3-2012

Peridynamic models for dynamic brittle fracture

Wenke Hu
University of Nebraska-Lincoln, huwenke_nbu@hotmail.com

Peridynamic Models for Dynamic Brittle Fracture

By

Wenke Hu

A DISSERTATION

Presented to the Faculty of

The Graduate College at the University of Nebraska

In Partial Fulfillment of Requirements

For the Degree of Doctor of Philosophy

Major: Engineering

Under the Supervision of Professor Florin Bobaru

Lincoln, Nebraska

March, 2012

Peridynamic Models for Dynamic Brittle Fracture

Wenke Hu, Ph.D.

University of Nebraska, 2012

Adviser: Florin Bobaru

Damage and failure in composite materials under dynamic loading has been extensively studied in experiments for several decades. Composite materials exhibit various damage and failure patterns under different loading rates, such as splitting and branching. Classical models cannot directly be applied to problems with discontinuous fields. A new nonlocal continuum model, peridynamics, has been proposed with the goal of solving dynamic fracture problems.

The *J*-integral has the physical significance of energy flow into the crack tip region. We present a rigorous derivation for the formulation of the *J*-integral in peridynamics using the crack infinitesimal virtual extension approach. We introduce an algorithm for computing this nonlocal version of the *J*-integral. Convergence studies are performed and the results converge to the FEM calculations when the nonlocal region goes to zero. We discuss how the boundary conditions and the peridynamic "skin effect" may influence the peridynamic *J*-integral value. We computationally show the path-independence of the peridynamic *J*-integral.

A new peridynamic model for unidirectional fiber-reinforced composite is proposed based on a homogenization process. We discretize this model and use it to simulate dynamic brittle fracture and damage in unidirectional fiber-reinforced composites. We

analyze dynamic effects induced by different types of dynamic loading on the fracture and damage behavior of such materials. The simulations show that dynamic conditions can lead to co-existence of and transitions between fracture modes, like matrix shattering and splitting cracks. We observe crack migration in the matrix, including crack branching in the matrix similar to what is observed in recent dynamic experiments.

Multilayer glass materials are being investigated for wider use in industry and military. Experimental results of high-velocity impact on multilayer glass show complex patterns of dynamic brittle fracture. We study the damage and fracture of multilayer glass material under impact by using a three-dimensional peridynamic model. Convergence studies are performed in terms of damage patterns and projectile speed profile. The results for the damage patterns at various impact speed, fracture energy, and thickness of glass pate, are compared with available experimental results.

Acknowledgements

I would like to thank many people for their support and guidance. First and foremost, I would like to thank my adviser Dr. Florin Bobaru for all his support, for his patience, for his numerous suggestions in research during the past four years. I learned a lot from him not only the way to conduct research and write papers but also the way to see life and science in their full depth.

I would also like to thank Dr. Yuris A. Dzenis, Dr. Ruqiang Feng, Dr. Stewart A. Silling, and Dr. John Reid for serving on my committee. Dr. Yuris A. Dzenis and Dr. Ruqiang Feng, I would like to thank you for being the readers for my dissertation. I express thanks Dr. Stewart A. Silling for providing such a great theory that turned out to be essential in my PhD thesis and for sparing a time to attend my thesis defense.

I also thank the people from Holland Computing Center, University of Nebraska-Lincoln, especially Tom Harvill, for helping me to run my simulations smoothly on the clusters and for their assistance with all types of technical problems - at all times.

I express thanks to Dr. Jian Yu (ARL) for providing experiment data.

I gratefully acknowledge the financial support offered through research contracts between UNL and the ARO (Dr. Larry Russell), and ARL (project coordinators Dr. C.F. Yen and Dr. C. Randow), ARO award number 58450EG, the Sandia National Laboratories (Dr. S.A. Silling), contract number 568428 and DE-AC04-94AL85000, Boeing Research &

Technology, the Applied Mathematics division (Dr. E. Askari). Those funding sources that made my Ph.D. work possible.

I would like to thank Tom and Ann Bussy and we have a great time together. Thanks to my friends, Monchai, Nan, Zhanping, Lili, and others that I cannot include all names here.

Last but not least, I wish to thank my parents, Guoliang Hu and Jianfen Shen for their love and encouragement. A big thank to my loving wife, Jinying Shan, for supporting me and for taking care of my baby during these months so that I can focus on my research and finish my thesis. I dedicate this thesis to my wife, Jinying Shan, and my baby, William Hu.

Contents

List of TABLES

LIST OF FIGURES

Chapter 1
Introduction

In this chapter, we start by discussing the experimentally observed fracture modes and damage pattern in dynamic brittle fracture. Then, the merits and difficulties or limitations of several major approaches aimed at computationally modeling brittle dynamic fracture, are discussed.

1.1 Literature review

Dynamic fracture is the most fundamental in the science of fracture [1]. Dynamic brittle fracture is characterized by rapid crack propagation with low energy release and with very little plastic and/or visco-elastic deformation before failure occurs. Dynamic brittle fracture is extremely important in various fields of engineering applications, such as

aerospace structure design, fielded armor vehicle used in military operation, and mining industry. Damage and failure in solids under dynamic loading has been extensively studied in experiments for several decades. Material exhibits various damage modes and failure patterns under different loading rates, such as crack curving, crack branching, fragmentation, spallation, and delamination. The fragmentation phenomenon in brittle materials, such as glass, is a succession of multiple branching of what was initially a single crack [2]. The simple fragmentation and multiple fragmentation of a single-layer glass plate have been characterized by the amplitude of contact between the projectile and the target by [3]. The spall fracture, which is a common failure mode under high velocity impact, was firstly discovered by [4]. After that, many experiments have been conducted to investigate the spall fracture under high velocity impact. It is interesting to observe single and double spall fracture in propellant SRI-A under different impact velocities by [5]. The studies of dynamic fracture have been extended to composite material due to the extensive use of the composite material in aerospace structure, such as Boeing 787 commercial airplane. Dynamic experiments are conducted in [6] with different strain rates from low (10^{-4} s^{-1}) to high (10^{2} s^{-1}) for glass/vinylester composites. The experiment results show that the dynamic damage behavior and failure patterns are highly sensitive to strain rates. Extensive fracture and damage produced by interconnected splitting, matrix cracking, delamination, and fiber breakage, are observed under higher strain rates. Damage and failure in S2-glass/vinylester UD composites is induced using the Split-Hopkinson-Pressure-Bar technique in [7], where the authors investigate cracking behavior under different strain rates. They observe matrix cracking

and debonding for loading unidirectional fiber-reinforced composites (UD FRCs) in the transverse direction. Remark: Crack means a line along which something has split without breaking into separate parts; Fracture (or damage) is the local separation of an object or material into two or more pieces[8].

Wave propagation and interaction with cracks are essential factors in dynamic brittle fracture as they determine the evolution of damage and fracture modes in brittle solids. A series of dynamic experiments are performed by [9] to investigate the effect of stress wave on crack initiation and arrest, crack branching and curving. In [10] it is shown that reflection of stress waves from distal surface (parallel to, and farthest away from the strike face) and interaction the reflected wave with cracks result in further spalling and fragmentation in brittle material under impact.

Significant efforts have been made to model damage and failure based on classical elasticity. However, the equations of motion in classical continuum mechanics cannot be directly applied to the discontinuous field because the spatial derivatives in differential equations fail to exist when a discontinuity exist, such as a crack. Thus, external criteria or special treatments are needed in order to introduce damage or cracks in such problems. Significant efforts have been made to develop crack propagation and damage models by employing ad-hoc modifications of the classical models and modifications of the FEM in order to overcome those issues

- The cohesive finite element method uses the cohesive zone model (cohesive law) implemented in finite elements. The fundamental framework for cohesive zone

model was introduced by [11] and [12]. The cohesive zone elements were developed by [13] and [14] in order to corporate cohesive zone model in computational fracture mechanics, especially in FEM. Cohesive zone elements are usually placed between continuum elements. These cohesive zone elements can open when damage growth occurs in order to simulate crack initiation or crack propagation. However, the cracks can only follow the path where the cohesive zone elements are placed, which leads to the need of prior knowledge of actual crack path. In dynamic fracture, crack paths and damage modes are hard to know in advance due to the waves propagation and interaction with the crack. For instance, cascading branching or arresting the propagation of secondary branches can be observed in different material under same loading condition [15]. Thus, it is difficult to place the cohesive zone elements in advance. Mesh dependency is an additional problem in cohesive zone FEM based methods [16].

- The extended finite element method (XFEM) was introduced in [17] by adding enrichment functions (additional degrees of freedom) to the approximation which contains a discontinuous displacement field. Hence, a crack can be allowed to pass through the elements rather than along the element boundaries, which resolves the mesh dependency. XFEM is employed to analyze and simulate the dynamic crack propagation ([18]; [19]). However, subdivision of the cut elements for numerical integration purpose increases the complexity and the cost of the method [20]. Furthermore, this method still requires phenomenological damage models and branching criteria. For instance, an interface damage model was

introduced in order to model the failure in matrix/fiber interfaces [21]. The crack need to be tracked by using, for example, level set (see [17]). When more than a couple of cracks start developing in the material like in fragmentation, XFEM approach might not be an option.

Atomistic studies (molecular dynamics simulations) of dynamic fracture are another approach besides the classical continuum mechanics. Some important features of dynamic fracture were described by using atomistic simulations in [22]. The molecular-dynamics simulations are shown to have the capability to reproduce some of the phenomena that are discovered in experiments ([23]; [24]). In last decades, the large-scale atomistic modeling of dynamic fracture is widely employed with the number of atoms exceeding one billion ([25]; [26]). Nowadays, molecular-dynamics simulation can be performed with 320 billion atoms, which corresponds to a cubic piece with an edge length of 1.56μm [27]. However, two issues are still remaining: 1). The length scale spanned by MD simulation is too small for real problem so it is difficult to model the original geometry; 2) The time scales spanned are too short. In order to accelerate the simulation, the computations are done by using very high loading rate, which is much higher than those seen in practical. Thus, the atomistic studies can provide some fundamental understanding of the underlying basic physical processes of dynamic fracture, but they cannot achieve predictive capabilities for dynamic fracture, at lease for no foreseeable future [1].

Most recently, a new nonlocal continuum model, peridynamics [28], has been proposed with the goal of solving dynamic fracture problems, which does not need ad-hoc criteria to guide the dynamic crack propagation. In order to overcome mathematical inconsistencies when cracks form in the classical continuum mechanics models, peridynamics [28] uses an integral of forces over a nonlocal region around a point to replace the divergence of the stress tensor in the equations of motion. Thus, the peridynamic equations of motion can directly apply to discontinuous fields, such as crack. In peridynamics, internal forces within a continuous body are expressed through interactions between pairs of material points, called peridynamic bonds, and damage is part of the constitutive model.

The peridynamic theory has been successfully applied to damage analysis of viscoplastic materials ([29]; [30]), dynamic fracture and crack branching in glass ([15]; [31]), damage in composite materials under quasi-static loading, and impact or shock loading ([32]; [33]) and nano-scale structures ([34]; [35]).

1.2 Motivation and objective

Fracture toughness is a material property which describes the ability of a material containing a crack to resist fracture. Fracture toughness can be used for material characterization and performance evaluation. Fracture toughness can be measured and characterized by the *J*-integral. The classical local theoretical *J*-integral was introduced by [36] and was used originally as a measure of the intensity of elastic-plastic crack-tip

fields. The nonlocal version of state-based peridynamic *J*-integral is presented based on energy balance approach [37].

The work here mainly validates the peridynamics by theoretically and numerically studying the *J*-integral. In following chapter, we present bond-based peridynamic *J*-integral based on the crack infinitesimal virtual extension approach. We will show that the nonlocal *J*-integral has the same format as classical *J*-integral as horizon goes to zero. Moreover, the path independent of peridynamic *J*-integral is also studied.

The composite materials and multilayer glass materials are widely used in various engineering fields, such as automobile industry, sports, aerospace industry, and military applications. However, the spontaneous formation and propagation of brittle cracks is an open problem. Most recent attempts have addressed quasi-static loading conditions ([38]; [39]; [40]). The existing modeling methods are not able to capture essential features of failure in composite and multilayer materials from dynamic loading. The response of composite and multilayer materials in terms of damage and fracture to the dynamic loading includes matrix cracking, splitting, delamination, fiber breakage, fragmentation, and spallation. Moreover, Gilat et al. [41] studied the strain rate sensitivity of IM7/977-2 carbon/epoxy composite under dynamic tensile loading and found the material to be highly strain rate sensitive. In particular, they found that the composite is more strain rate sensitive at shallower angles. Moreover, Rio et al. [42] performed dynamic tensile tests on the different carbon/epoxy composite of unidirectional (0° and 90°) and quasi-isotropic configurations. The results of the dynamic tests showed little effect of strain rate

on tensile strength of a unidirectional composite loaded in the fiber direction but in the other cases strength are sensitive to the strain rate. However, the composite breaks quasi-brittle under high-strain rate. All the observed strain-rate dependence may come only from the dynamic loading, such as the effects of inertia and stress wave propagation. This is one question that our model is trying to answer.

Recently, the peridynamics offer the great potential for predicting the complex fracture modes and damage pattern in dynamic fracture. Two peridynamic models were proposed for modeling composites by [43], [32], and [33]. In Xu et al [32] develop peridynamic model for predicting damage patterns in laminated composites subjected to low-velocity impact. However, the evaluation of the bond stiffness is done via a computational procedure for a specific horizon and a specific discretization size, and analytical formulas for the parameters used in the model are not given in [32]. In [33] individual fibers are explicitly modeled. Bond stiffness for bonds inside the fibers is fitted to fiber properties, while bond stiffness for bonds inside the matrix material is fitted to matrix properties. However, this model has significant limitations since it is not practical for solving realistic problems in fiber-reinforced laminated composites because of the huge number of fibers contain in such materials.

In this thesis, a new homogenization-based peridynamic model for unidirectional fiber-reinforce composite is proposed for simulating dynamic fracture and damage. Analytic formulas to obtain the bond stiffness for bonds aligned with the fiber direction and all other bonds are provided by matching the peridynamic strain energy density in a

composite lamina under a homogeneous deformation with the classical linear elastic strain energy density, under the same deformation. We will use this model to study the interaction between the stress waves and the crack propagation behavior in unidirectional fiber-reinforced composites (UD FRC) under dynamic loading.

We then study the response of multilayered systems like glass laminate under high impact velocity by using peridynamics. Parametric studies are performed, such as various impact speeds and various thicknesses, in order to identify those factors that influence the damage patterns and ballistic performance. We compare with experimental results taken tests recently performed at the ARL (Aberdeen) by Dr. Yu.

1.3 Thesis outline

The outline of this thesis is as follows:

- Chapter 2 – We review the basic formulation for bond-based peridynamics. We discuss about the discretization scheme for the peridynamic equations of motion. Finally, the three different types of convergence studies are introduced and discussed in detail.

- Chapter 3 – We give the derivation for the peridynamic *J*-integral based on the infinitesimal virtual crack extension. The algorithm used for computing the peridynamic *J*-integral is presented. Validation of the peridynamic *J*-integral algorithm is demonstrated by considering a plate without crack for which the *J*-

integral should be zero on a closed contour. Then, we perform two types of convergence (m-convergence and δ-convergence) studies for a 2D plate in plate stress condition with single-edge notch and double edge-notch and we compare the peridynamic results with those obtained from finite element calculations for the classical *J*-integral using in Abaqus 6.10. Calculations related to the path-independence of the nonlocal *J*-integral are also shown. This chapter have been submitted for publish [44].

- Chapter 4 – We briefly review the classical equations for a unidirectional fiber-reinforced composite lamina. We present the new model with the analytical connections between the microscopic parameters in the peridynamic formulation and the macroscopic material properties, as well as obtain the scaling factors required for maintaining the same elastic strain energy density with a classical material. We treat a number of examples of dynamic fracture in UD FRCs and analyze, in particular, the influence of the stress waves (generated by the suddenly applied loads or reflected from the boundaries) on the crack propagation and damage patterns. We use two different loading cases, vary the loading amplitude, and compare the peridynamic results with experiments. We perform convergence studies in terms of the crack path and crack propagation velocity. This chapter have been appeared or to be appeared ([45]; [46]).

- Chapter 5 – We study the three-dimensional glass laminate (first layer is glass plate and the second layer is a polycarbonate layer) impact problem based on

peridynamics for the first time. The damage patterns of the glass layer with various conditions, such as different impact speeds and different plate thickness, are compared with some experiment results. The convergence studies in terms of damage pattern and perforation speed are shown.

- Chapter 6 – We present the conclusions and future work.

Chapter 2
The Peridynamic theory

In this chapter, we briefly review the formulation of the peridynamic theory and the damage model in peridynamics. We also introduce the discretization scheme in order to discretize the peridynamic formulation, which is relative easy to implement. Finally, we present the three types of numerical convergence in peridynamics.

2.1 Peridynamic formulation

The peridynamic theory [28] is a non-local formulation that extends the classical continuum mechanics formulation. The term “peridynamic” comes from the Greek roots for near and force. In peridynamics, every material point is connected to the other points inside a certain “horizon” region through peridynamic bonds. In this way, instead of the

divergence of stresses term in the classical equations, one uses an integral over the horizon of the current point of forces, per unit volume squared, acting in the peridynamic bonds. Since the spatial differentiation is eliminated from the mathematical framework of peridynamics, this formulation is well suited to modeling problems in which discontinuities emerge, interact, and evolve in time. Indeed, the integration of forces can be directly applied over discontinuous displacement fields, which appear in the case of crack propagation.

The peridynamic model is a framework for continuum mechanics based on the idea that pairs of particles exert forces on each other across a finite distance. The peridynamic equations of motion are given as

$$\rho\ddot{\mathbf{u}}(\mathbf{x},\mathrm{t}) = \int_H \mathbf{f}(\mathbf{u}(\mathbf{x},\mathrm{t}) - \mathbf{u}(\mathbf{x},\mathrm{t}), \hat{\mathbf{x}} - \mathbf{x})\mathrm{dV}_{\hat{\mathbf{x}}} + \mathbf{b}(\mathbf{x},t) \tag{2.1}$$

where **f** is the pairwise force function in the peridynamic bond that connects point $\hat{\mathbf{x}}$ to **x,** and **u** is the displacement vector field. ρ is the density and **b**(**x**, *t*) is the body force. The integral is defined over a region *H* called the "horizon". The region is taken here to be a circle/sphere of radius δ, but its shape is arbitrary as long as the micromodulus function exists so that linear momentum and angular momentum are satisfied. The horizon is the compact supported domain of the pairwise force function around a point **x**. We will abuse the terminology and also call the "horizon", the radius of the horizon, δ.

The peridynamic horizon may be viewed as an "effective" interaction distance or an "effective length-scale" of a continuum model in a dynamic problem [47]. In principle, the exact size and shape of the horizon could be found from wave dispersion curves for a

specific material under specific dynamic conditions (see [28]). In practice, for problems where a material length-scale does not readily manifests itself, we take the horizon to smaller and smaller values and monitor the convergence of the results (see [48] and [15]). A convenient horizon size is one which is sufficiently large that the computations are efficient (we can use coarser grids with a larger horizon), but sufficiently small that the results do not change much if one chooses to use a smaller horizon. Please note that in dynamic fracture problems, while one cannot guarantee convergence of results in the limit of the horizon going to zero, recent simulations show, for crack branching problems, that convergence in terms of the crack path and crack propagation speed happens as the horizon goes to zero (see, e.g. [15] and [31]).

Let $\boldsymbol{\xi} = \hat{\mathbf{x}} - \mathbf{x}$ be the relative position in the reference configuration and $\boldsymbol{\eta} = \hat{\mathbf{u}} - \mathbf{u}$ is the relative displacement. From the definition of the horizon, we have

$$\|\boldsymbol{\xi}\| > \delta \Rightarrow \mathbf{f}(\boldsymbol{\eta}, \boldsymbol{\xi}) = 0 \tag{2.2}$$

so there is no force acts between two material points if the relative position (in the reference configuration) is larger than the given horizon size (see Figure 2.1).

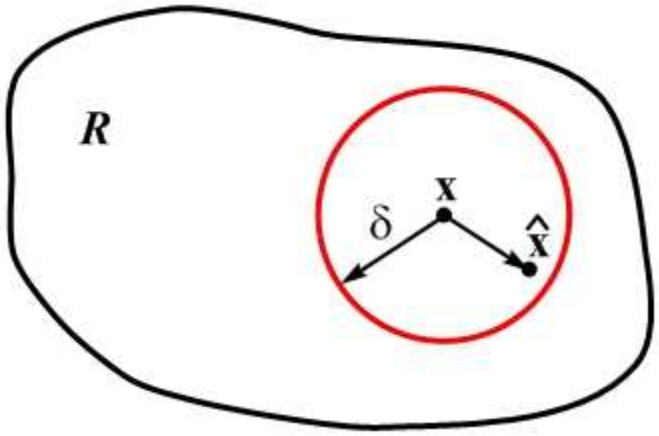

Figure 2.1. Each point x interacts directly with the points $\hat{\mathbf{x}}$ in the horizon (red circle).

The pairwise force function **f** is required to satisfy two conservation laws as follows:

$$\mathbf{f}(\boldsymbol{\eta},\boldsymbol{\xi}) = -\mathbf{f}(-\boldsymbol{\eta},-\boldsymbol{\xi}) \quad \forall \boldsymbol{\eta},\boldsymbol{\xi} \tag{2.3}$$

which assures the conversation of linear momentum (*linear admissibility condition* in peridynamics).

$$(\boldsymbol{\xi}+\boldsymbol{\eta})\times\mathbf{f}(\boldsymbol{\eta},\boldsymbol{\xi}) = \mathbf{0} \quad \forall \boldsymbol{\eta},\boldsymbol{\xi} \tag{2.4}$$

which assures the conversation of angular momentum (*angular admissibility condition* in peridynamics).

A micro-elastic material [28] is defined as one for which the pairwise force derives from a scalar micro-potential ω:

$$\mathbf{f}(\boldsymbol{\eta},\boldsymbol{\xi}) = \frac{\partial \omega(\boldsymbol{\eta},\boldsymbol{\xi})}{\partial \boldsymbol{\eta}} \tag{2.5}$$

The strain energy density at a given point is

$$W = \frac{1}{2}\int_H \omega(\boldsymbol{\eta}, \boldsymbol{\xi}) dV_{\xi} \tag{2.6}$$

The factor of 1/2 appears because each points of a peridynamic bond "owns" only half the energy in the bond.

A *linear* micro-elastic potential, which leads to a linear relationship between the bond force and the relative elongation of the bond, is obtained if we take

$$\omega(\boldsymbol{\eta}, \boldsymbol{\xi}) = \frac{c(\|\boldsymbol{\xi}\|)s^2 \|\boldsymbol{\xi}\|}{2} \tag{2.7}$$

where s the bond relative elongation

$$s = \frac{\|\boldsymbol{\xi} + \boldsymbol{\eta}\| - \|\boldsymbol{\xi}\|}{\|\boldsymbol{\xi}\|} \tag{2.8}$$

The corresponding pairwise force becomes

$$\mathbf{f}(\boldsymbol{\eta}, \boldsymbol{\xi}) = \frac{\partial \omega(\boldsymbol{\eta}, \boldsymbol{\xi})}{\partial \boldsymbol{\eta}} = c(\|\boldsymbol{\xi}\|)s \frac{\partial \|\boldsymbol{\xi} + \boldsymbol{\eta}\|}{\partial \boldsymbol{\eta}} \tag{2.9}$$

with

$$\frac{\partial \|\boldsymbol{\xi} + \boldsymbol{\eta}\|}{\partial \boldsymbol{\eta}} = \mathbf{e}$$

where $\mathbf{e}$ is the unit vector along the direction of the bond between $\hat{\mathbf{x}}$ and $\mathbf{x}$ in the deformed configuration ($\boldsymbol{\xi} + \boldsymbol{\eta}$).

The function $c(\|\boldsymbol{\xi}\|)$ is called micromodulus function and it represents the bond elastic stiffness. Some possible choices for the micromodulus function are given in 1D ([48]), 2D ([15]) and 3D ([49]). These are obtained by matching the elastic strain energy density at a material point in the bulk (see point A in Figure 2.2) of a microelastic peridynamic material to the elastic strain energy density from the classical theory, when both materials are under the same homogeneous deformation (see Eq.(2.10)).

$$W_{\text{classical}} = \frac{1}{2}\int_H \frac{c(\|\boldsymbol{\xi}\|)s^2\|\boldsymbol{\xi}\|}{2} dV_{\hat{\mathbf{x}}} \tag{2.10}$$

Hence, the micromodulus c, can match to the measured material parameters, such as the Young's modulus. For simplicity, we use the form of the micromodulus function obtained for a point in the bulk for all points, including those that are within δ from the surface (like point B in Figure 2.2). This leads to an effectively softer material close to the boundary, since now the integral in Eq. (2.10) is over a smaller region and for the match to hold one would have to increase the micromodulus value. Therefore, the strains will be larger for the “skin” of the domain than in the bulk of the material, for a deformation that classically would be homogeneous (see [50]). We call this behavior in peridynamics the “skin effect”.

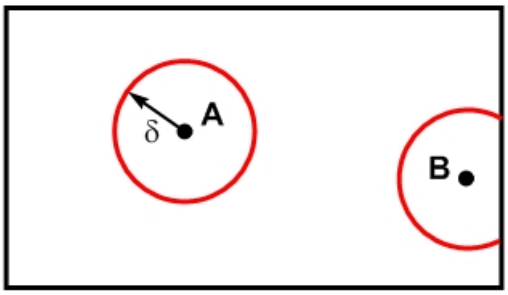

Figure 2.2. The skin effect in peridynamics for points close to the boundary.

2.2 Damage model in peridynamics

The damage model in peridynamics [28] consists in breaking the peridynamic bonds connecting any two nodes when the relative change in distance between the nodes exceeds a certain prescribed value.

As mentioned in [49], the pairwise force for a micro-elastic material with damage is

$$\mathbf{f}(\boldsymbol{\eta},\boldsymbol{\xi}) = \frac{\boldsymbol{\xi}+\boldsymbol{\eta}}{\|\boldsymbol{\xi}+\boldsymbol{\eta}\|} c(\|\boldsymbol{\xi}\|) s \mu(t,\|\boldsymbol{\xi}\|) \tag{2.11}$$

where $\mu(t,\xi)$ is a history-dependent scalar-value function which has the value of either 0 or 1.

$$\mu(t,\|\boldsymbol{\xi}\|) = \begin{cases} 1 & \text{if } s(t,\|\boldsymbol{\xi}\|) < s_0 \\ 0 & \text{if } s(t,\|\boldsymbol{\xi}\|) > s_0 \end{cases} \tag{2.12}$$

Here, the s_0 is the critical relative elongation. The damage model is now history-dependent. If the relative elongation s between two points over the critical value s_0, the

bonds cannot sustain any force after breaking and this procedure is irreversible (see Figure 2.3). Reversible-type damage can also be introduced (see[34], [35]) and allow bonds to re-form.

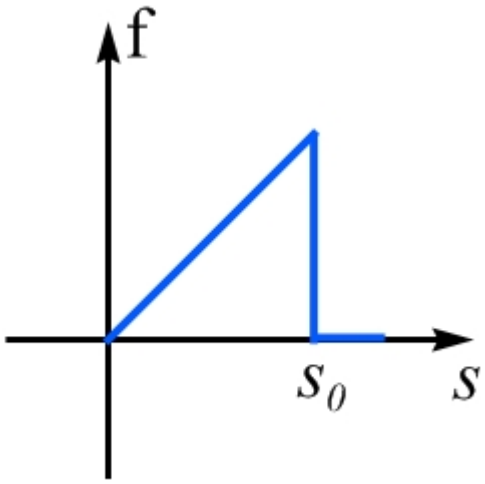

Figure 2.3. Bond force as a function of bond stretch.

Some possible choices for the critical relative elongation are given in 2D ([15]) and 3D ([49]). This critical relative elongation parameter $s_0 s_0$ is obtained by equating the work, per unit fracture area, required to break all the bonds across the fracture surface to the fracture energy required for complete separation of the two halves of the body. For the 2D case, we have

$$G_0 = 2\int_0^{\delta}\int_z^{\delta}\int_0^{\cos^{-1}(z/\|\xi\|)} [c(\|\xi\|)s_0^2 \|\xi\|/2]\|\xi\| \, d\theta d\xi dz \tag{2.13}$$

where G_0 is fracture energy, which is a measureable quantity in experiments. For each point A along the dashed line, $0 \le z \le \delta$, the work required to break the bonds connecting

A to each point B in the circular cap is summed by the integrals in Eq. (2.13) (see Figure 2.4).

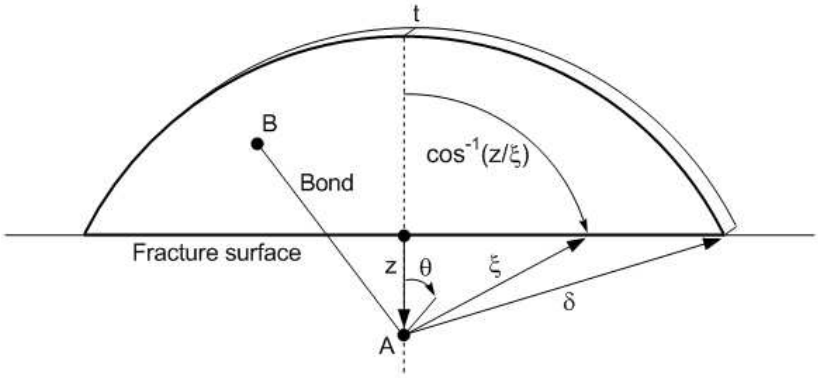

Figure 2.4. Evaluation of fracture energy. For each point A along the dashed line, $0 \le z \le \delta$, the work required to break the bonds connecting A to each point B in the circular cap ([15]).

We impose the same s_0 over the entire region, which results in an "effectively" weaker material in the regions near the boundary or damage already happened. This is similar to the skin effect discussed in previous section. Recently, the damage dependent s_0 is introduced in order to reduce the effectively weaker bond strength near the boundary or in damaged regions ([49], [31]).

2.3 Discretization for peridynamics

In this section, we briefly review discretization approach for peridynamics, which is introduced by [49]. The entire body is discretized into nodes, each with a known volume in the reference configuration. The nodes are not necessary regularly spaced and its volume can be non-uniform. However, for simplicity, we can use the uniform

discretization with certain grid spacing (see Figure 2.5). This method is meshfree in the sense that there are no elements or other connectivity between the nodes.

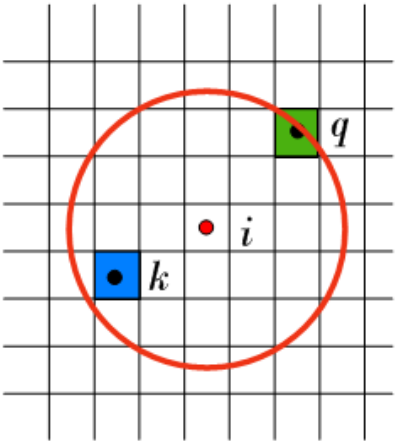

Figure 2.5. Discretized grid and nodes inside of horizon of node *i*.

The discretized form of peridynamic equation of motion by using the mid-point integration scheme for the domain integral:

$$\rho \ddot{\mathbf{u}}_i^n = \sum_j \mathbf{f}(\mathbf{u}_j^n - \mathbf{u}_i^n, \mathbf{x}_i - \mathbf{x}_i) V_j + \mathbf{b}_i^n \tag{2.14}$$

where V_j is the volume of the node j. $\mathbf{u}_i^n = \mathbf{u}(\mathbf{x}_i, t^n)$, and n is the time step number.

Remark: In 1D and 2D, the volume of a node is a length and area, respectively, that represents a portion of the body assigned to a node. Furthermore, the volume of a node does not have restrictions in terms of geometric shape, but it is desirable that the node has a central location in the volume represented by the area (see Figure 2.5). This is

necessary to obtain a better representation of the body by the meshless grid and, therefore, to gain more accuracy in the numerical solution.

In the calculation of the peridynamic bond-force between node *i* and *q*, for instance, it is necessary to calculate the portion of the volume of node *q* inserted in the horizon of the source node *i*. For example, in Figure 2.5, the volume of node *k* is completely covered by the horizon of source node, *i*. However, the volume of node *q* is only partially covered by the horizon. We can either use the entire volume of the node *q* or complete it from the computation. This is simple, but it introduces numerical error. In here, we use a simple, efficient, and robust algorithm that approximates the area for the nodes area partially covered by horizon. This algorithm is for two dimension grid but can be easily extended to three dimensions. It defines the fraction of the volume, *frac*, covered by the source node by the following algorithm (where Δx, Δy are the grid spacings in the x, y directions, respectively):

Table 2.1. Volume calculation.

1:	**if** $\|\|\xi\|\| < \delta$ - max(Δx, Δy) / 2 **then**
2:	*frac* = 1.0
3:	**else if** $\|\|\xi\|\| < \delta$ **then**
4:	*frac* = (δ + max(Δx, Δy) / 2 - $\|\|\xi\|\|$) / (2 max(Δx, Δy))
5:	**else if** $\|\|\xi\|\| < \delta$ + max(Δx, Δy) **then**
6:	*frac* = (δ + max(Δx, Δy) / 2 - $\|\|\xi\|\|$) / (2 max(Δx, Δy))
7:	**else**
8:	*frac* = 0.0
9:	**end if**

To solve the ordinary differential equation defined by the equation of motion of the peridynamic model, we introduce and implement an explicit time integration Velocity-

Verlet algorithm [51], which is a more numerically stable version of central-differences, is used for the peridynamic analysis.

$$\begin{aligned}\dot{\mathbf{u}}_{n+1/2} &= \dot{\mathbf{u}}_n + \frac{\Delta t}{2}\ddot{\mathbf{u}}_n \\ \mathbf{u}_{n+1} &= \mathbf{u}_n + \dot{\mathbf{u}}_{n+1/2}\Delta t \\ \dot{\mathbf{u}}_{n+1} &= \dot{\mathbf{u}}_{n+1/2} + \frac{\Delta t}{2}\ddot{\mathbf{u}}_{n+1}\end{aligned} \tag{2.15}$$

where $\mathbf{u}$, $\dot{\mathbf{u}}$, and $\ddot{\mathbf{u}}$ are displacement, velocity, and acceleration vectors, respectively. Δt is the time step size. Moreover, the stable time step size Δt is given by[49] as follows

$$\Delta t < \sqrt{\frac{2\rho}{\sum_j V_j \mathrm{c}}} \tag{2.16}$$

where c is the micromodulus function. The maximum stable time step tends to be limited by the horizon size, which implies Δt reduces as the horizon size δ decrease.

2.4 Types of convergence scheme in peridynamics

The peridynamic model is nonlocal and contains a length-scale determined by the horizon δ while the classical elasticity has no intrinsic length-scale. Thus, numerical convergence of the solutions in the peridynamic model differs from traditional convergence in the FEM (like p-type, h-type, and hp-type).

Three types of convergence scheme in peridynamics are defined and discussed for the numerical integration for the spatial variable [48]:

a. The δ-convergence: $\delta \to 0$ and m (the ratio between the horizon size and grid spacing) is fixed or increases with decreasing δ but at a slower rate, such that the ratio m/δ increases. In this case the numerical peridynamic approximation converges to an approximation of the classical solution, almost everywhere. The larger m is, the closer this approximation becomes. This type of convergence does not guarantee uniform convergence to the classical solution.
b. The m-convergence: δ is fixed and $m \to \infty$. The numerical peridynamic approximation converges to the exact non-local peridynamic solution for the given δ.
c. The (δm)-convergence: $\delta \to 0$ and m increases while decreasing δ. In this case, the numerical peridynamic approximation converges to the analytical peridynamic solution and converges uniformly to the local classical solution, almost everywhere.

In Figure 2.6, there is an illustration of the three types of convergence in the peridynamic model. In the original grid, the horizon size δ is equal to $3\Delta x$, where $m = 3$. In Figure 2.6(a), the first type of convergence, the δ-convergence, where the horizon size becomes smaller, while m has the same value as 3. In Figure 2.6(b), the horizon size keeps the same value, but m increases to 6, therefore, the requirements for the m-

convergence is achieved. In Figure 2.6(c), the horizon size decrease while *m* increases to 4, and with this configuration, it respects the requirements for the (δ*m*)-convergence.

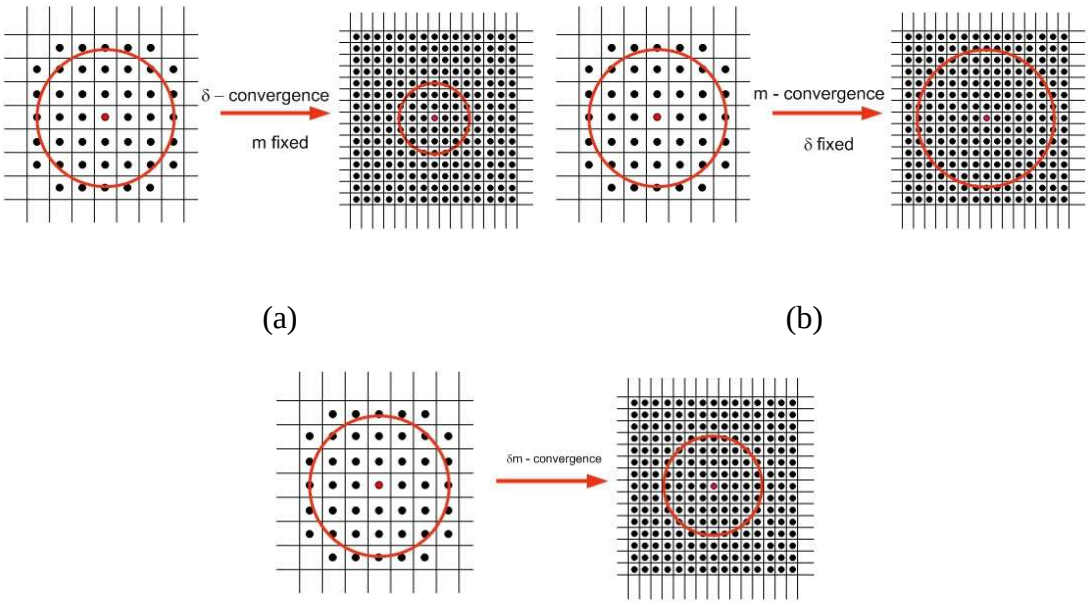

Figure 2.6. Three cases of convergence in peridynamics: (a). δ –convergence; (b). *m*-convergence; (c). (δ *m*)-convergence.

Remark: In peridynamic, the horizon δ is required to cover more than source node, which *m* should equal or larger than one. Thus, for the δ-convergence, the grid refinement is required when the horizon size decrease in order to satisfy above condition.

2.5 Summary

In this chapter, we briefly reviewed the characteristics of the peridynamic formulation and introduced the damage model in peridynamics. Compared with classical continuum mechanics, the peridynamic equations of motion apply to discontinuous fields without any special treatment. The parameters of the peridynamic model, such as the micromodulus function and the critical relative elongation, can be obtained by matching the corresponding parameters in the classical theory. In order to solve the peridynamic equation of motion, mid-point integration scheme and Velocity-Verlet algorithm were introduced for the spatial and temporal discretization. Three different types of convergence were also presented and discussed in detail.

Chapter 3
The Peridynamic *J*-integral

In this chapter, we first introduce the classical *J*-integral formulation in fracture mechanics. Then, we present a rigorous derivation for the formulation of the *J*-integral in bond-based peridynamics using the crack infinitesimal virtual extension approach. We give a detailed description of an algorithm for computing this nonlocal version of the *J*-integral. We present two types of convergence studies for two different geometries: a single edge-notch configuration and a double edge-notch sample. We compare the results with results based on the classical *J*-integral and obtained from FEM calculations that employ special elements near the crack tip. We also observe, computationally, the path-independence of the peridynamic *J*-integral.

3.1 The classical J-integral

The *J*-integral formulation for a linear elastic body in 2D was introduced in [36] the quantity was shown to be path independent and an equivalent value with the energy release rate. The *J*-integral can be understood both as a fracture energy parameter and as a stress intensity parameter because the *J*-integral uniquely characterizes crack–tip stresses and strains ([52]; [53]). The *J*-integral is extensively used to compute energy flow to the crack tip, to estimate crack opening and is used as part of failure criteria for ductile materials.

Consider an arbitrary integral path around the tip of a crack. The *J*-integral in 2D domain is given by

$$J = \oint_{\Gamma} \left(w\mathbf{n}_1 - \mathbf{T} \bullet \frac{\partial \mathbf{u}}{\partial x} \right) dS \tag{3.1}$$

where dS is the length increment along the contour Γ. w, $\mathbf{u}$ and $\mathbf{T}$ are the strain energy density, displacement vector and the traction vector, respectively. $\mathbf{n}_1$ is the outward unit vector normal to the contour Γ. As mentioned previously, *J*-integral equals to the strain energy release rate G in linear elastic body, whereas the stress intensity factor K_I can be computed as follow

$$J = G = \frac{K_I^2}{\hat{E}} \tag{3.2}$$

$$\hat{E} = \begin{cases} E & \text{for plane stress} \\ \dfrac{E}{1-\nu^2} & \text{for plane strain} \end{cases} \tag{3.3}$$

where E and ν are young's modulus and Poisson's ratio, respectively

3.2 Derivation of the peridynamic *J*-integral

The physical interpretation of the classical *J*-integral is the rate of change of potential energy with respect to the incremental change of crack length along the crack line. Thus, we use the same concept in order to derive the peridynamic *J*-integral for a mode I crack that grows in a self similar manner in a 2D microelastic peridynamic body. We consider a certain domain Ω, which contains a straight crack of length a, in equilibrium and zero body force density. The peridynamic equations of motion become:

$$\int_{\Omega} \mathbf{f}(\mathbf{u}(\hat{\mathbf{x}}, t) - \mathbf{u}(\mathbf{x}, t), \hat{\mathbf{x}} - \mathbf{x}) dA_{\hat{\mathbf{x}}} = 0 \tag{3.4}$$

where $A_{\hat{\mathbf{x}}}$ represents the nodal area in 2D instead nodal volume $V_{\hat{\mathbf{x}}}$ in 3D.

The elastic energy density at any x in Ω for the microelastic material is

$$W(\mathbf{x};\mathrm{a}) = \frac{1}{2}\int_{\Omega(\mathrm{a})} \omega(\boldsymbol{\eta},\boldsymbol{\xi})\, dA_{\boldsymbol{\xi}} \tag{3.5}$$

where a is crack length (see Figure 3.1).

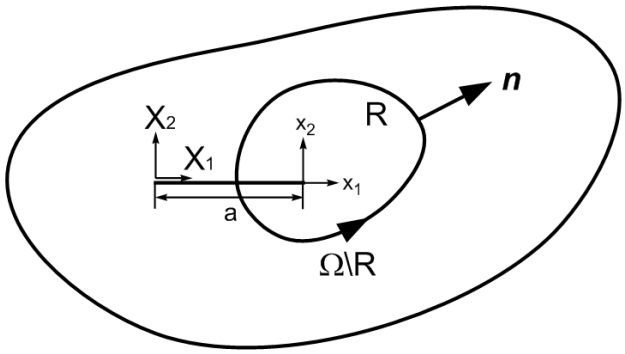

Figure 3.1. Two-dimensional body containing a straight crack.

Consider a fixed coordinate system (X_1, X_2) as in Figure 3.1. The local coordinate system (x_1, x_2) is attached to the crack tip and moves as the crack grows. Assume crack grows by an infinitesimal amount in the x_1 direction. Considering the change in total elastic strain energy resulting from an infinitesimal virtual extension of the crack we get:

$$\frac{dU}{d\mathrm{a}} = -\frac{d}{d\mathrm{a}} \oint_{R(\mathrm{a})} W(\mathbf{x};\mathrm{a})\, dA_{\mathbf{x}} \tag{3.6}$$

The right hand side of Eq. (3.6), by adding and subtracting $\oint_{R(\mathrm{a})} W(\mathbf{x};\mathrm{a}+\Delta\mathrm{a})\, dA_{\mathbf{x}}$, can be written as:

$$\frac{d}{d\mathrm{a}}\oint_{R(\mathrm{a})} W(\mathbf{x};\mathrm{a})dA_{\mathbf{x}} = \lim_{\Delta\mathrm{a}\to 0}\frac{1}{\Delta\mathrm{a}}\left[\oint_{R(\mathrm{a}+\Delta\mathrm{a})-R(\mathrm{a})} W(\mathbf{x};\mathrm{a}+\Delta\mathrm{a})dA_{\mathbf{x}} + \oint_{R(\mathrm{a})} W(\mathbf{x};\mathrm{a}+\Delta\mathrm{a}) - W(\mathbf{x};\mathrm{a})dA_{\mathbf{x}}\right]$$

$$= \oint_{\partial R} W(\mathbf{x};\mathrm{a})\mathbf{n}_1 dS + \oint_{R(\mathrm{a})}\frac{\partial W(\mathbf{x};\mathrm{a})}{\partial \mathrm{a}}dA_{\mathbf{x}} \tag{3.7}$$

Consider now the second term on the right hand side of Eq. (3.7) and by using Eq. (3.5) and Eq. (2.5), we have

$$\oint_{R(\mathrm{a})}\frac{\partial W(\mathbf{x};\mathrm{a})}{\partial \mathrm{a}}dA_{\mathbf{x}} = \frac{1}{2}\oint_{R(\mathrm{a})}\oint_{\Omega(\mathrm{a})}\mathbf{f}(\boldsymbol{\eta},\boldsymbol{\xi})\cdot\left(\frac{\partial \hat{\mathbf{u}}}{\partial \mathrm{a}} - \frac{\partial \mathbf{u}}{\partial \mathrm{a}}\right)dA_{\hat{\mathbf{x}}}dA_{\mathbf{x}}$$

$$= \frac{1}{2}\oint_{R(\mathrm{a})}\oint_{\Omega(\mathrm{a})}\mathbf{f}(\boldsymbol{\eta},\boldsymbol{\xi})\cdot\frac{\partial \hat{\mathbf{u}}}{\partial \mathrm{a}}dA_{\hat{\mathbf{x}}}dA_{\mathbf{x}} - \frac{1}{2}\oint_{R(\mathrm{a})}\oint_{\Omega(\mathrm{a})}\mathbf{f}(\boldsymbol{\eta},\boldsymbol{\xi})dA_{\hat{\mathbf{x}}}\frac{\partial \mathbf{u}}{\partial \mathrm{a}}dA_{\mathbf{x}} \tag{3.8}$$

The second term on the right hand side of Eq. (3.8) is equal to zero because of Eq. (3.4). Thus, Eq. (3.8) reduces to

$$\oint_{R(\mathrm{a})}\frac{\partial W(\mathbf{x};\mathrm{a})}{\partial \mathrm{a}}dA_{\mathbf{x}} = \frac{1}{2}\oint_{\Omega(\mathrm{a})}\oint_{R(\mathrm{a})}\mathbf{f}(\boldsymbol{\eta},\boldsymbol{\xi})dA_{\mathbf{x}}\frac{\partial \hat{\mathbf{u}}}{\partial \mathrm{a}}dA_{\hat{\mathbf{x}}} \tag{3.9}$$

Defining the domain $Q(\mathrm{a}) = \Omega(\mathrm{a})\backslash R(\mathrm{a})$, the right hand side of Eq. (3.9) can be rewritten as

$$\frac{1}{2}\oint_{\Omega(\mathrm{a})}\oint_{R(a)}\mathbf{f}(\boldsymbol{\eta},\boldsymbol{\xi})dA_{\mathbf{x}}\frac{\partial \hat{\mathbf{u}}}{\partial \mathrm{a}}dA_{\hat{\mathbf{x}}} = \frac{1}{2}\oint_{Q(\mathrm{a})}\oint_{R(\mathrm{a})}\mathbf{f}(\boldsymbol{\eta},\boldsymbol{\xi})dA_{\mathbf{x}}\frac{\partial \hat{\mathbf{u}}}{\partial \mathrm{a}}dA_{\hat{\mathbf{x}}}$$

$$+\frac{1}{2}\oint_{R(\mathrm{a})}\oint_{R(\mathrm{a})}\mathbf{f}(\boldsymbol{\eta},\boldsymbol{\xi})dA_{\mathbf{x}}\frac{\partial \hat{\mathbf{u}}}{\partial \mathrm{a}}dA_{\hat{\mathbf{x}}} \tag{3.10}$$

Also, from Eq. (3.4), we have

$$\oint_{R(a)} \mathbf{f}(\boldsymbol{\eta},\boldsymbol{\xi})\, dA_{\hat{\mathbf{x}}} = -\oint_{Q(a)} \mathbf{f}(\boldsymbol{\eta},\boldsymbol{\xi})\, dA_{\hat{\mathbf{x}}} \tag{3.11}$$

By the change of variables $\hat{\mathbf{x}} \rightarrow \mathrm{x}$, using the linear admissibility condition Eq. (2.3) and employing Eq. (3.11), Eq. (3.10) can be written as

$$\begin{aligned}
&\frac{1}{2}\oint_{\Omega(a)} \oint_{R(a)} \mathbf{f}(\boldsymbol{\eta},\boldsymbol{\xi})\, dA_{\mathbf{x}}\, \frac{\partial \hat{\mathbf{u}}}{\partial a}\, dA_{\hat{\mathbf{x}}} \\
&\qquad = \frac{1}{2}\oint_{Q(a)} \oint_{R(a)} \mathbf{f}(\boldsymbol{\eta},\boldsymbol{\xi})\, dA_{\mathbf{x}}\, \frac{\partial \hat{\mathbf{u}}}{\partial a}\, dA_{\hat{\mathbf{x}}} + \frac{1}{2}\oint_{R(a)} \oint_{R(a)} \mathbf{f}(-\boldsymbol{\eta},-\boldsymbol{\xi})\, dA_{\hat{\mathbf{x}}}\, \frac{\partial \mathbf{u}}{\partial a}\, dA_{\mathbf{x}} \\
&\qquad = \frac{1}{2}\oint_{Q(a)} \oint_{R(a)} \mathbf{f}(\boldsymbol{\eta},\boldsymbol{\xi})\, dA_{\mathbf{x}}\, \frac{\partial \hat{\mathbf{u}}}{\partial a}\, dA_{\hat{\mathbf{x}}} - \frac{1}{2}\oint_{R(a)} \oint_{R(a)} \mathbf{f}(\boldsymbol{\eta},\boldsymbol{\xi})\, dA_{\mathbf{x}}\, \frac{\partial \hat{\mathbf{u}}}{\partial a}\, dA_{\hat{\mathbf{x}}} \\
&\qquad = \frac{1}{2}\oint_{R(a)} \oint_{Q(a)} \mathbf{f}(\boldsymbol{\eta},\boldsymbol{\xi}) \cdot \frac{\partial \hat{\mathbf{u}}}{\partial a}\, dA_{\hat{\mathbf{x}}} dA_{\mathbf{x}} + \frac{1}{2}\oint_{R(a)} \oint_{Q(a)} \mathbf{f}(\boldsymbol{\eta},\boldsymbol{\xi}) \cdot \frac{\partial \mathbf{u}}{\partial a}\, dA_{\hat{\mathbf{x}}} dA_{\mathbf{x}}
\end{aligned} \tag{3.12}$$

Substituting Eq. (3.12) into Eq. (3.8), we get

$$\oint_{R(a)} \frac{\partial W(\mathbf{x};a)}{\partial a} dA_{x} = \frac{1}{2}\oint_{R(a)} \oint_{\Omega(a)\setminus R(a)} \mathbf{f}(\boldsymbol{\eta},\boldsymbol{\xi}) \cdot \left(\frac{\partial \hat{\mathbf{u}}}{\partial a} + \frac{\partial \mathbf{u}}{\partial a}\right) dA_{\hat{\mathbf{x}}} dA_{\mathbf{x}} \tag{3.13}$$

Since the coordinates (x_1, x_2) are attached at the crack tip, and are defined by

$$\mathrm{x}_1 = \mathrm{X}_1 - a\,,\ \mathrm{x}_2 = \mathrm{X}_2$$

we have that $\dfrac{\partial \mathrm{x}_1}{\partial a} = -1$

By using the chain rule, we obtain

$$\frac{\partial \hat{\mathbf{u}}}{\partial \mathrm{a}} = -\frac{\partial \hat{\mathbf{u}}}{\partial \mathrm{x}_1}, \quad \frac{\partial \mathbf{u}}{\partial \mathrm{a}} = -\frac{\partial \mathbf{u}}{\partial \mathrm{x}_1} \tag{3.14}$$

Then, we place Eq. (3.14), (3.13), and (3.7) back into Eq. (3.6) to get the peridynamic *J*-integral formula as follow:

$$J_{peri} = \oint_{\partial R} W(\mathbf{x}; \mathrm{a})\mathbf{n}_1 dS - \frac{1}{2}\oint_{R(\mathrm{a})}\oint_{\Omega(\mathrm{a})\setminus R(\mathrm{a})} \mathbf{f}(\boldsymbol{\eta}, \boldsymbol{\xi})\cdot\left(\frac{\partial \hat{\mathbf{u}}}{\partial \mathrm{x}_1} + \frac{\partial \mathbf{u}}{\partial \mathrm{x}_1}\right) dA_{\mathbf{x}} dA_{\mathbf{x}} \tag{3.15}$$

where $W(\mathbf{x}; \mathrm{a})$ is the strain energy density ∂R is the integral contour. $R(\mathrm{a})$ is the region inside the integral contour, and $\Omega(a)\setminus R(a)$ is the region outside the integral contour (see Figure 3.1). Silling and Lehoucq [37] obtained the state-based peridynamic J-integral formulation based on an energy approach. We observe that in the particular case of the bond-based theory, the formula in [37] coincides with the one we obtained here in Eq. (3.15). Moreover, if there is no dissipation within the closed surface ∂R, then $J = 0$. So, R can be deformed to include any amount of additional material in which there is no dissipation occurring without changing the *J*-integral value. Thus, the peridynamic *J*-integral is path independent [37].

Discussion: The first term of peridynamic *J*-integral (see Eq. (3.15)) is a contour integral, along ∂R, where $R=R_1 \cup R_2$ (see red curve in Figure 3.2). The second term of the peridynamic J-integral is a double domain integral. This domain integral is zero unless the points in R are in R_2, and the points in $\Omega\setminus R$ are in R_3. Thus, Eq. (3.15) can be written as follows

$$J_{peri} = \oint_{\partial R} W(\mathbf{x};\mathrm{a})\mathbf{n}_1 dS - \frac{1}{2}\oint_{R_2}\oint_{R_3} \mathbf{f}(\boldsymbol{\eta},\boldsymbol{\xi})\cdot\left(\frac{\partial \hat{\mathbf{u}}}{\partial \mathrm{x}_1} + \frac{\partial \mathbf{u}}{\partial \mathrm{x}_1}\right) dA_{\mathbf{x}} dA_{\mathbf{x}} \tag{3.16}$$

Clearly, when the horizon δ goes to zero, the domain integral becomes a contour integral and the regions R_2 and R_3 reduce to the contour ∂R. In this case, the formulation of peridynamic *J*-integral coincides with the classical *J*-integral formula. Indeed, the peridynamic *J*-integral formulation when horizon goes to zero is

$$J_{peri} = \oint_{\partial R} W(\mathbf{x};\mathrm{a})\mathbf{n}_1 dS - \oint_{\partial R} \frac{\partial \mathbf{u}}{\partial \mathrm{x}_1} \bullet \boldsymbol{\tau}(\mathbf{x},\mathbf{n}) dS \tag{3.17}$$

where **τ**(**x**, **n**) is the force flux vector at any **x** in the direction of unit vector ***n*** normal to the tangent of the contour (see [54]).

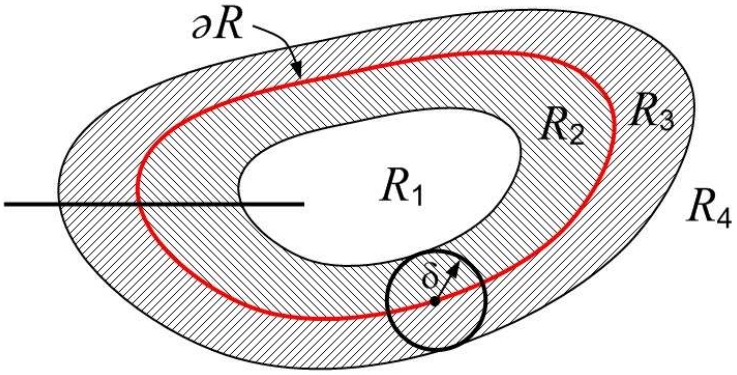

Figure 3.2. Integration domain (banded) for the peridynamic J-integral. The red curve is the contour of integration.

3.3 An algorithm for calculating the peridynamic *J*-integral

We use a uniform discretization with grid spacing Δx over the domain to compute the peridynamic *J*-integral. Using the mid-point integration scheme for the domain integral in Eq. (3.15) and the trapezoidal rule for the contour integral in Eq. (3.15) for the case when the contour is piecewise linear, leads to the following approximation

$$J_{peri} \approx \sum_{n=1}^{n_{boundary}} Wn_1 \Delta x - \frac{1}{2}\sum_{i=1}^{n_{inner}}\sum_{j=1}^{n_{outer}}\left(f(u_1^j - u_1^i, x_1^j - x_1^i)\times\left(\frac{\partial u_1}{\partial x_1} + \frac{\partial \hat{u}_1}{\partial x_1}\right)\right.$$

$$\left. + f(u_2^j - u_2^i, x_2^j - x_2^i)\times\left(\frac{\partial u_2}{\partial x_1} + \frac{\partial \hat{u}_2}{\partial x_1}\right)\right) A_j A_i \qquad (3.18)$$

where $n_{contour}$ and n_{inner} are the number of nodes along the integral contour boundary ∂R and the number of nodes in the inner region (the R_2 region in Figure 3.2), respectively. n_{outer} is the number of nodes in the outer region (the R_3 region in Figure 3.2). A_i is the nodal area or node i. The central difference scheme is used for $\partial \mathbf{u}/\partial x_1$ and $\partial \hat{\mathbf{u}}/\partial x_1$ as follows

$$\frac{\partial u_1(x_1^i, x_2^i)}{\partial x_1^i} \approx \frac{u_1(x_1^i + \Delta x, x_2^i) - u_1(x_1^i - \Delta x, x_2^i)}{2\Delta x},$$

$$\frac{\partial u_2(x_1^i, x_2^i)}{\partial x_1^i} \approx \frac{u_2(x_1^i + \Delta x, x_2^i) - u_2(x_1^i - \Delta x, x_2^i)}{2\Delta x},$$

$$\frac{\partial \hat{u}_1(x_1^j, x_2^j)}{\partial x_1^j} \approx \frac{\hat{u}_1(x_1^j + \Delta x, x_2^j) - \hat{u}_1(x_1^j - \Delta x, x_2^j)}{2\Delta x},$$

$$\frac{\partial \hat{u}_2(x_1^j, x_2^j)}{\partial x_1^j} \approx \frac{\hat{u}_2(x_1^j + \Delta x, x_2^j) - \hat{u}_2(x_1^j - \Delta x, x_2^j)}{2\Delta x}.$$

We compute the peridynamic J-integral with the following algorithm based on Eq. (3.18).

Table 3.1. Algorithm to compute the peridynamic J-integral.

1:	Get the nodal displacements and elastic strain energy density at all nodes.
2:	Define the geometry of the integral contour.
3:	Compute the first term (contour integral) of the peridynamic J-integral
	(a) Find nodes along the contour ∂R and the corresponding outer normal vector to the integral contour at such nodes.
	(b) Evaluate the line integral using trapezoidal rule.
4:	Compute the second term (domain double integral) of the peridynamic J integral
	(a) Define the inner region (R_2): one horizon size inside of the integral contour ∂R.
	(b) Define the outer region (R_3): one horizon size outside of the integral contour ∂R.
	(c) Search all viable source nodes $\mathbf{x}^i$ in inner region.
	(d) Search all viable nodes $\mathbf{x}^j$ in outer region.
	(e) Compute the second term based on the discretization in Eq. (3.18).
5:	J_{peri} = First_term – Second_term.

3.4 Numerical results: convergence studies, path-independence, and effects from the boundaries

As we discussed in section 2.4, two types of convergence studies are typically used: the δ-convergence (fix the number of nodes covered by a horizon, which is proportional to $m = \delta / \Delta x$, and decrease the horizon size), and *m*-convergence (keep the horizon size fixed

and increase *m*). Here we perform convergence studies for a plate without notch to test the correctness of the implementation. Then, we perform convergence studies to investigate for what horizon size, relative to the size of the sample, and which *m*-values does the peridynamic *J*-integral get close (with a relative difference of a few percentages) to the classical value of the J-integral. We analyze the influence of boundary conditions (when symmetry conditions are used) and of the peridynamic "skin effect" on the nonlocal *J*-integral. We compare the peridynamic results with the classical *J*-integral value as approximately given by Finite Element results using Abaqus with special crack-tip elements for a plate with an edge notch under tension. In order to investigate how symmetric boundary conditions influence the peridynamic *J*-integral value we analyze a double-edge notch plate under uniform tension, for which we use symmetry boundary conditions. We also perform calculations that show the path-independence of the peridynamic *J*-integral.

In following examples, we use the same material parameters: Young's modulus is 72GPa and Poisson's ratio is 1/3. Along top and bottom boundaries of the two different samples, a uniform tensile stress $\sigma = 1$ MPa is applied. Uniform discretization is used for all computations. We use the "conical" micromodulus functions given below (see Figure 3.3) since it gives better convergence rates to the classical (local) solutions in elasticity problems compared to the simpler, constant micromodulus (see [48], [15]).

$$c(\|\boldsymbol{\xi}\|) = C_1(1-\frac{\|\boldsymbol{\xi}\|}{\delta}) = \frac{24E}{\pi\delta^3(1-\nu)}(1-\frac{\|\boldsymbol{\xi}\|}{\delta}) \tag{3.19}$$

where E and ν are Young's modulus and Poisson's ratio, respectively. δ is horizon size.

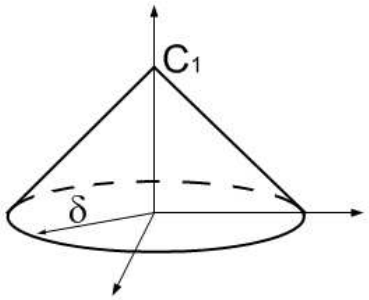

Figure 3.3. The conical micromodulus function.

3.4.1 Benchmark test

Consider a square plate with dimension of 10 cm x 10 cm, as shown in Figure 3.4. We choose an arbitrary point (see Point P in Figure 3.4) in the bulk to compute the elastic strain for different horizon size and m by using the central difference scheme, and then compare with the classical analytical solution (1.389×10^{-5}).

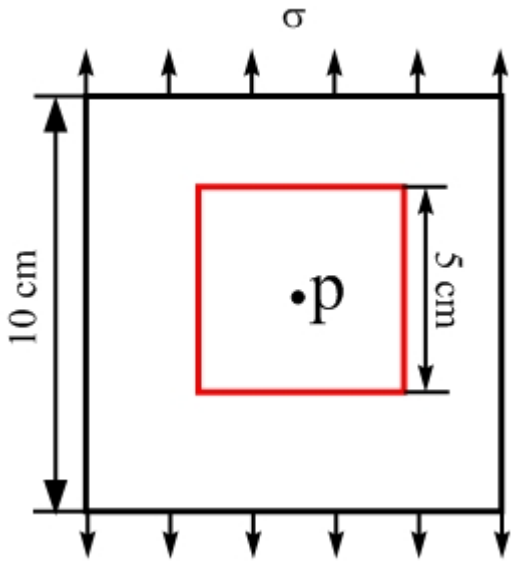

Figure 3.4. Geometry configuration. The red square is the integral contour.

Table 3.2. The convergence studies of elastic strain for point P.

	δ = 24 mm	δ = 12 mm	δ = 6 mm	δ = 3 mm	δ = 1.5 mm
$m = 3$	1.290×10^{-5}	1.332×10^{-5}	1.353×10^{-5}	1.363×10^{-5}	1.368×10^{-5}
$m = 6$	1.294×10^{-5}	1.338×10^{-5}	1.360×10^{-5}	1.371×10^{-5}	1.377×10^{-5}
$m = 9$	1.295×10^{-5}	1.339×10^{-5}	1.363×10^{-5}	1.374×10^{-5}	1.380×10^{-5}

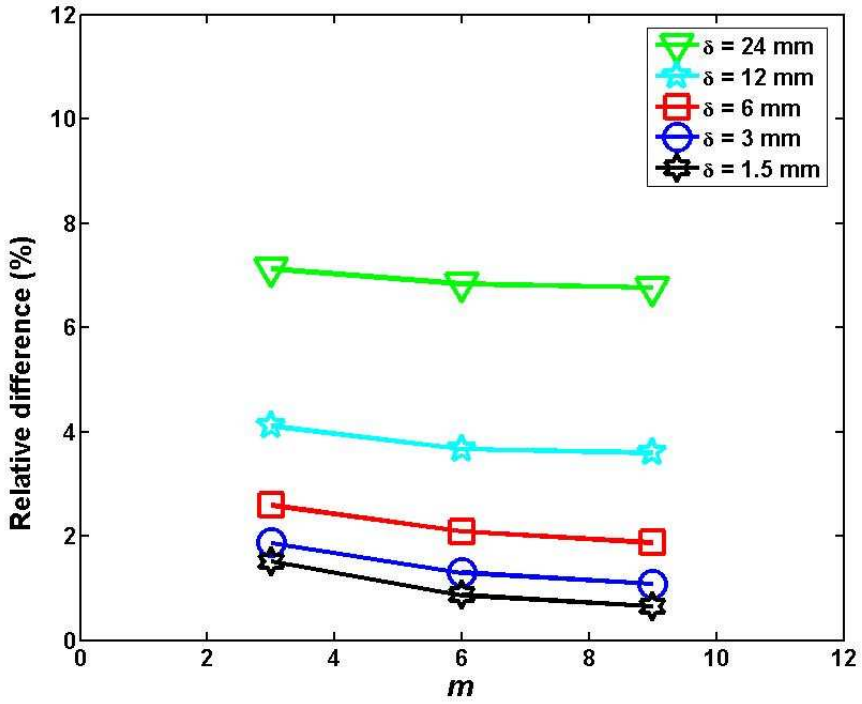

Figure 3.5. The relative difference between the peridynamic results for the vertical strain at Point P in Figure 3.4 and the analytical solution for the classical theory.

Two types of convergence studies (*m*-convergence and δ-convergence) are shown in Table 3.2 and the relative difference between peridynamic results and classical solution are shown in Figure 3.5. For a fixed *m*, the elastic strain from peridynamics approaches the classical solution when the horizon size decreases, so we do observe δ - convergence to the classical elastic strain in the limit of the horizon going to zero.

Then, we use the square contour shown in Figure 3.4 to compute the peridynamic *J*-integral. In this case, peridynamic J-integral values are in the range of 10^{-15} for any *m*-values and horizon size we tried. For instance, the peridynamic *J*-integral value is 3.3 x

10^{-15} Pa·m for $m = 9$ and $\delta = 1.5$ mm. The results coincide with theoretical value of zero, since the *J*-integral value on a closed contour in an elastic material without a crack is zero.

3.4.2 Single edge-notch specimen

Consider a single edge-notch square plate with dimension of 10 cm x 10 cm with a length of the notch of 5 cm, as shown in Figure 3.6. We use the square contour shown in Figure 3.6 to compute the peridynamic *J*-integral and the corresponding classical value with Abaqus. In Abaqus, we use the "seam crack" option to create the crack and use special crack-tip quadratic elements around the crack tip as shown in Figure 3.7. In the actual FEM computation, the total number of nodes is about 30000 (many more nodes than shown in Figure 3.7), which gives us a converged value for the classical *J*-integral of about 19.76 Pa·m.

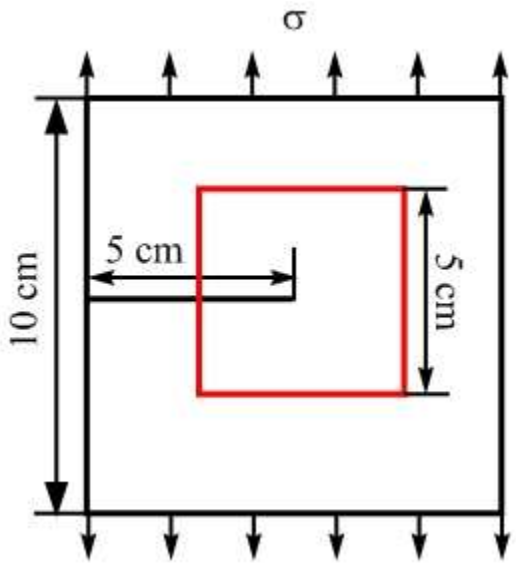

Figure 3.6. Geometry configuration for single edge-notched plate

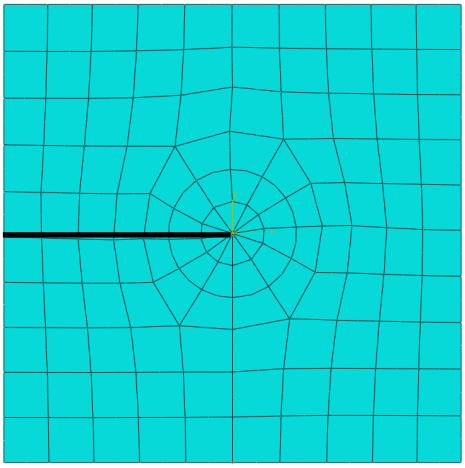

Figure 3.7. A sample Abaqus mesh with special elements around the crack tip, used to compute the classical *J*-integral value. The dark solid line is the crack.

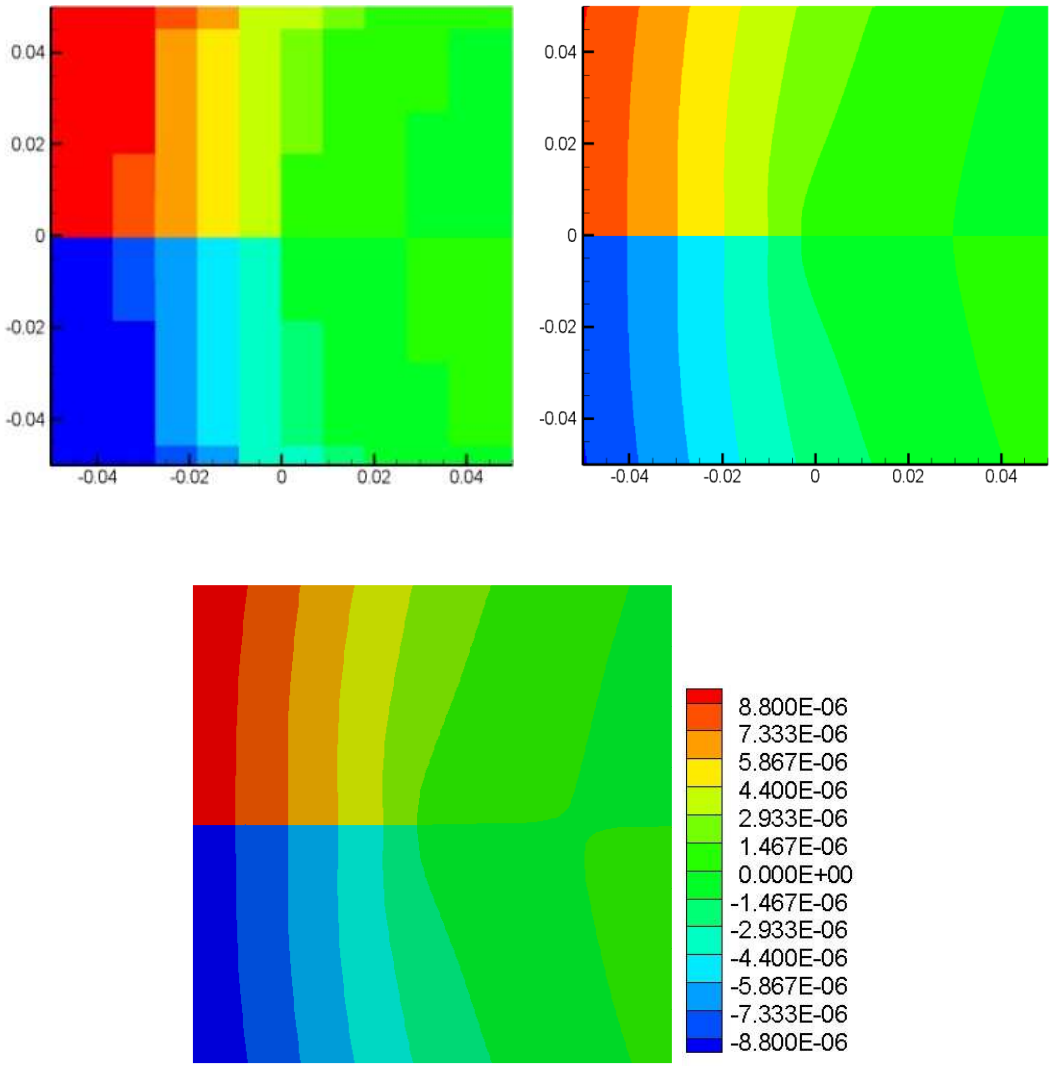

Figure 3.8. Comparison of vertical displacements obtained with: (a) peridynamics using δ = 24mm, m = 3 (about 144 nodes), (b) peridynamics using δ = 1.5mm, m = 9 (about 360000 nodes), and (c) the FEM (about 30000 nodes).

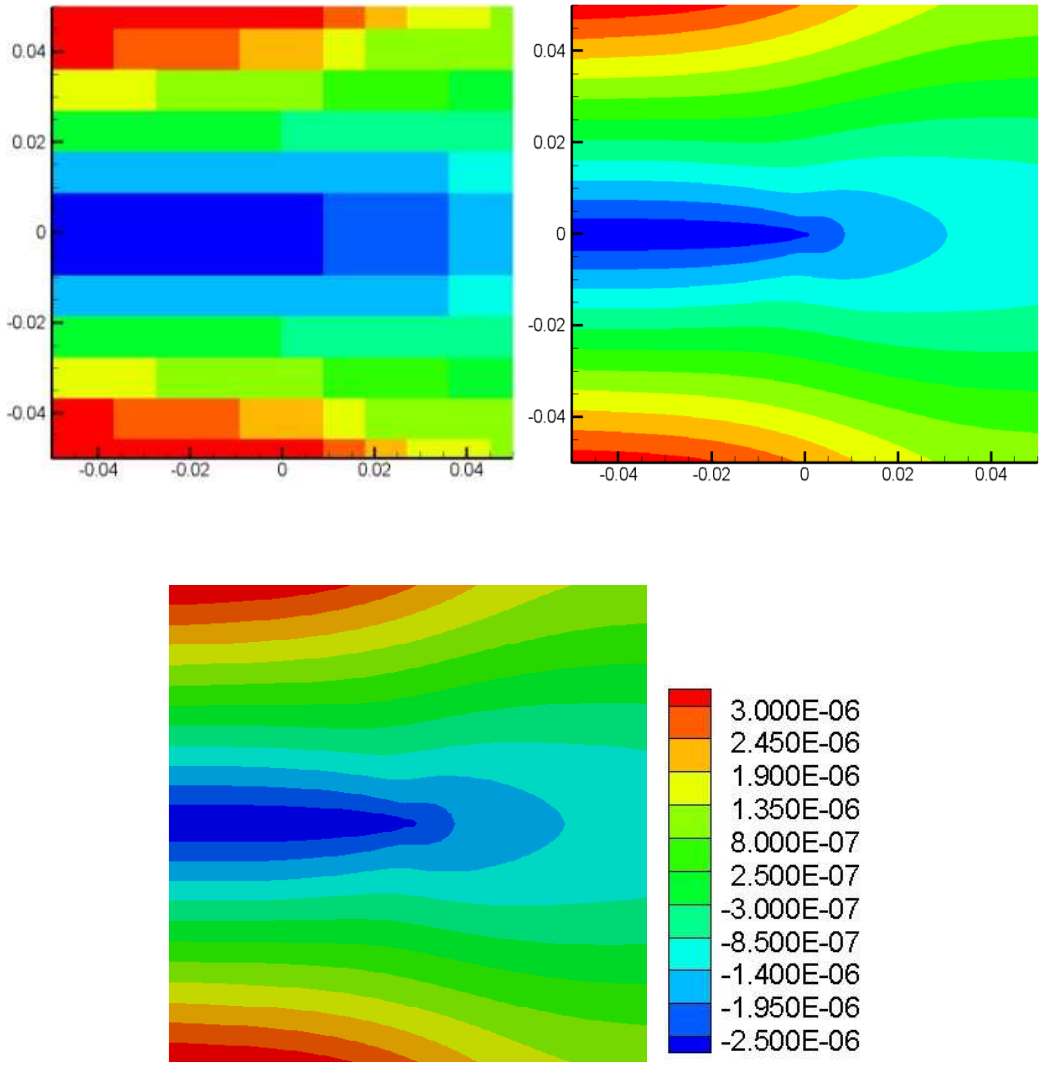

Figure 3.9. Comparison for horizontal displacements obtained with: (a) peridynamics using δ = 24mm, m = 3; (b) peridynamics using δ = 1.5mm, m = 9, and (c) the FEM.

Since the *J*-integral involves the components of the displacement field, it is of interest to compare the displacements obtained from peridynamics with a "large" and a "small" horizon size with the classical displacements obtained from a sufficiently fine FEM mesh. As shown in Figure 3.8 and Figure 3.9, the vertical and horizontal-displacements from the peridynamic computation are almost identical to the FEM

calculations when the horizon size, relative to the sample size and crack size is below 1/20. In these figures the same legend is used for both the peridynamic results and the finite element results.

Table 3.3. Peridynamic *J*-integral values for the single edge-notch specimen

	δ = 24 mm	δ = 12 mm	δ = 6 mm	δ = 3 mm	δ = 1.5 mm
m = 3	30.15 Pa·m	23.64 Pa·m	21.74 Pa·m	20.83 Pa·m	20.41 Pa·m
m = 6	26.52 Pa·m	23.05 Pa·m	21.54 Pa·m	20.85 Pa·m	20.51 Pa·m
m = 9	26.17 Pa·m	22.95 Pa·m	21.53 Pa·m	20.86 Pa·m	20.53 Pa·m

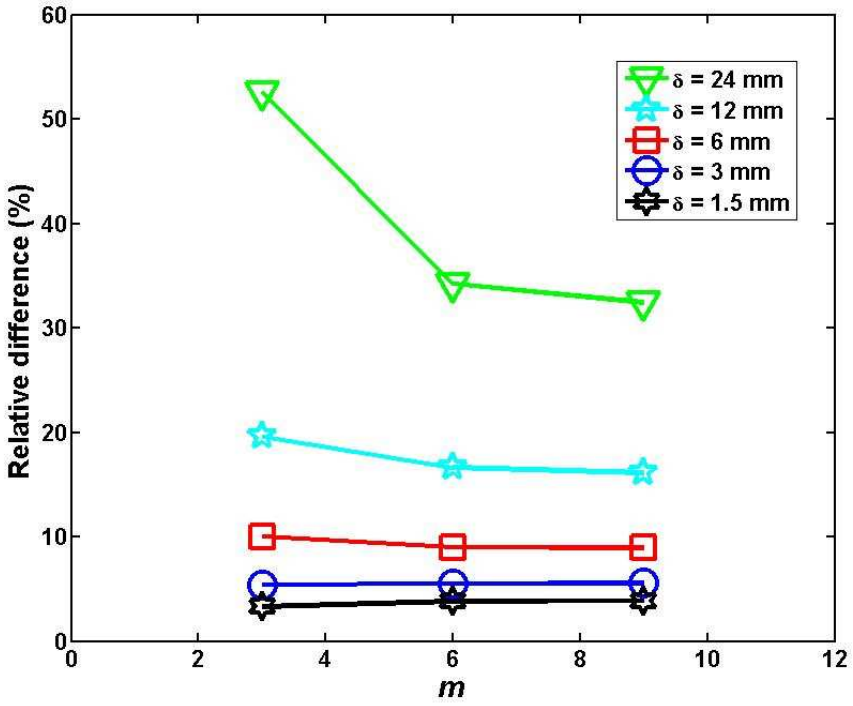

Figure 3.10. The relative difference between the peridynamic results for the single-notch sample and the classical *J*-integral obtained with the FEM (Abaqus).

Two types of convergence studies (*m*-convergence and δ-convergence) are shown in Table 3.3 and Figure 3.10. For a fixed *m*, the peridynamic *J*-integral approaches the classical solution when the horizon size decreases, so we do observe δ - convergence to the classical *J*-integral value. We also note that the m-convergence curves (for a fixed δ) start to level off when *m* becomes larger than 6. Increasing *m* for a fixed horizon size delivers solutions that approach the exact nonlocal solution. The results of Figure 3.10 indicate good candidates for both δ and *m* to use in order to obtain the peridynamic *J*-integral values within a few percentages from the FEM results. We stress that, in general, the FEM results may also be a few percentages away from an analytical solution of the classical model. Thus, when the intention is to obtain peridynamic *J*-integral values close to the classical ones, an *m* of about 6 and a horizon size smaller than 6 mm (a ratio of at least 1/10 to the crack length, and 1/20 to the sample dimensions) are good choices.

Remark: the peridynamic "skin effect" mentioned in section 2 exists on the crack surfaces. Hence, we expect peridynamic *J*-integral results to be higher than the FEM results since we effectively have a slightly softer material around the crack tip than the material in the bulk. We assigned a softer material to a thin region around the crack line in the FEM model and the J-integral value from Abaqus calculation increased by about 2%.

3.4.3 Double edge-notch specimen

In this section, we consider a double-notch plate with dimensions 20 cm x 10 cm. The length of each notch is 5 cm. We could use full dimension to perform the convergence studies, but we are not able to study the boundary conditions influence the *J*-integral values. By making use of symmetry, we can reduce the problem to analyzing the same configuration as before except that now we impose symmetry conditions on the displacements along the right-hand boundary (see Figure 3.11).

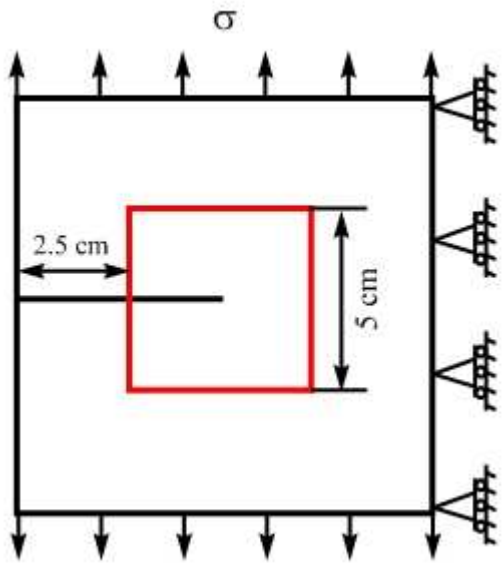

Figure 3.11. double edge notched specimen with symmetric boundary conditions and the *J*-integral contour.

We use the same integral contour as in section 3.4.2 and three different horizon sizes δ = 6 mm, δ = 3 mm, and δ = 1.5 mm and m = 3, 6, and 9 to observe how convergence is influenced by the presence of the symmetry boundary condition. While in a classical model discretized with finite elements the symmetry boundary condition is simply

imposed on the boundary nodes where zero horizontal displacements are enforced, in a nonlocal peridynamic model this type of condition is more delicate. In principle, in the discrete peridynamic model we should enforce the boundary nodes to have zero horizontal displacements, but in addition to that, for a sliver of thickness δ on the corresponding boundary we should also prescribe the horizontal displacement field (see [28] for a discussion on nonlocal Dirichlet boundary conditions). The problem is that we do not know those values. Ways around this are possible: for example, we could set horizontal displacements to zero for all nodes in the region of thickness δ, and in the limit of the horizon going to zero we will approach the actual symmetry condition desired; alternatively, we could impose zero horizontal displacements only on the boundary nodes, just like in finite element approximations. We choose the latter strategy because of simplicity and similarity to the way boundary conditions are imposed for the classical model.

The finite element solution for the classical *J*-integral value from Abaqus with special crack-tip elements is 12.90 Pa·m.

As shown in Figure 3.12, the strain energy density obtained with peridynamics for a sufficiently small horizon size is very close to that given by a converged FEM solution. However, some high strain energy density values are observed from the peridynamic result on the right-hand boundary, where the symmetric boundary condition is applied (see Figure 3.12). This influences, to a certain extent, the results for the *J*-integral, as we will see below. We also notice that the difference in brightness between the FEM and

peridynamics results are not due to differences in the values, but are caused by differences in the colors used by Abaqus (for the FEM results) and Tecplot (which we used to post-process the peridynamic results).

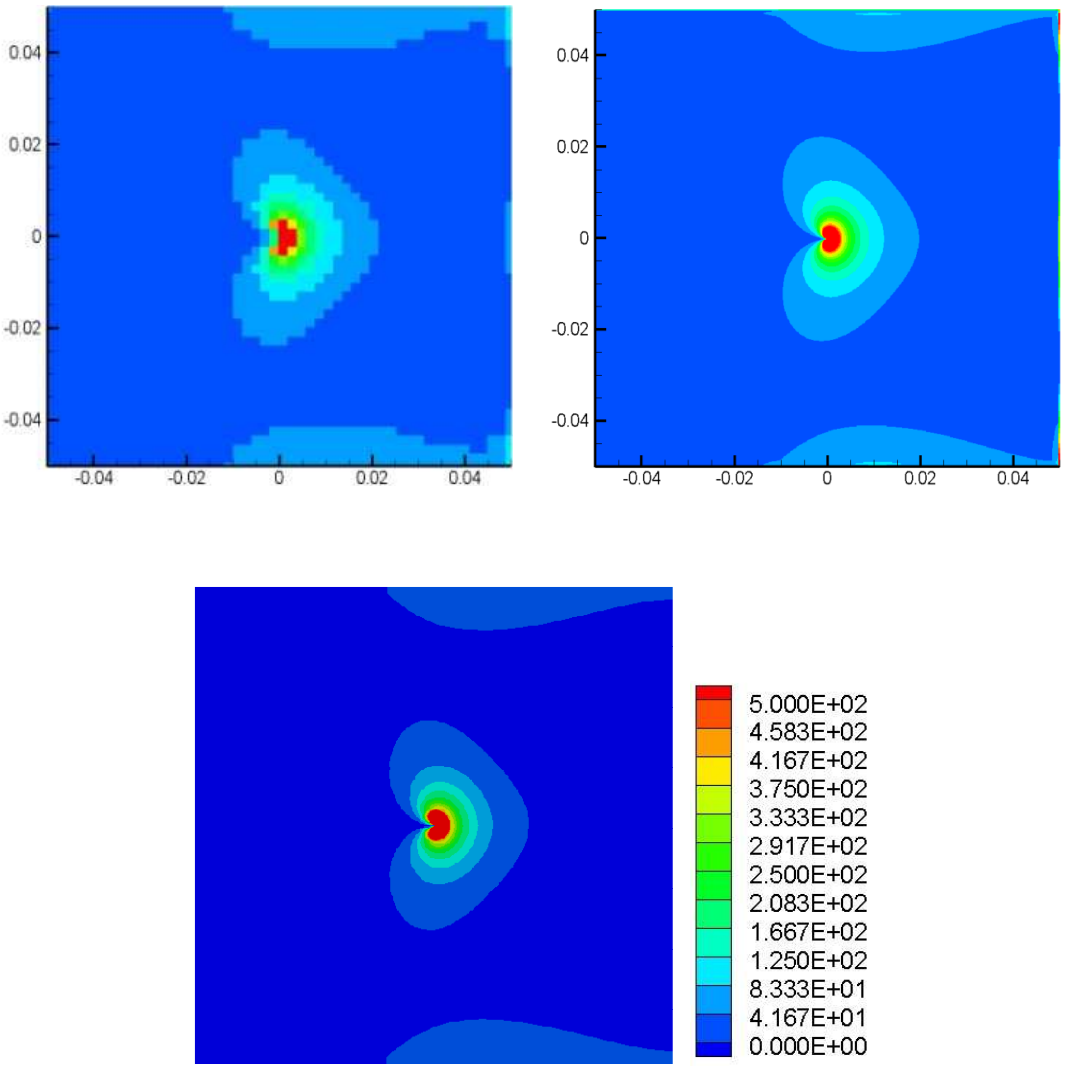

Figure 3.12. Strain energy density results with: (c) peridynamics with δ = 6 mm, m = 3 (about 2700 nodes); (b) peridynamics with δ = 1.5 mm, m = 9 (about 360000 nodes); (a) FEM (30000 nodes).

Table 3.4. Convergence study for the *J*-integral value for the double edge-notch specimen.

	δ = 6 mm	δ = 3 mm	δ = 1.5 mm
m = 3	14.83 Pa·m	14.01 Pa·m	13.58 Pa·m
m = 6	15.49 Pa·m	14.50 Pa·m	13.99 Pa·m
m = 9	15.90 Pa·m	14.77 Pa·m	14.17 Pa·m

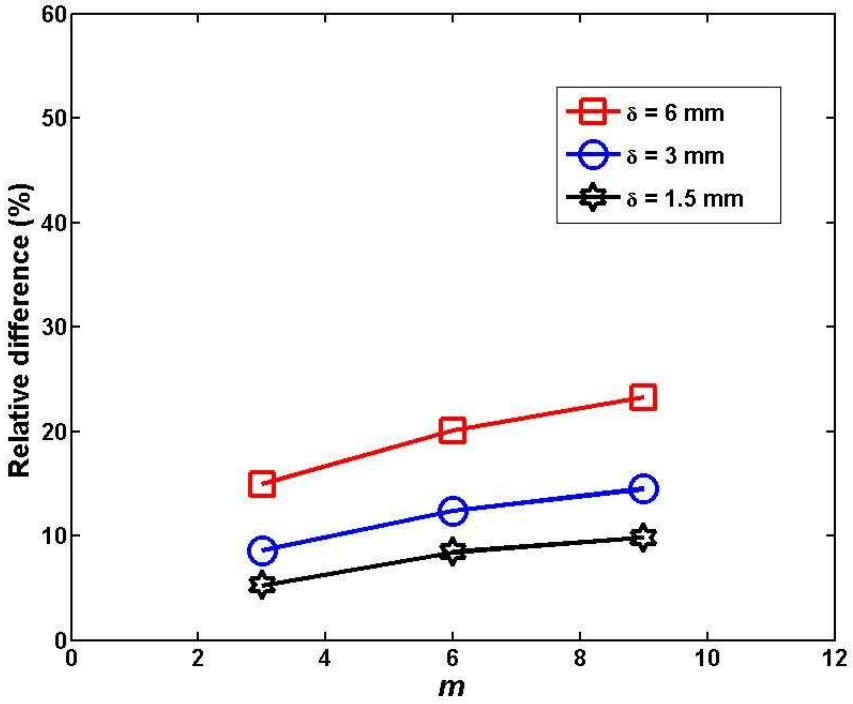

Figure 3.13. The relative difference between peridynamic results for the double edge-notch (with symmetric boundary conditions) and the classical *J*-integral value obtained from a FEM (Abaqus) analysis.

The *m*-convergence trends are the same for all three cases as shown in Figure 3.13. The peridynamic solutions are all larger than the FEM result, which is consistent with the results obtained in section 3.4.2. The effectively softer material around the crack tip (induced by the peridynamic "skin effect") is responsible for this. For a given *m*-value,

the smaller the horizon size the closer the peridynamic result is to the classical value, confirming that with a horizon size sufficiently small, the relative difference between the classical *J*-integral value and the peridynamic *J*-integral is smaller than a few percentages. However, for the fixed horizon size and increase *m* the peridynamic results will converge to the exact solution of nonlocal problem (see [55], [56]). The question whether the imposition of the symmetry boundary conditions influences the calculation of the peridynamic *J*-integral is answered in the next section.

3.4.4 Studies of path-independence of the peridynamic *J*-integral

We test here different contours to observe if, and by how much, the value of the peridynamic *J*-integral changes with the change in contour. For these tests we use the smallest horizon and finest grid from the computations above ($m = 9$ and $\delta = 1.5$ mm) and perform calculations for the single edge-notch problem and the double edge-notch problem with symmetry boundary conditions. We use three different contours shown in Figure 3.14: the closest contour to the crack tip that remains feasible from the point of view of evaluating the integrals in Eq. 3.15 (see also Figure 3.14), one away from the crack tip and the boundaries, and one near the boundaries, but at least one horizon size away from the boundaries to remain feasible. Thus, contour (a) in Figure 3.14 is one horizon size away from the crack tip, contour (b) is in the middle of the structure, and contour (c) is one horizon away from the boundary of the sample.

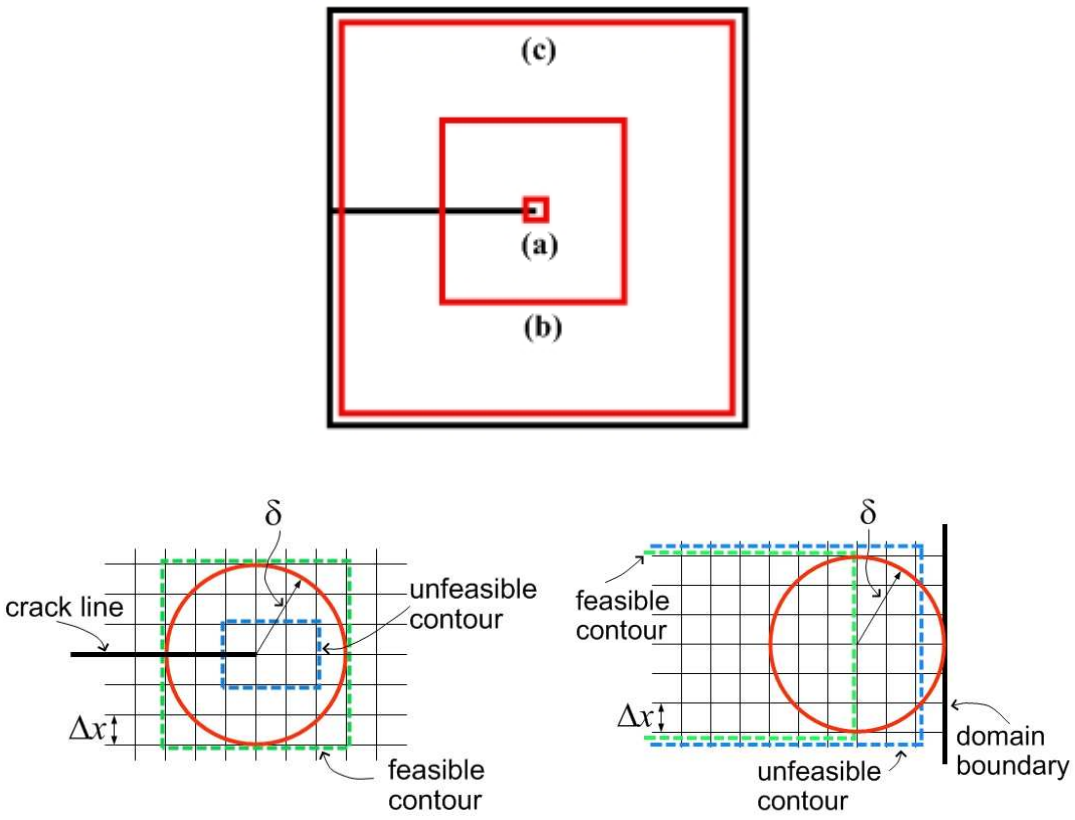

Figure 3.14. Three different integral contours to compute peridynamic *J*-integral (top). Feasible and unfeasible contours (bottom row) for the computation of the nonlocal *J*-integral near the crack tip and near a domain boundary.

Table 3.5. Values of the peridynamic *J*-integral on the three different contours from Figure 3.14.

	Contour (a)	Contour (b)	Contour (c)
Single edge-notch	20.11 Pa·m	20.54 Pa·m	19.84 Pa·m
Double edge-notch (using symmetric b.c.'s)	13.88 Pa·m	14.17 Pa·m	13.37 Pa·m

We measure the relative difference between the values obtained based on contour (b) and those on contours (a) and (c). As shown in Table 3.6, the relative differences between

contour (a) and contour (b) for both the single edge-notch and double edge-notch specimens are very similar, of about 2%. However, the relative difference between contour (c) and contour (b) is larger in the double-edge case (with symmetric boundary conditions) than in the single edge-notch case. The reason is likely the way the nonlocal Dirichlet boundary condition is enforced and the peridynamic "skin-effect". Notice that the results on contour (c) are actually closer to the classical results obtained with the FEM, but these trends should not be misinterpreted. The horizon size, number of nodes inside the horizon, and the type of boundary conditions all "influence" the nonlocal results which may be lower than a classical value for some *m*-values and higher for some other *m*-values. We recall that in *m*-convergence, as *m* tends to infinity, the numerical approximation is supposed to approach the exact solution of the nonlocal problem and not the exact solution of the classical problem. It is known that nonlocal results may be closer to the classical results for some δ_1 and m_1, and higher for a $\delta_2 < \delta_1$ and $m_2 > m_1$, thus leading to the exact classical solution for some δ_3 in $[\delta_2, \delta_1]$ and m_3 in $[m_1, m_2]$ (see also [55], [56]).

Table 3.6. Relative difference of the peridynamic *J*-integral on contours (a) and (c) in Figure 3.14 from the values obtained on contour (b).

	Contour (a)	Contour (c)
Single edge-notch	2.09%	3.41%
Double edge-notch (using symmetric boundary conditions)	2.05%	5.65%

In conclusion, a contour for computing the peridynamic *J*-integral needs to avoid the boundary region because of the skin effect. On the other hand, the contour may be

selected near the crack tip, with the only condition being the feasibility requirement as shown in Figure 3.14.

3.5 Summary

We derived the 2D peridynamic *J*-integral formulation based on the infinitesimal virtual extension of the mode-I crack. We discussed the computation of the peridynamic *J*-integral value which involves a double integral in contrast with the classical *J*-integral. We showed that the peridynamic *J*-integral will converges to the classical *J*-integral formulation when the horizon size goes to zero. Using a simple discretization, we performed convergence studies (*m*-convergence and δ-convergence) for two specimens: a single edge-notch and a double edge-notch sample, for which symmetry boundary conditions were enforced. We observed that the peridynamic results approach within a few percentages the classical *J*-integral values obtained using the FEM with special element around the crack tip, when the horizon size is less than about 1/20 of the crack size and sample size. In particular, we discuss the influence of the peridynamic "skin-effect" around the crack tip and along the boundaries on the value of the peridynamic *J*-integral. We computed the peridynamic *J*-integral along with different paths and small variations are seen (attributable to the approximation error) between the contour, except when the integration path is near the boundaries. Special care also needs to be paid when symmetric boundary conditions are imposed.

Chapter 4
Modeling of dynamic fracture in unidirectional composite materials

In this chapter, we propose a peridynamic formulation for a unidirectional (UD) fiber-reinforced composite (FRCs) lamina based on homogenization and mapping between elastic and fracture parameters of the micro-scale peridynamic bonds and the macro-scale parameters of the composite. We propose a computational method for a homogenized peridynamics description of fiber-reinforced composites and we use it to simulate dynamic brittle fracture and damage in these materials. With this model we analyze the

dynamic effects induced by different types of dynamic loading on the fracture and damage behavior of unidirectional fiber-reinforced composites.

4.1 Introduction

New aerospace structures, like the new Boeing-787 airplane, are incorporating more fiber-reinforced composites in their design [57]. The types of dynamic loading conditions that these and other similar composite structures undergo during their service life justify the need for dynamic analysis of fracture and failure in composite materials. As demonstrated by recent experimental observations ([6], [7]), the dynamic failure behavior of these materials is extremely complicated and a full understanding of the damage processes and mechanisms of failure in FRCs is currently lacking. Fracture in FRCs has been experimentally studied predominantly under quasi-static conditions ([58], [59], [60], [61], [38], [39]).

Significantly fewer experiments report on dynamic fracture in FRCs. There are some difficulties to perform experiments in composite materials with dynamic tensile loadings. Generating a tensile pulse and specimen gripping [62] are two of the difficulties in dynamic tensile loading of composites. However, some studies ([6],[7]) show that dynamic loading leads to dramatically different fracture behavior compared with quasi-static conditions. Dynamic experiments are conducted in [6] with different strain rates from low (10^{-4} s^{-1}) to high (10^{2} s^{-1}) for glass/vinylester composites. The observations show that the dynamic damage behavior and failure patterns are highly sensitive to strain

rates. Extensive fracture and damage produced by interconnected splitting, matrix cracking, delamination, and fiber breakage, are observed under higher strain rates. Damage and failure in S2-glass/vinylester UD composites is induced using the Split-Hopkinson-Pressure-Bar technique in [7], where the authors investigate cracking behavior under different strain rates. Haque et al. [7] observe matrix cracking and debonding for loading UD FRCs in the transverse direction. Interestingly, at higher levels of loading the straight splitting cracks branch in the matrix in a similar way seen in isotropic materials [63] and the angle of branching (the angle between a branch and the original propagation direction) is close to 45°. This branching phenomenon happens in the matrix only, the fibers do not break and the matrix cracks "migrate" over the fibers. These results show that the crack path is highly sensitive to the loading conditions, and that the dynamic fracture behavior in composites is completely different from that observed under quasi-static loading. While limited in their number, the experimental observations for dynamic fracture in UD FRCs reveal that different fracture modes coexist when the loading is dynamic and that a complex and rich strain-rate dependent damage behavior occurs.

Significant efforts have been made to model damage and failure in FRCs based on classical elasticity, the Finite Element Method and damage or fracture models ([38], [39], [40]). For the most part, these efforts have addressed quasi-static loading conditions. Tay et al. [64] gives a comprehensive review of modeling failure, delamination, and splitting in FRCs based on the element failure method. As mentioned in [65], such treatments of fracture in composites require prior knowledge of the actual fracture modes and of the

crack paths. As discussed above, for dynamic loading conditions the fracture modes and the crack paths are part of the solution and thus, these classical models cannot be very useful except in special situations. Recently, for example, Guimard et al. [65] used an interfacial Continuum Damage Model to study the rate effects for a setup in which a single failure mode (delamination) is active and the crack path is straight. As indicated by dynamic experiments under more general conditions [7], different failure modes coexist and are coupled in dynamic fracture of UD FRCs. The dynamic interactions among matrix cracking, splitting, delamination and stress waves determine the dynamic fracture and failure behavior in such composites. Therefore, models that intend to predict this complex behavior need to:

1. Obtain the crack paths, and their kinetics as part of the solution, and

2. Allow for the autonomous interaction between stress waves, cracks, and fracture modes.

Peridynamics has been extended to model the fracture and damage of composite materials. Xu et al. ([43],[32]) use such a peridynamic model to simulate the damage patterns in laminated composites subjected to bi-axial loading and low-velocity impact. The details of the model are, however, not given in ([43],[32]). An explicit model of fibers and matrix material is employed in [33] for damage and failure in composites under quasi-static loadings. The authors of [33] observed that homogenized models would not be able to capture the splitting fracture mode and thus they explicitly modeled individual fibers with peridynamics.

In following section, we presented a homogenization-based peridynamic formulation for a unidirectional fiber-reinforced composite lamina and provided analytical formulas for the parameters used. In the discrete version of the model, scaling of the peridynamic micro-moduli is required in order to maintain the strain energy of the numerical model under grid refinement the same. We will show that it is possible to successfully use homogenization to model fracture and damage in fiber-reinforced composites using peridynamics.

4.2 Classical mechanics of composite material

A unidirectional (UD) composite lamina is a planar arrangement of unidirectional fibers strongly bonded in a matrix. At the macro-mechanical level, the fiber-reinforced UD composite is an orthotropic, homogeneous, linearly elastic material [66].

Thus, for the lamina, the constitutive equation can be written in the following matrix form:

$$\begin{bmatrix} \sigma_1 \\ \sigma_2 \\ \sigma_3 \\ \sigma_4 \\ \sigma_5 \\ \sigma_6 \end{bmatrix} = \begin{bmatrix} C_{11} & C_{12} & C_{13} & 0 & 0 & 0 \\ C_{12} & C_{22} & C_{23} & 0 & 0 & 0 \\ C_{13} & C_{23} & C_{33} & 0 & 0 & 0 \\ 0 & 0 & 0 & C_{44} & 0 & 0 \\ 0 & 0 & 0 & 0 & C_{55} & 0 \\ 0 & 0 & 0 & 0 & 0 & C_{66} \end{bmatrix} \begin{bmatrix} \varepsilon_1 \\ \varepsilon_2 \\ \varepsilon_3 \\ \varepsilon_4 \\ \varepsilon_5 \\ \varepsilon_6 \end{bmatrix} \tag{4.1}$$

where the Voigt notation is used for a single subscript notation for stress and strain.

In this research, we will use 2-D plane stress model. 2-D plane stress constitutive equation for UD composites can be written as

$$\begin{bmatrix}\sigma_1\\ \sigma_2\\ \sigma_3\end{bmatrix}=\begin{bmatrix}C_{11} & C_{12} & 0\\ C_{12} & C_{22} & 0\\ 0 & 0 & C_{66}\end{bmatrix}\begin{bmatrix}\varepsilon_1\\ \varepsilon_2\\ \varepsilon_3\end{bmatrix} \tag{4.2}$$

Connections between the properties of the fibers and the matrix and the effective properties of the lamina can be expressed, for example, by using the Halpin-Tsai relationships ([67]):

$$E_{11}=V_{fiber}E_{fiber}+V_{matrix}E_{matrix},\quad \frac{1}{E_{22}}=\frac{V_{fiber}}{E_{fiber}}+\frac{V_{matrix}}{E_{matrix}},$$

$$\nu_{12}=V_{fiber}\nu_{fiber}+V_{matrix}\nu_{matrix},\quad V_{fiber}+V_{matrix}=1, \tag{4.3}$$

$$G_{12}=G_{fiber}G_{materix}/\left(V_{fiber}G_{matrix}+V_{matrix}G_{fiber}\right),$$

where E_{11} and E_{22} are the longitudinal and transverse elastic Young's modulus in the principal material axes, respectively. ν_{12} is the longitudinal Poisson's ratio and ν_{12} is the transverse Poisson's ratio. G_{12} is the elastic shear modulus. E_{fiber}, E_{matrix}, ν_{fiber}, ν_{matrix}, V_{fiber}, V_{matrix}, G_{fiber}, and G_{matrix} are the fiber and matrix Young's moduli, fiber and matrix Poisson's ratio, fiber volume fraction and matrix volume fraction, fiber and matrix shear modulus, respectively.

4.3 Peridynamic model for a unidirectional composite lamina

In this section, we present a new formulation for modeling fiber-reinforced composites based on a homogenization procedure similar to the one performed for isotropic materials but applied here for the elastic deformation of the UD composite lamina. We assume that strain energy in the longitudinal direction is a result of contributions from peridynamic "fiber bonds" while the strain energy along the transverse direction comes from the "matrix bonds". To arrive at a homogenized model for the lamina we follow a procedure schematically shown in Figure 4.1. The peridynamic bonds at a point in the anisotropic peridynamic material will have different properties along the longitudinal direction than along all other directions.

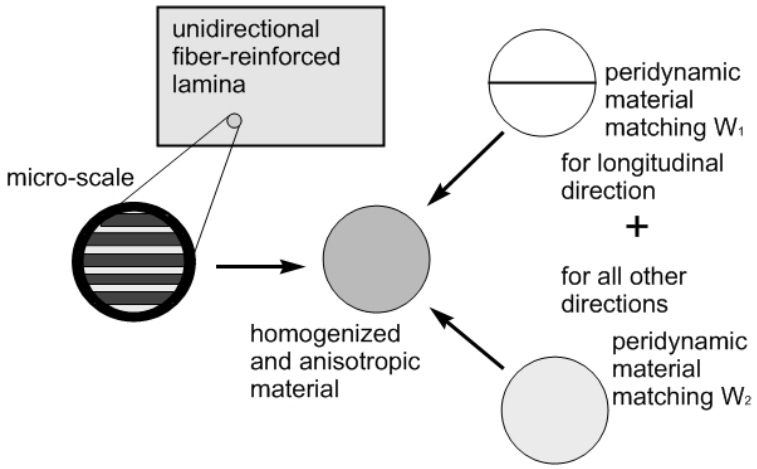

Figure 4.1. Schematic of the homogenization procedure.

Remark: We call the peridynamic bonds aligned with the fiber direction "fiber bonds" and all other bonds "matrix bonds". It is important to emphasize that the "fiber

bonds" properties are not matched to the actual fiber properties, but are calibrated to the analytical effective elastic properties of the composite lamina along the fiber direction. The same is true for the "matrix bonds".

To compute the strain energy density along the longitudinal deformation we need to make use of the Dirac-delta function. For a given homogeneous deformation, we match the strain energy of the material along the longitudinal direction with the strain energy of homogenized anisotropic peridynamic material along the same direction. Along the transverse direction we do the same.

Given a homogeneous bi-axial deformation of size *s* aligned with the longitudinal and the transverse directions, the peridynamic elastic strain energy density of the UD composite can be written as:

$$W_1 = \frac{1}{2}\int_H \omega_{fb}(\boldsymbol{\eta},\boldsymbol{\xi})[D(\|\boldsymbol{\xi}\|,0) + D(\|\boldsymbol{\xi}\|,\pi)]dA_\xi = \frac{1}{2}\int_{-\delta}^{\delta} \omega_{fb}(\boldsymbol{\eta},\boldsymbol{\xi})d\boldsymbol{\xi}$$
$$W_2 = \frac{1}{2}\int_H \omega_{mb}(\boldsymbol{\eta},\boldsymbol{\xi})dA_\xi \tag{4.4}$$

$$\omega_{fb}(\boldsymbol{\eta},\boldsymbol{\xi}) = \frac{\bar{c}_{fb}(\|\boldsymbol{\xi}\|)s^2\boldsymbol{\xi}}{2}, \quad \omega_{mb}(\boldsymbol{\eta},\boldsymbol{\xi}) = \frac{\bar{c}_{mb}(\|\boldsymbol{\xi}\|)s^2\boldsymbol{\xi}}{2} \tag{4.5}$$

where *s* is the constant strain value of the homogeneous deformation (see also Eq. (2.8)). ω_{fb} and ω_{mb} are the micro-elastic potentials for the anisotropic peridynamic material along the longitudinal and transverse directions. $\bar{c}_{fb}$ and $\bar{c}_{mb}$ are the elastic stiffness (micromodulus) functions for "fiber bonds" and "matrix bonds", respectively. D(||ξ||, 0)

and $D(\|\boldsymbol{\xi}\|, \pi)$ are the two-dimensional Dirac delta functions (distributions) for the polar coordinates $\theta=0$ and $\theta=\pi$ ($\theta=\arctan(\xi_2/\xi_1)$, $\boldsymbol{\xi}=(\xi_2, \xi_1)=(\xi, \theta)$).

We impose the peridynamic elastic strain energy densities above to equal the longitudinal and transverse components, respectively, of the strain energy density under 2D plane stress conditions, of a classical elasticity composite material under the same homogenous deformation. The classical strain energy density for the homogenized composite lamina is given by:

$$W_1^{\text{classical}} = \frac{1}{2}\frac{(E_{11} + \nu_{12}E_{22})}{(1-\nu_{12}\nu_{21})}s^2, \quad W_2^{\text{classical}} = \frac{1}{2}\frac{(E_{22} + \nu_{12}E_{22})}{(1-\nu_{12}\nu_{21})}s^2 \tag{4.6}$$

We use here the “conical” micromodulus function (see [15]) because this function gives a slightly smaller error against the classical solution, in the limit of the horizon going to zero, compare with constant micromodulus function ([48], [15]). By matching the corresponding elastic strain energies, for the peridynamic “fiber bonds” we get:

$$\bar{c}_{\text{fb}} = \frac{6(E_{11} + \nu_{12}E_{22})}{(1-\nu_{12}\nu_{21})\delta^2}\left(1 - \frac{\|\boldsymbol{\xi}\|}{\delta}\right) \tag{4.7}$$

while for bonds along the transverse direction (“matrix bonds”) we obtain:

$$\bar{c}_{\text{mb}} = \frac{12(E_{22} + \nu_{12}E_{22})}{(1-\nu_{12}\nu_{21})\pi\delta^3}\left(1 - \frac{\|\boldsymbol{\xi}\|}{\delta}\right) \tag{4.8}$$

The micromodulus function for the homogenized anisotropic peridynamic material therefore is (see Figure 4.2):

$$C(\|\boldsymbol{\xi}\|,\theta)=\begin{cases}\bar{c}_{fb}(\|\boldsymbol{\xi}\|) & \text{if } \theta=0 \text{ or } \pi \\ \bar{c}_{mb}(\|\boldsymbol{\xi}\|) & \text{otherwise}\end{cases} \tag{4.9}$$

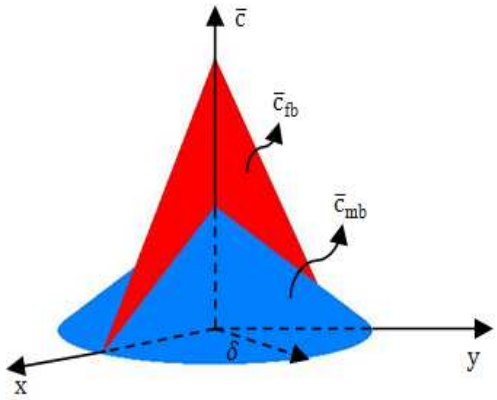

Figure 4.2. The conical micromodulus function for the homogenized peridynamic model of a unidirectional fiber-reinforced composite.

The pairwise force function f for our model can be written as follows

$$\mathbf{f}(\boldsymbol{\eta},\boldsymbol{\xi})=\begin{cases}\mathbf{f}_{fb}(\boldsymbol{\eta},\boldsymbol{\xi})[D(\|\boldsymbol{\xi}\|,0)+D(\|\boldsymbol{\xi}\|,\pi)] & \text{if } \theta=0 \text{ or } \pi \\ \mathbf{f}_{mb}(\boldsymbol{\eta},\boldsymbol{\xi}) & \text{otherwise}\end{cases} \tag{4.10}$$

where $\mathbf{f}_{fb}(\boldsymbol{\eta}, \boldsymbol{\xi})$ and $\mathbf{f}_{mb}(\boldsymbol{\eta}, \boldsymbol{\xi})$ are the pairwise force functions for "fiber bonds" and "matrix bonds", respectively.

Notice that if we were to consider an isotropic peridynamic material that would match W_1, the micromodulus for such a material would have been:

$$c_{11}^{iso} = \frac{12(E_{11} + \nu_{12}E_{22})}{(1-\nu_{12}\nu_{21})\pi\delta^3}\left(1 - \frac{\|\boldsymbol{\xi}\|}{\delta}\right) \tag{4.11}$$

Similarly for the transverse direction, to match W_2, we would get

$$c_{22}^{iso} = \frac{12(E_{22} + \nu_{12}E_{22})}{(1-\nu_{12}\nu_{21})\pi\delta^3}\left(1 - \frac{\|\boldsymbol{\xi}\|}{\delta}\right) \tag{4.12}$$

Observe that the ratio between $\bar{c}_{fb}$ and c_{11}^{iso} is $\pi\delta/2$. Notice also that c_{22}^{iso} is the same as $\bar{c}_{mb}$.

Remark: c_{11}^{iso} and c_{22}^{iso} have great advantage in discrete model in order to keep the scaling factor dimensionless. We will discuss in detail in following section. Moreover, the shear modulus does not enter specifically in the formulation. Its value will be dependent on the elastic moduli and the Poisson ratios. We mention that in the state-based peridynamics ([68]) the Poisson ratios and the shear modulus values can be independently modeled.

For the homogenized peridynamic model of UD FRCs, we postulate that damage occurs in the "fiber bonds" and "matrix bonds" when they are stretched beyond some corresponding critical relative elongations, s_0^{fb} and s_0^{mb}. The critical relative elongation s_0^{fb} is obtained by matching the work needed to break all bonds in a material made entirely out of "fiber bonds" (not fibers), across a line (for the 2D case) to the fracture energy G_0^{11}. The value for s_0^{mb} can be obtained in a similar way by matching G_0^{22} with the work needed to break all bonds in a material made entirely out of "matrix bonds" (not matrix material), across a line (in 2D). The values we obtain are:

$$s_0^{fb} = \sqrt{\frac{20\pi G_0^{11}}{\bar{c}_{fb}\delta^3}}, \quad s_0^{mb} = \sqrt{\frac{20G_0^{22}}{\bar{c}_{mb}\delta^4}} \tag{4.13}$$

where G_0^{11} and G_0^{22} are the fracture energies for a UD composite with 0° fiber orientation and 90° fiber orientation lamina, respectively. Recall that the "fiber bond" properties are not matched to the fiber material, but to the effective properties along the fiber direction. The same goes for "matrix bonds".

The fracture energy G_0^{11} and G_0^{22} are experimentally measured from the intralaminar mode I fracture test [69]. We emphasize that in this damage model, the critical relative elongation only depends on the material properties and also depend on the horizon size. Note that dependencies of the critical relative elongation on the current elastic deformation state, manufacturing defects, and time [49], or current damage state [15] can be easily introduced into the model if desired.

4.4 The discrete model and the scaling of the micromodulus function

In our model, the peridynamic "fiber bonds" emanating from a particular node are only those bonds that have the same or nearly the same direction as the longitudinal direction. All other bonds connected to this node are "matrix bonds" (see Figure 4.2). Note that the discretization below is employed to regular square grids aligned with the fiber direction (such as 0º or 90º), and for grids not aligned with the fiber direction (arbitrary angle

between grids and fiber direction other than 0º or 90º) (see Figure 4.3). The preference for uniform grids is due to the simplicity of generating them and conducting convergence tests, as well as the convenience for modeling the 0º, 45º, and 90º fiber orientations, the most used in practice. Uniform grids aligned with the fiber direction are used in all the computations in this paper.

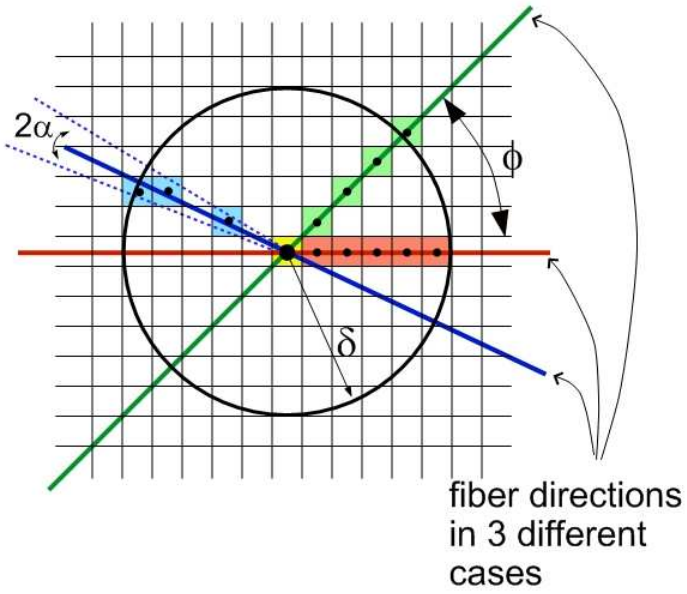

Figure 4.3. The discrete peridynamic model for three different unidirectional FRCs at a node for a uniform grid. Possible orientations between the grid and the fibers are shown (red, green and blue represent φ = 0°, 45°, and some arbitrary value). The nodes with fiber bond connections to the central node are marked in each case.

In the discrete model, the strain energy density will change due to the grid refinement and/or grid not aligned with the fiber direction. Thus, the scaling approach is necessary in order to keep the strain energy density as a constant. In what follows, we use a semi-analytical approach to estimate the scaling required for the case in which the

fibers make 0°, 45°, and 90° angle with the uniform discretization grid. For the general grid orientation relative to a uniform grid and/or a non-uniform discretization such an approach is not possible and, instead, we introduce a new algorithm that correctly scales the model.

4.4.1 Semi-analytical derivation of the discrete model and the scaling factors for φ =0° or 90°

As a result of grid refinement for a fixed horizon size (the so-called *m*-convergence see Figure 2.6), the “fiber bonds” area in the peridynamic discretization at a node changes. This is schematically shown in Figure 4.4, and the change is reflected in a change in the strain energy density, at the node, unless proper scaling is employed.

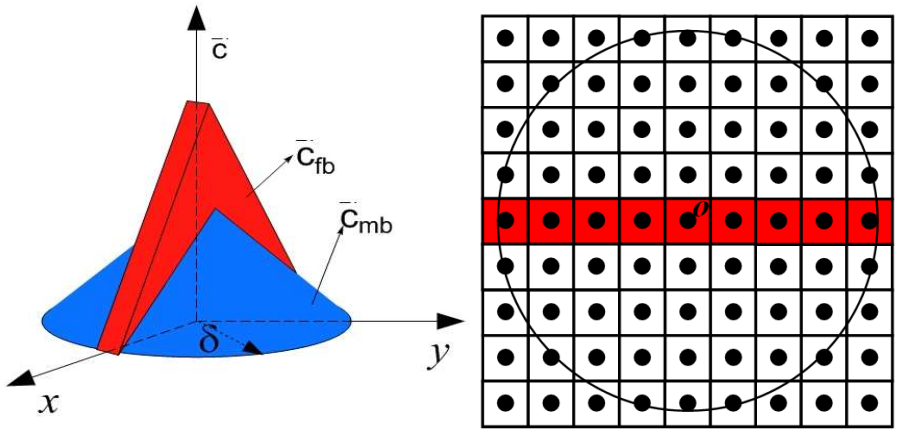

Figure 4.4. Conical micromodulus function for the UD composite lamina at a point in the bulk (a). The discrete peridynamic model for unidirectional lamina at a particular node O (b). The circle is the horizon for this node. Fiber direction is horizontal in this example, thus the peridynamic "fiber bonds" for the central node exist only with nodes having their areas colored in red (since only these bonds, centered at O, have the same direction as the fiber direction).

Let W_1^d the elastic strain energy density computed over the "fiber bonds" area in the discretized configuration in Figure 4.4, based on the c_{11}^{iso} in Eq. (4.11). Obviously, this will not match W_1 since we do not integrate over the entire horizon area. Similarly, let W_2 be elastic strain energy density computed over the "matrix bond" area in the discretized configuration in Figure 4.4, based on the c_{22}^{iso} in Eq. (4.12). We find the scaling factors λ_{fb} and $\lambda_{mb}\lambda_{mb}$, for the "fiber bonds" and "matrix bonds" in the discretized model, respectively, so that:

$$\lambda_{fb} W_1^d = W_1, \quad \lambda_{mb} W_2^d = W_2 \tag{4.14}$$

From Eqs. (4.4), (4.11), and (4.12), the scaling factors for “fiber bonds” and “matrix bonds” are found as:

$$\lambda_{fb} = \frac{W_1}{W_1^d} = \frac{\frac{1}{2}\int_{A_\delta} \frac{c_{11}^{iso}(\|\xi\|)s^2\|\xi\|}{2} dA_\xi}{\frac{1}{2}\int_{A_{fb}^d} \frac{c_{11}^{iso}(\|\xi\|)s^2\|\xi\|}{2} dA_\xi} \tag{4.15}$$

$$\lambda_{mb} = \frac{W_2}{W_2^d} = \frac{\frac{1}{2}\int_{A_\delta} \frac{c_{22}^{iso}(\|\xi\|)s^2\|\xi\|}{2} dA_\xi}{\frac{1}{2}\int_{A_{fb}^d} \frac{c_{22}^{iso}(\|\xi\|)s^2\|\xi\|}{2} dA_\xi} \tag{4.16}$$

where A_δ is the total area covered by the horizon of radius δ (see the circle area in Figure 4.4). A_{fb}^d and A_{mb}^d are the “fiber bonds” area (see Figure 4.4, the red area inside the circle.) and “matrix bonds” area (the white areas inside the circle) for the particular discretization, respectively.

The discrete version for the conical micromodulus function case is then written as

$$C^d(\|\xi\|,\theta) = \begin{cases} \lambda_{fb} c_{11}^{iso}(\|\xi\|) & \text{if } \theta = 0 \text{ or } \pi \\ \lambda_{mb} c_{22}^{iso}(\|\xi\|) & \text{otherwise} \end{cases} \tag{4.17}$$

We can also express this micromodulus function in terms of the continuum peridynamic anisotropic model in Eq. (4.9).

$$C^d(\|\boldsymbol{\xi}\|,\theta)=\begin{cases}\bar{\lambda}_{fb}\bar{c}_{fb}(\|\boldsymbol{\xi}\|) & \text{if } \theta=0 \text{ or } \pi\\ \bar{\lambda}_{mb}\bar{c}_{mb}(\|\boldsymbol{\xi}\|) & \text{otherwise}\end{cases} \tag{4.18}$$

where $\bar{\lambda}_{fb}=2\lambda_{fb}/\pi\delta$ and $\bar{\lambda}_{mb}=\lambda_{mb}$. Moreover, the scaling factor λ_{fb} is independent of the horizon size. Because of this, in practice we will use the scaling of the discrete micromodulus function in the form of Eq. (4.17).

Remark: in practice, for the conical micromodulus function, instead of the values for λ_{fb} and λ_{mb} obtained above, we use the following approximations:

$$\tilde{\lambda}_{fb}=\frac{A_\delta}{A^d_{fb}}\cong\frac{\pi m}{2},\quad \tilde{\lambda}_{mb}=\frac{A_\delta}{A^d_{mb}}\cong\frac{\pi m}{\pi m-2} \tag{4.19}$$

where $m=\delta/\Delta x$, with Δx being the grid spacing in a uniform discretization. These ratios of areas are good approximations for the ratios of strain energies above because of the nature of the integrand functions in Eqs. (4.15) and (4.16): these functions are zero at the node and at the boundary of the horizon. These approximations are less than 1% in error for values of m=5 or larger. For any micromodulus function other than the conical one, the scaling parameters can be computed from Eqs. (4.15) and (4.16) using numerical integration, for example.

Table 4.1. Comparison between the approximate and analytical values for the scaling factor for the conical micromodulus function.

	λ_{fb}	$\tilde{\lambda}_{fb}$	Error *	λ_{mb}	$\tilde{\lambda}_{mb}$	Error**
m=4	6.1974	6.2832	1.38%	1.1924	1.1893	0.26%
m=5	7.7764	7.8540	1%	1.1475	1.1459	0.14%

* Relative error between approximate and analytical scaling factor for “fiber bonds”
** Relative error between approximate and analytical scaling factor for “matrix bonds”

4.4.2 The scaling factors for φ=45°

In order to have a discrete model that is independent not only on the discretization size but also on the orientation of the discrete grid relative to the fibers we need additional scaling factors. In this section, we provide a semi-analytical derivation for the scaling factors in the discrete peridynamic model for the case when the angle between the uniform grid and the fibers is 45°. In this case (uniform grid and φ= 45°), the geometry allows to easily derive the scaling parameters (see nodes with green areas in Figure 4.3). The nodes on the diagonal direction (45°) of the grid cells have "fiber-bonds" connections with the center node. The goal is to obtain the same strain energy density (under a homogeneous and equal deformation imposed along the longitudinal and transverse directions) for φ=45°.

Let $W^{d}_{fb\_0}$ and $W^{d}_{fb\_45}$ be the discrete elastic strain energy densities from the "fiber bonds" for φ = 0° (red line in Figure 4.3) and φ = 45° (green line in Figure 4.3) for the given longitudinal and transverse deformations with a constant relative elongation *s*, respectively:

$$W^{d}_{fb\_0} = \frac{1}{2}\int_{A^{d}_{fb\_0}} \frac{c^{iso}_{11}(\|\boldsymbol{\xi}\|)s^2\boldsymbol{\xi}}{2} dA_{\boldsymbol{\xi}}, \quad W^{d}_{fb\_45} = \frac{1}{2}\int_{A^{d}_{fb\_45}} \frac{c^{iso}_{11}(\|\boldsymbol{\xi}\|)s^2\boldsymbol{\xi}}{2} dA_{\boldsymbol{\xi}} \tag{4.20}$$

where $A^{d}_{fb\_0}$ and $A^{d}_{fb\_45}$ are the "fiber bonds" areas (red and green areas in Fig. 4) for φ= 0° and φ= 45°, respectively. Obviously, $W^{d}_{fb\_0}$ and $W^{d}_{fb\_45}$ will not match each other since the areas of integration are different. We introduce the scaling factor γ_{fb} for the "fiber bonds" defined by

$$\gamma_{\text{fb}} = \frac{W^{\text{d}}_{\text{fb\_0}}}{W^{\text{d}}_{\text{fb\_45}}} = \frac{\frac{1}{2}\int_{A^{\text{d}}_{\text{fb\_0}}} \frac{c^{\text{iso}}_{11}(\|\boldsymbol{\xi}\|)s^2\boldsymbol{\xi}}{2} dA_{\boldsymbol{\xi}}}{\frac{1}{2}\int_{A^{\text{d}}_{\text{fb\_45}}} \frac{c^{\text{iso}}_{11}(\|\boldsymbol{\xi}\|)s^2\boldsymbol{\xi}}{2} dA_{\boldsymbol{\xi}}} \tag{4.21}$$

Using mid-point numerical integration scheme for the conical micromodulus function (see Eqs. (4.11)), the scaling factor γ_{fb}, for a given discretization, becomes:

$$\gamma_{\text{fb}} = \frac{W^{\text{d}}_{\text{fb\_0}}}{W^{\text{d}}_{\text{fb\_45}}} \cong \frac{\sum_{i=1}^{p}(\xi_i - \frac{\xi_i^2}{\delta})A_i}{\sum_{j=1}^{q}(\xi_j - \frac{\xi_j^2}{\delta})A_j} \tag{4.22}$$

where A_i is the nodal area; here, for simplicity, we assume that all the nodes inside the horizon have their full volume contained in the horizon; also, the distances from the center node to the *i*-th and *j*-th nodes on the 0°and 45° directions are:

$$\xi_i = i\Delta x, \quad \xi_j = j\sqrt{2}\Delta x \tag{4.23}$$

where Δx is the grid spacing and *p* and *q* are the number of nodes along φ= 0°and φ= 45° directions inside the horizon δ:

$$p = \left[\frac{\delta}{\Delta x}\right], \quad q = \left[\frac{\delta}{\sqrt{2}\Delta x}\right] \tag{4.24}$$

The notation [δ/Δx] defines the integer part of δ/Δx. From Eqs. (4.22)-(4.24), we obtain:

$$\gamma_{fb} \cong \frac{\frac{1}{p^2}\sum_{i=1}^{p}(p\times i\text{-}i^2)}{\frac{1}{q^2}\sum_{j=1}^{q}(q\times j\text{-}j^2)} = \frac{p+2-\frac{2}{p}-\frac{1}{p^2}}{q+2-\frac{2}{q}-\frac{1}{q^2}} \tag{4.25}$$

If p and q are sufficiently large and the horizon δ is constant, the scaling factor γ_{fb} is well approximated by:

$$\gamma_{fb} \cong \sqrt{2} = \frac{1}{\cos 45^{\circ}} \tag{4.26}$$

Similarly, let $W^{d}_{mb\_0}$ and $W^{d}_{mb\_45}$ be the discrete elastic strain energy densities from the "matrix bonds" for φ = 0°and φ = 45°, for the given longitudinal and transverse deformations with a constant relative elongation s, respectively. We find the scaling factor γ_{mb} , for "matrix bonds" as:

$$\gamma_{mb} = \frac{W^{d}_{mb\_0}}{W^{d}_{mb\_45}} = \frac{\frac{1}{2}\int_{A^{d}_{mb\_0}} \frac{c^{iso}_{22}(\|\xi\|)s^2\xi}{2}\,dA_{\xi}}{\frac{1}{2}\int_{A^{d}_{mb\_45}} \frac{c^{iso}_{22}(\|\xi\|)s^2\xi}{2}\,dA_{\xi}} \tag{4.27}$$

where $A^{d}_{mb\_0}$ and $A^{d}_{mb\_45}$ are the "matrix bonds" areas (the entire horizon area minus the "fiber bonds" area) for φ = 0° and φ = 45°, respectively.

Following the same procedure as before, the scaling factor γ_{mb} for "matrix bonds" is

$$\gamma_{mb} \cong \left(\frac{\pi\delta - \Delta x}{\pi\delta - \frac{\Delta x}{\sqrt{2}}} \right) \tag{4.28}$$

The new discrete version of the conical micromodulus functions for $\varphi = 45°$ is therefore

$$C_{45}^{d}(\|\xi\|, \theta) = \begin{cases} \gamma_{fb} \times \lambda_{fb} c_{11}^{iso}(\|\xi\|) & \text{if } \theta = 0 \text{ or } \pi \\ \gamma_{mb} \times \lambda_{mb} c_{22}^{iso}(\|\xi\|) & \text{otherwise} \end{cases} \tag{4.29}$$

4.4.3 An algorithm for computing scaling factors in the discrete peridynamic model for arbitrary grids

For an arbitrary orientation of the grid relative to the fibers and/or when a non-uniform discretization is used, there might not be any nodes exactly sitting along the fiber direction that passes through the center node (see Figure 4.3). To define "fiber bonds" in these cases we search in a "cone" of angle 2α about the fiber direction, where α is a given tolerance. If angle φ' between a peridynamic bond direction belonging to the center node and the horizontal direction falls in the interval $[\varphi - \alpha, \varphi + \alpha]$, then that bond is considered a "fiber bond" (see, for example, the blue nodes in Figure 4.3). All other bonds are considered to be "matrix bonds". Explicit formulations for scaling factors γ_{fb} and γ_{mb} in these cases are not easy to obtain because of the dependence on: the fiber orientation relative to the grid, the selected angle tolerance, the grid spacing and the horizon size, and more importantly, on the specific discretization used in the case of a non-uniform or random-nodes discretization. We obtain therefore appropriate scaling

factors for “fiber bonds” and “matrix bonds” numerically. We compute the strain energy density for “fiber bonds” and “matrix bonds” for a specific fiber orientation φ and under given homogeneous longitudinal and transverse deformations, and match them to the longitudinal and transverse components of the classical strain energy density (W_1 and W_2) by the following procedure, given in Table 4.2.

Table 4.2. Numerical evaluation of the scaling factors for arbitrary uniform grid orientation relative to the fibers and/or an arbitrary discretization.

1: Input fiber orientation φ (relative to the horizontal axis) and angle tolerance α

2: Impose deformation along longitudinal and transverse direction

3: Compute longitudinal and transverse classical strain energy densities W_1 and W_2

4: Compute the angle φ' between a peridynamic bond direction and horizontal direction

5: If $\varphi - \alpha \le \varphi' \le \varphi + \alpha$ then

6: the bond is assigned as “fiber bond”

7: Else

8: the bond is assigned as “matrix bond”

9: Endif

10: Compute the peridynamic discrete strain energy densities for “fiber bonds” $W^{d}_{fb\_\varphi}$ and “matrix bonds” $W^{d}_{mb\_\varphi}$

11: Compute the scaling factors for “fiber bonds” and “matrix bonds”

$$\gamma^{\varphi}_{fb} = \frac{W_1}{W^{d}_{fb\_\varphi}}, \quad \gamma^{\varphi}_{mb} = \frac{W_1}{W^{d}_{mb\_\varphi}}$$

The tolerance angle α may be chosen in terms of *m*, the ratio between the horizon and the grid spacing. For example, if *m* is large, the angle tolerance α can be small. In

fact, in the limit of *m* going to infinity, the value of α could be taken as the actual fiber misalignment in the manufactured UD FRCs. For instance, in a carbon fiber composite material like the APC-2 [70], most of the fibers are found to lie within ±3° of the fiber direction.

The scaling factors obtained from Table 4.2 are then used to scale the micro-modulus (conical) function as follows:

$$C_{\varphi}^{d}(\|\boldsymbol{\xi}\|,\theta)=\begin{cases}\gamma_{fb}^{\varphi}c_{11}^{iso}(\|\boldsymbol{\xi}\|) & \text{if } \theta=\varphi\\ \gamma_{mb}^{\varphi}c_{22}^{iso}(\|\boldsymbol{\xi}\|) & \text{otherwise}\end{cases} \tag{4.30}$$

This micromodulus function is then used in the peridynamic computations that use a uniform grid with an arbitrary orientation to the fibers, or that use an arbitrary discretization. Notice that, in most cases, uniform grids are preferred to non-uniform grids, because they are easier to generate and the algorithms become simpler. However, in the case of adaptive refinement (see [50] for the case of isotropic materials) regions with irregular grids will naturally occur and therefore the above algorithm should be used in problems where adaptive refinement is employed for modeling the behavior of UD FRCs.

4.5 Numerical simulation

In this section, convergence studies under uniform grid refinement for a fixed horizon size (*m*-convergence) and under decreasing the peridynamic horizon (δδ-convergence)

are performed in terms of the crack path and crack propagation velocity. We treat a number of examples of dynamic fracture in UD FRC and analyze, in particular, the influence of the stress waves (generated by the suddenly applied loads or reflected from the boundaries) on the crack propagation and damage patterns. We use two different loading cases and vary the loading amplitude to perform simulations, and then compare the peridynamic results with experiments.

4.5.1 Problems setup

We consider the following setup for analyzing dynamic fracture phenomena in a UD composite lamina: a central-crack thin rectangular plate with 0.2m x 0.1m as shown in Figure 4.5. Two different loading types are employed in our simulations: in the first case A (Figure 4.6a) a uniform tensile load is applied suddenly *along the left and right edges* and maintained constant in time after that; in the second case B (Figure 4.6b), a uniform tensile load *is applied suddenly on the crack surfaces* and maintained constant in time after that. Both cases generate sharp stress wave (shock waves) but of different profiles and which interact differently with the boundaries and the crack surfaces. Dynamic experiments in UD FRC that produce the type of loading similar to case A (loading on the external boundaries of the sample), have been reported in [7]. Creating rapid loading on the crack faces is reported in the experiments in [9]. The composite material used in the examples shown below is the M55J/M18 carbon/epoxy [69]. The material properties are presented in Table 4.3.

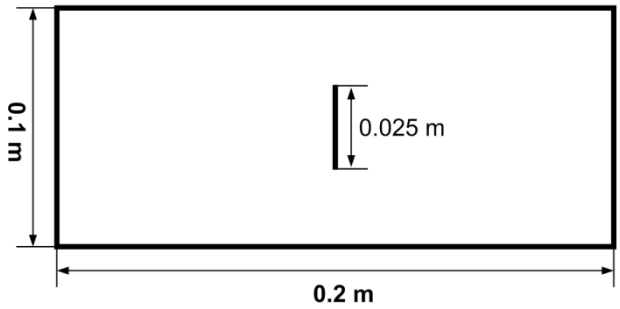

Figure 4.5. Geometry of the plate with a center notch for the dynamic tests on unidirectional fiber-reinforced composites.

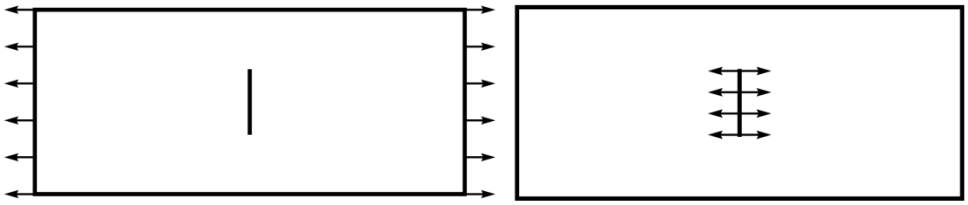

A B

Figure 4.6. Two different loading cases: Case A. suddenly applied loading on the left and right boundaries; Case B. sudden loading on the pre-crack surfaces.

Table 4.3. Material Properties.

Property	**Unidirectional**
Longitudinal Young's modulus E_{11}(GPa)	329
Transverse Young's modulus E_{22}(GPa)	6
Shear modulus G_{12}(GPa)	4.4
Poisson's ratio υ_{12}	0.346
Density ρ(kg/ m^3)	1630
Fracture energy G_0^{11}(KJ/m^2)	15.49
Fracture energy G_0^{22}(KJ/m^2)	0.168

Notice that in the present bond-based peridynamic model, the only inputs in the model are the values of the Young's moduli and values for mode I fracture energies for 0° and 90° fiber orientations. The values of the Poisson ratio, shear modulus, and mode II fracture energy are determined, in this bond-based peridynamic model, by the Young's moduli and mode I fracture energies. These limitations are removed if one uses the state-based peridynamics [68]. With the state-based peridynamic composite model one can model a composite material with arbitrary material properties. We use here the somewhat simpler bond-based version because our focus is on demonstrating the capabilities of the peridynamic approach in modeling dynamic fracture in a fiber-reinforced composite.

4.5.2 Benchmark test

In this section we compare the total elastic strain energy of the scaled model and the non-scaled model with the exact classical elasticity solution. The elastic strain energy of a composite lamina with 0° fiber orientation without a per-crack is examined for the homogeneous deformation (constant bi-axial strain $\alpha = 0.005$) given below:

$$\mathbf{F} = \alpha \mathbf{I} \tag{4.31}$$

where **F** and **I** are deformation gradient tensor and identity tensor, respectively, and α is a constant positive value. The total strain energy for the rectangular plate (without the center cut) as shown in Figure 4.5 is the integral over the plate area of the nodal strain energy density. Since we are employing an approximate scheme for the spatial

integration (see the algorithm for partial area evaluation in [50]), we will only obtain approximations of the exact classical strain energy density. Moreover, because of the "skin effect" near the boundaries (see, e.g. [31]) additional error will be introduced. Nevertheless, as *m* increases the approximate numerical integration approaches the exact integration, while decreasing the horizon δ the skin effect is reduced as well. The results, for both the scaled (see Eq. (4.17)) and non-scaled (directly use Eqs. (4.11) and (4.12)) models are given in Table 4.4. The exact classical strain energy with the same homogeneous deformation and configuration, which can be obtained from Eq. (4.6), is 84.92 KJ.

Table 4.4. Comparison of strain energy between scaled and non-scaled model with conical micromodulus function

	δ = 4 mm		δ = 2 mm		δ = 1 mm	
Model	SE-S* (KJ)	SE-NS** (KJ)	SE-S (KJ)	SE-NS (KJ)	SE-S (KJ)	SE-NS (KJ)
m = 3	72.93	16.86	73.37	16.97	73.63	17.05
m = 6	80.79	10.16	81.33	10.24	81.60	10.28
m = 12	83.07	6.16	83.57	6.21	83.82	6.23

* SE-S: Strain energy with the "scaled model"
** SE-NS: Strain energy with the "non-scaled model"

4.5.3 m-Convergence studies for φ = 0° subject to abrupt load

We perform *m*-convergence for two different horizon sizes: δ = 4mm and δ = 2mm with loading case A. For this loading case, a "no-fail zone" is used on the boundary nodes where the loads are suddenly applied, in order to prevent rupture at those locations. All the models use uniform grid spacing. The peridynamic models for horizon δ = 4 mm use

m = 3 or Δx = 1.33 mm (11552 nodes), m = 6 or Δx = 0.67 mm (45602 nodes), and m = 12 or Δx = 0.33 mm (181202 nodes). The results in terms of the damage maps are shown in Figure 4.7. We observe that the crack paths (seen as zones with non-zero damage) are similar for the different grids used and that the splitting fracture mode is captured for this lamina with 0° fibers. We also mention that the damage takes place only in the "matrix bonds", no "fiber bonds" break under the applied shock loading σ = 40MPa. In all the damage maps below we use the same range for the color-bar of the damage index as in Figure 4.7.

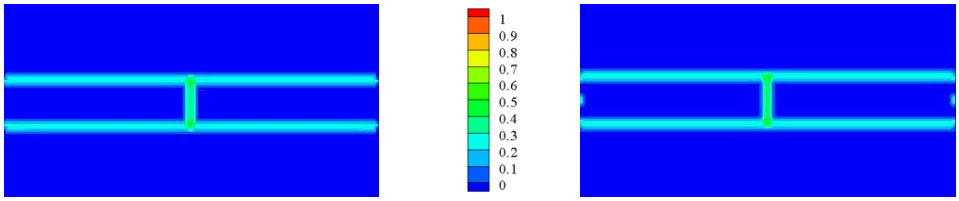

(a) (b)

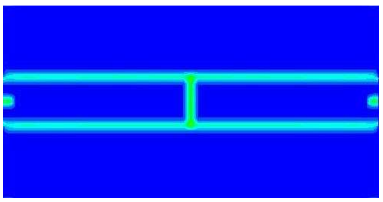

(c)

Figure 4.7. Damage index maps (or crack path) computed with different grids for δ = 4 mm at 50µs. (a) m = 3; (b) m = 6; (c) m = 12. The same damage index scale is used in all plots.

To monitor the fracture behavior, we define the damage index of a node as the number of broken bonds by the original number of bonds for that node. The expression for the damage index is therefore:

$$d = \frac{n_{broken}}{n} \tag{4.32}$$

where n_{broken} and n nare the number of broken bonds and the number of initial bonds at a node. The damage index is a number between 0 and 1 (0 means no bonds are broken, and 1 means all the bonds are broken). Note that a damage index of around 0.4-0.5 may indicate that a fracture surface exists.

For horizon δ = 2 mm, the grids used are for *m*=3 or Δx = 0.67 mm (45602 nodes), *m*=4 or Δx = 0.5 mm (80802 nodes), and m=8 or Δx = 0.25 mm (321602 nodes). The results are given in Figure 4.8. The difference between the case with *m*=4 and *m*=8 is minimal. The splitting fracture mode is again captured well in this UD composite lamina with 0° 0°fibers. Also, no fiber failure occurs in these simulations. In Figure 4.8(a), we use *m* = 3 instead of *m* = 2 because the number of nodes inside horizon, for *m*=2, is not sufficient to allow a sufficiently large number of directions in which a crack can grow as a results of bond breaking.

As shown in Figure 4.8, the results indicate that using *m* = 5 is a good choice since the crack path does not suffer significant changes if one uses an even denser grid, and this choice is computationally efficient too. For all the remaining studies below we use *m* = 5.

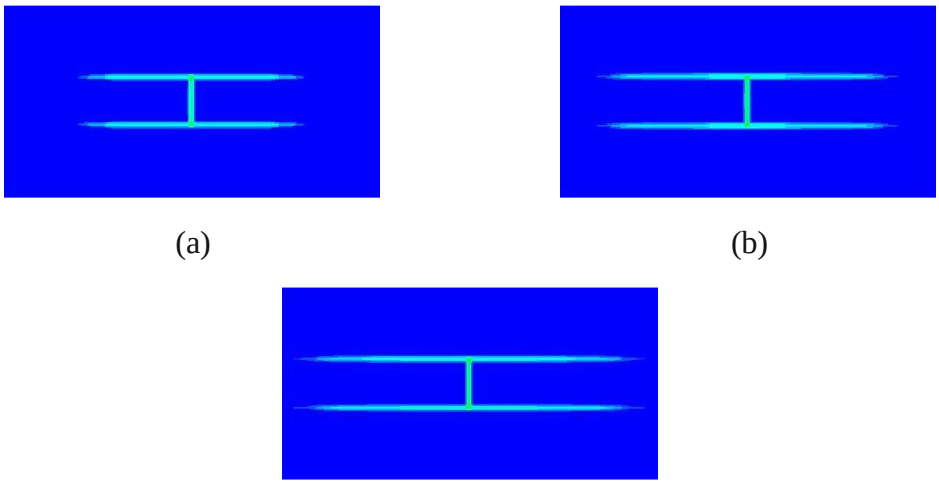

(a) (b)

(c)

Figure 4.8. Damage index maps (indicating the crack paths) computed with different grids for δ = 2 mm at 50μs. (a) m = 3; (b) m = 4; (c) m = 8.

4.5.3 δ-Convergence studies for φ = 0° subject to abrupt load

For a fixed value m = 5, we use four different kinds of horizon sizes (uniform grid spacing): δ = 4 mm or Δx = 0.8 mm (31752 nodes), δ = 3 mm or Δx = 0.6 mm (56112 nodes), δ = 2 mm or Δx = 0.4 mm (126002 nodes), and δ = 1 mm or Δx = 0.2 mm (502002 nodes). We note that for m = 5 and δ = 1 mm the elastic strain energy computed with peridynamics is only about 4% different from the classical exact value. Please note that the critical relative elongation also changes with respect to the changing horizon, as seen from Eq. (4.13).

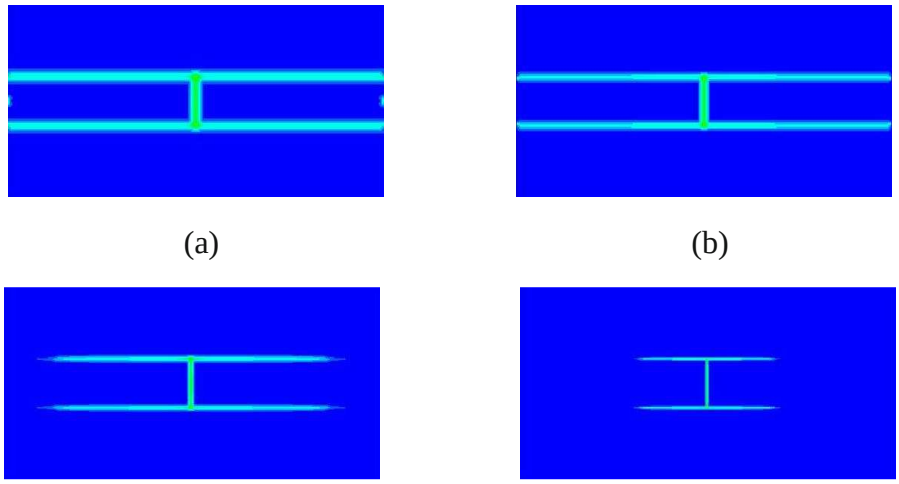

(a) (b)

(c) (d)

Figure 4.9. Damage index maps computed with various δ (*m* = 5) at 50μs. (a) δ = 4mm; (b) δ = 3mm; (c) δ = 2mm; (d) δ = 1mm.

The results showing the damage map for each case are given in Figure 4.9. In all simulations the symmetric path of splitting fracture mode is obtained and only "matrix bonds" breakage is observed, no "fiber bonds" break (besides those corresponding to the initial center-cut). The damage patterns from these peridynamic simulations agree very well with the experimental observations in [71], who also report only matrix breaking taking place (under quasi-static loadings). Notice in Figure 4.9 that the crack length changes during the δ-convergence study because the crack speed changes as the horizon becomes smaller. It is noted that the largest horizon used (δ = 4) results in a strong nonlocal effect since the size of the center cut can be, in this case, covered by only about three horizon regions. The "large" nonlocality induces a much higher crack propagation speed than realistically expected. The crack propagation speed from our δ–convergence

results and comparisons with analytical solutions for the classical steady-state dynamic debonding crack propagation are discussed in the next section.

4.5.4 Study of the splitting crack propagation speed

In this section we study the crack propagation speed in terms of the horizon size for the splitting fracture mode. As shown in Figure 4.10, the crack starts propagating at about 22μs after the loads have been applied at the boundaries (see Figure 4.6a). The larger horizon size simulation shows that the crack already reaches the boundaries at around 44μs. As the horizon size decreases, the average and the maximum crack propagation speeds decrease as well. The stress waves strongly affect the crack propagation speed. The observed speed-up and slow-down of the crack propagation speed seen in Figure 4.10 correlates well with the propagation of the stress/strain waves in the material, as seen from Figure 4.11. In Figure 4.11, we show the strain energy density at different times for the case with the smallest horizon used in this paper. It is apparent that when the stress waves are moving away from the crack tip, the crack propagation speed increases, and when the reflected waves return and meet the crack tip, the crack propagation speed decreases. Because of the dynamic loading and interaction with the stress waves, the crack arrests temporarily, before it continues to propagate again.

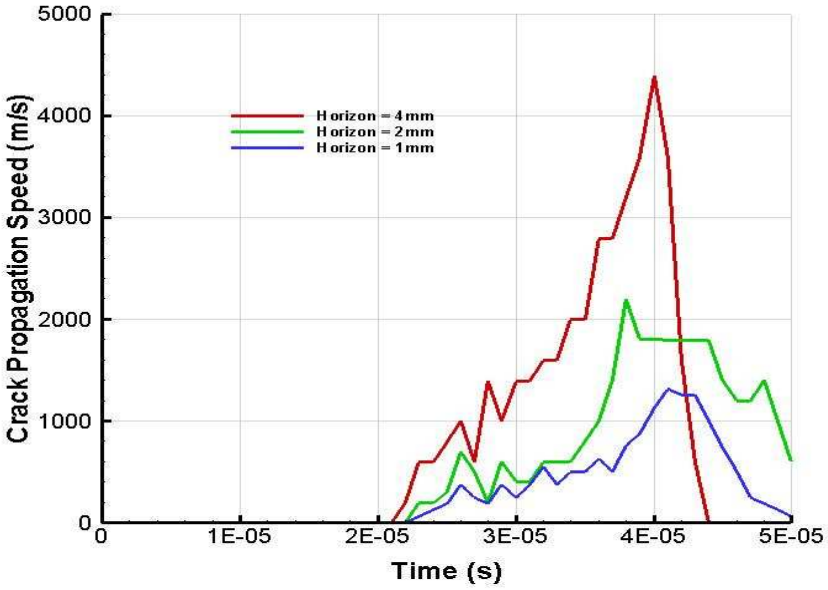

Figure 4.10. Crack propagation speed for different horizons.

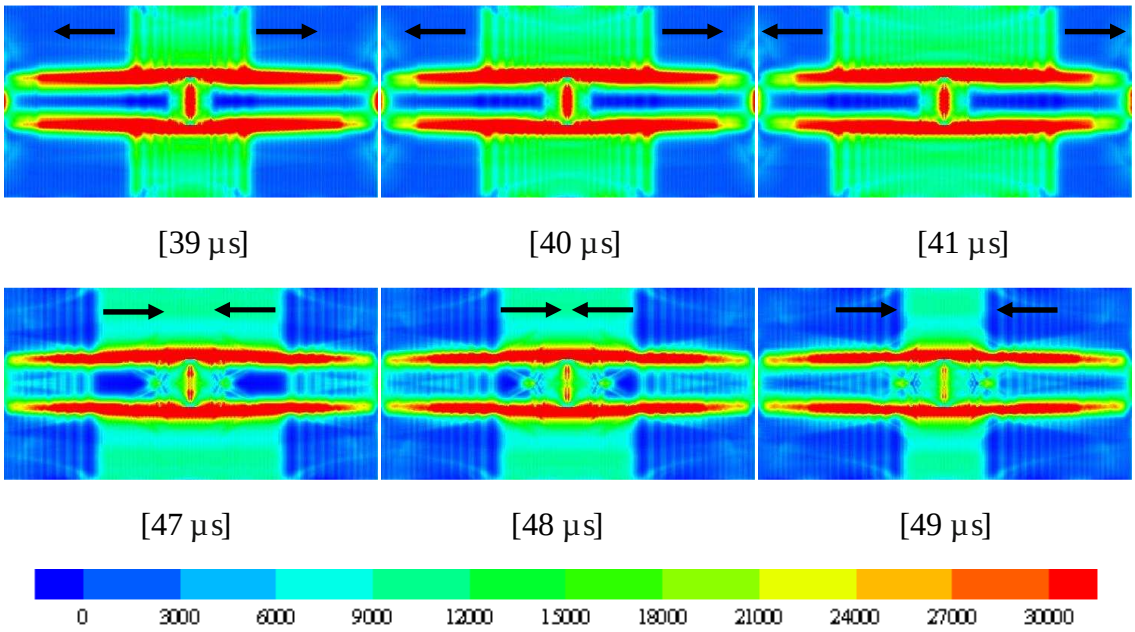

Figure 4.11. Strain energy density (δ = 1mm and m = 5) at different times (black arrows indicate the "direction of motion" of the stress waves). The crack path has not yet reached the state shown in Figure 4.9(d), which was obtained at 50µs.

We now focus on analyzing the maximum splitting crack propagation speed. A theoretical framework has been established in [72] for interface fracture mechanics that includes dynamic crack propagation and strain rate dependent material response. They argue that for cracks running at non-uniform speed, the near tip singularity is two dimensional, and is instantaneously in a steady state. A formula for the propagation speed of a debonding crack is given. Tsai et al. [73] used this formulation and found that the dynamic fracture toughness is roughly equal to the static fracture toughness and is not significantly influenced by crack speeds up to 1100 m/s. In particular, the modes I and II energy release rates remain nearly constant when the crack propagation speed is up to about 50% of the Rayleigh wave speed for S2/8553 glass/epoxy and AS4/3501-6 carbon/epoxy composites.

The crack propagation speed for a moving crack in a homogeneous orthotropic material can be obtained from the energy release rate and stress intensity factor ([72]; [73]). The crack propagation speed for splitting mode can be written as follows:

$$G_{II} = \frac{1}{2} H_{11} K_{II}^2 \tag{4.33}$$

where G_{II} and K_{II} are the fracture energy for mode II fracture and the mode II stress intensity factor, respectively. The expression of H_{11} is given as:

$$H_{11} = \frac{1}{C_{66} R} \rho_{22} a_2^2 \left[2(1+s)/\xi \right]^{1/2} \tag{4.34}$$

where

$$\rho_{11}=\frac{C_{11}}{C_{66}},\ \rho_{22}=\frac{C_{22}}{C_{66}},\ \rho_{12}=\frac{C_{12}}{C_{66}},\ \alpha_1=\sqrt{(1-\frac{\rho v_e^2}{C_{11}})},\ \alpha_2=\sqrt{(1-\frac{\rho v_e^2}{C_{66}})}$$

$$\xi=\alpha_1\alpha_2\sqrt{\rho_{11}/\rho_{22}},\ s=\frac{\alpha_2^2+\rho_{11}\rho_{22}\alpha_1^2-(1+\rho_{12})^2}{2\alpha_1\alpha_2\sqrt{\rho_{11}\rho_{22}}}$$

$$R=\rho_{22}(\rho_{22}\xi-1+\alpha_2^2)-\rho_{12}^2\alpha_2^2/\xi$$

where C_{11}, C_{22}, C_{66}, and C_{12} are the elastic constants defined in section 4.2. ρ and v_e are the density and the crack propagation speed for certain values of fracture energy and stress intensity factor, respectively.

With all the parameters provided as in [69], the crack propagation speed of the splitting mode for the value of G_{II} and K_{II}, from Eqs. (4.33) and (4.34), is about 820m/s. For M55J/M18 carbon/epoxy composite, the Rayleigh wave speed is about 1700m/s. In general, the fracture energy depends on the crack propagation speed. However, as pointed out in [73], the variation is minimal for cracks moving at speeds lower than 50% Rayleigh wave speed. Therefore it is reasonable to consider the fracture energy constant. In our peridynamic computations we use constant fracture energy in the formulas that give the critical relative elongation of the bonds. The values used in the peridynamic computations for mode I fracture energy in the 0° and 90° orientations are given in Table 4.3.

The relative error for the crack propagation speed computed with peridynamics for the different horizon sizes, against the analytical value mentioned above, is:

$$R_{error} = \frac{v\text{-}v_e}{v_e} \tag{4.35}$$

where v and v_e are the maximum crack propagation speed from the peridynamic computations and the analytical crack propagation speed computed above, respectively. In Figure 4.12(a), we give the relative error versus the horizon size and in Figure 4.12(b) the same plot in a log-log scale.

In the log-log plot the results indicate a linear relationship. With a linear curve-fit, we can obtain the crack speed for any horizon size as follows

$$v_\delta = v_e e^{\alpha} + v_e \tag{4.36}$$

where

$$\alpha = k * \log(\frac{1}{\delta}) - 0.49$$

where v_δ is the crack propagation speed for a given horizon size δ, k is the slope of the curve-fit line and equals -1.45 when the propagation speeds for the horizons equal to 4mm, 2mm, and 1mm were used. We compute the crack propagation speed for a value of the horizon equal to 3mm. The maximum crack propagation speed from peridynamics calculations with δ = 3mm is around 3,420m/s while the value obtained from the linear curve-fit above, for the same horizon size is 3,281m/s. The relative difference between these two results is less than 5%.

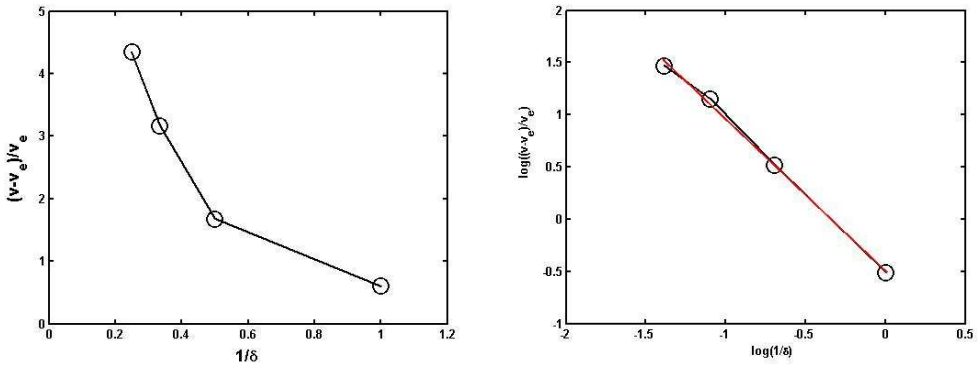

(a) (b)

Figure 4.12. Relative difference of the maximum crack propagation speed from the peridynamic computations for different horizon sizes versus the analytical value (a); linear curve fit in the log-log scale for the data on the left (b).

It appears that the maximum crack propagation speed computed by peridynamics, in the limit of the horizon going to zero, converges to the value computed analytically from the classical model, for the "same" composite material. For example, if we choose a horizon size of about 0.15mm, the crack propagation speed obtained from Eq. (4.36) is about 851m/s. The relative difference between this value and the analytical results (820m/s) is about 3.6%. However, we cannot afford to use such small horizon size to perform the simulation because of the limitation of the computational resources. Please note an important difference between the parameters used in the analytical formula and those used in our peridynamic computations: in the analytical classical approach, the value for G_{II} prescribed, while in our model we input G_I for 0° and 90° fiber orientations. The G_{II} value used in Eq. (4.33) from [69] falls between the two G_I values used in the peridynamic computations (see Table 4.3).

The results show that a sub-millimeter horizon produces maximum crack propagation speed values, in this splitting fracture mode for the given lamina geometry under the given dynamic loading conditions, close to those given by the classical analytical model.

4.5.5 Dynamic fracture for φ=90° under different loading types and magnitude

In this section, we investigate the damage pattern and progression for the 90° fiber orientations (grids orientation perpendicular to fiber direction) under two loading types (see Figure 4.6) and different loading magnitude with the same semi-analytically discretized model as for the 0° fiber orientation. We choose horizon size δ = 2mm and m = 5 to perform the simulation based on previous convergence studies, which can attain a balance between good approximation of the observed behavior and computational efficiency.

For the 90° fiber orientation case, only the splitting mode is observed in both loading cases, when the loading is σ = 2 MPa in Case A, and σ = 8 MPa in Case B (see Figure 4.13a and Figure 4.13c). For the 90° fiber orientation case, the reflected wave reaches the crack tip at the same time and as the same incidence angle. The crack path, therefore, is straight and only the splitting mode is observed for this level of loading. When we increase the loading amplitudes, however, from 2 MPa to 4 MPa in Case A, and from 8 MPa to 12 MPa in Case B, we observe dramatic differences compared to the lower

amplitude loadings (see Figure 4.13b and Figure 4.13d). In both loading cases A and B, after an initial splitting crack growth from the center pre-crack, the cracks *branch*! This indicates a fracture mode change, from splitting to cracks migrating through the matrix over the "fiber bonds". We observe no "fiber bonds" damage at these dynamic loading levels. The branching angles are around 45 degrees. Crack branching in dynamic fracture in brittle materials has been experimentally studied in glass plates [63] and peridynamics has been shown to be able to predict this behavior ([15], [31]). To obtain this phenomenon in the anisotropic UD FRC was a surprise to us. The recent dynamic experiments in [7], however, demonstrate that this phenomenon *actually happens in reality in dynamically loaded unidirectional FRCs*. As in our simulations, the experiments indicate no breakage of fibers in these branching cracks, meaning that the *cracks grow in the matrix migrating over the fibers*. To our knowledge, this is the first computational prediction for this phenomenon. The experimental branching angle, for an experiment in which the specimen is dynamically loaded from its boundaries, was around 45 degrees.

The peridynamic results also indicate that secondary or multiple branching can happen (see Figure 4.13b) and that interaction between the propagating cracks and the stress waves induce some crack-path bending (Figure 4.13d).

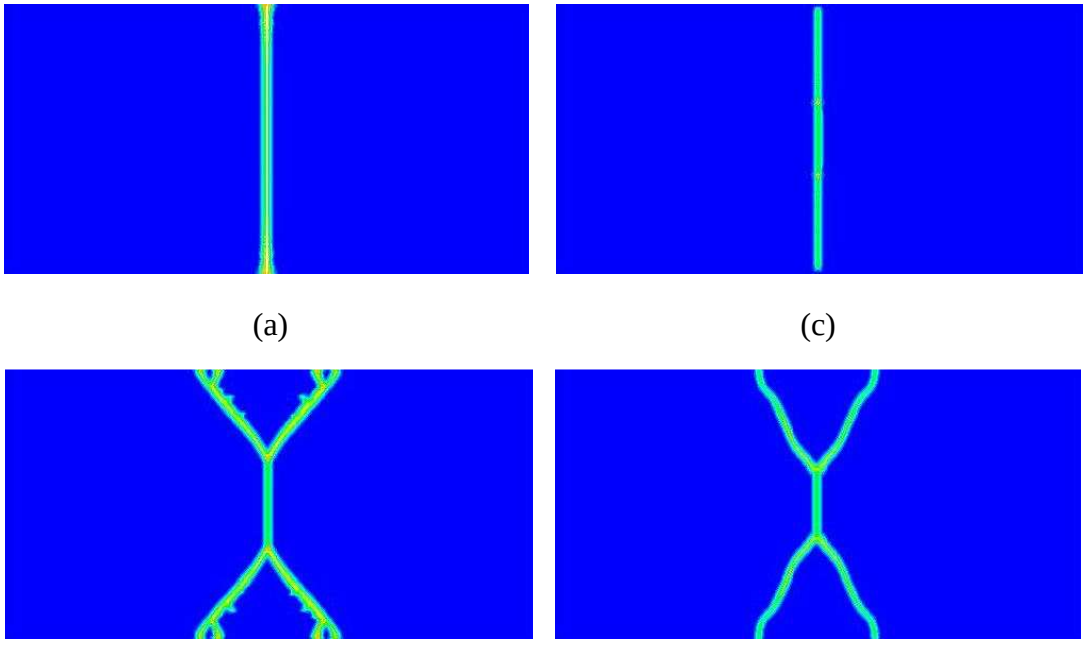

Figure 4.13. Crack patterns for the case φ = 90° under different loading magnitudes: loading Case A with (a) σ = 2 MPa and (b) σ = 4 MPa; and loading Case B with (c) σ = 8 MPa, and (d) σ = 12 MPa.

The relation between the stress waves and crack curving can be seen from the sequence of plots taken at different times for the loading Case B when the load magnitude is 12 MPa, shown in Figure 4.14. The top plots of Figure 4.14 indicate that the reflected waves move towards the center of the plate and meet the branching crack tips at 145 μs. The branches were propagating straight before that. After the reflected waves hit the branch tips, the cracks start to curve as seen from the bottom plots of Figure 4.14.

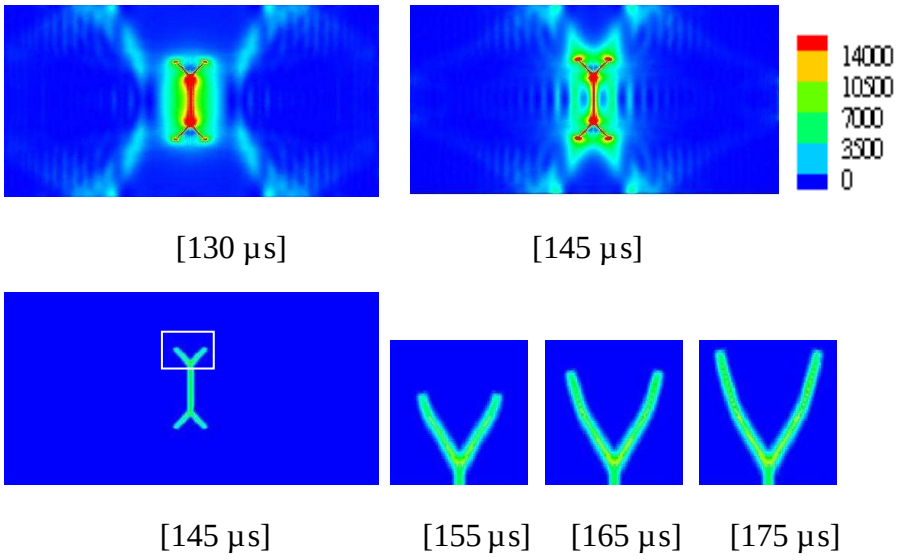

Figure 4.14. Elastic strain energy profiles (top row) and damage maps around the crack tips (bottom row) at different times for loading Case B and σ = 12MPa.

4.5.6 Dynamic fracture for φ=45° under different loading types

In this section, we investigate the damage pattern and progression for the 45° fiber orientations (the angle between the grid and the fiber orientation is 45°) by using the model derived semi-analytically in section 4.4.2. Two different loading cases are employed in order to investigate how the stress waves affect the evolution of the damage process and crack propagation.

4.5.6.1 Damage behavior and crack patterns for the loading Case A

The uniform tensile loading σ = 6 MPa is applied abruptly along the left and right boundary for φ = 45°. The result showing the damage map for φ = 45° is given in Figure 4.15.

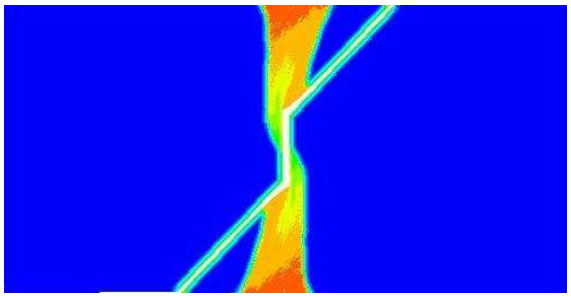

Figure 4.15. Damage map at 500 µs for the 45° fiber orientation under loading Case A.

In all the simulations, the splitting fracture mode is observed without fiber breakage. Interestingly, extensive and diffuse damage in the matrix, beside the splitting mode from the tips of the pre-crack are obtained for φ = 45°, are seen in Figure 4.15. In Figure 4.16 a-c and Figure 4.17, we show a few snapshots of the time evolution of damage maps and strain energy profiles for φ = 45°. As the shock waves propagate in the anisotropic material and meet at the center pre-crack, the splitting mode combines with diffuse matrix cracking. In fact, when the main wave-front moving through the matrix reaches the center pre-crack, matrix cracking is initiated and extensively propagates instead of the splitting mode, between 100µs and 200µs. The matrix in the composite is completely shattered in those regions. Eventually, splitting along the fiber directions starts to progress at about 350µs and full separation of the composite into two pieces follows soon after. Fig. 8d shows that, at these load levels, the “fiber bonds” are not damaged, except for those cut by the pre-crack. Damage of “fiber bonds” is computed by only counting the broken “fiber bonds” and the original number of such bonds. We notice that for φ = 45°, the damage behavior under dynamic loading is more complex than under static loading which only contains the splitting mode [58]. This mixing of extensive matrix shattering

followed by complete splitting is observed even if we lower the magnitude of the dynamically applied tensile loading. In the elastic strain energy density figures (see Figure 4.17), some of the ripples behind the wave fronts are induced by the non-local region (horizon) size and some are a result of the numerical dispersion of the sharp wave. The numerical dispersion can be eliminated by using flux-corrected transport (FCT) algorithms [74].

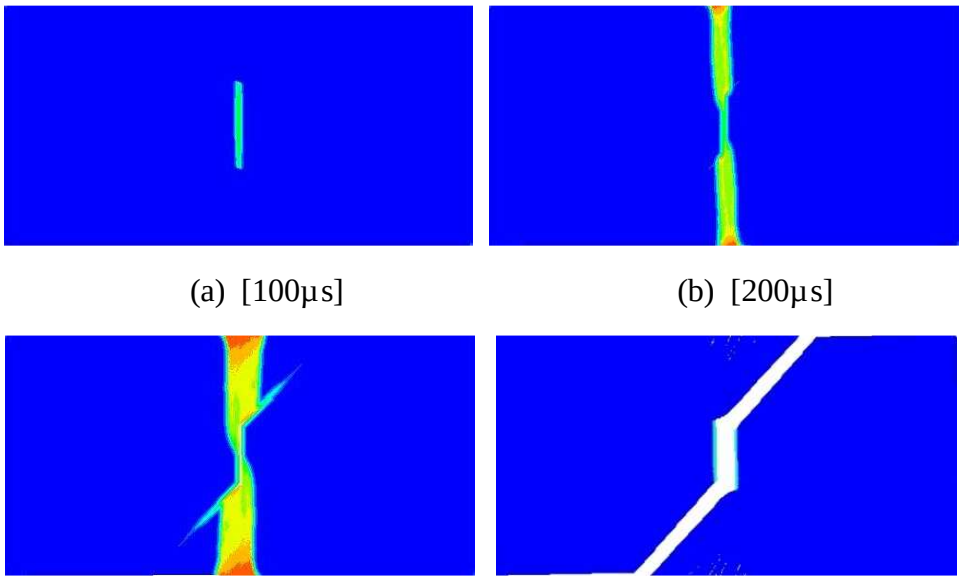

(a) [100μs] (b) [200μs]

(c) [350μs] (d) fiber-damage map

Figure 4.16. Time-evolution of damage for φ= 45°: (a) matrix cracking (at 100 μs); (b) extensive matrix cracking and diffuse damage (at 200μs); (c) extensive diffuse damage and growth of splitting mode fracture (at 350μs); (d) damage map for the “fiber bonds” only (at end of the simulation when total separation due to splitting is clearly visible).

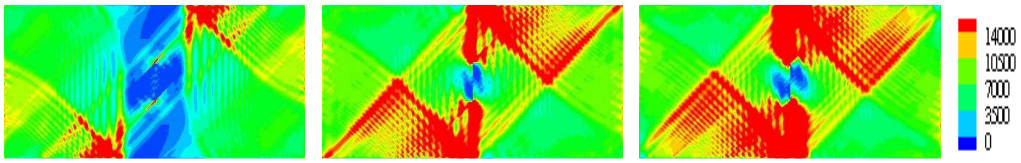

[75μs] [95μs] [100μs]

Figure 4.17. Elastic strain energy profiles just before and after the pre-crack starts propagation.

4.5.6.2 Evolution of fracture and crack patterns for the loading Case B

A uniform pressure loading σ = 10 MPa is applied abruptly along the pre-crack faces (see Figure 4.6) for the case when φ = 45°. The results showing the damage map for are given in Figure 4.18.

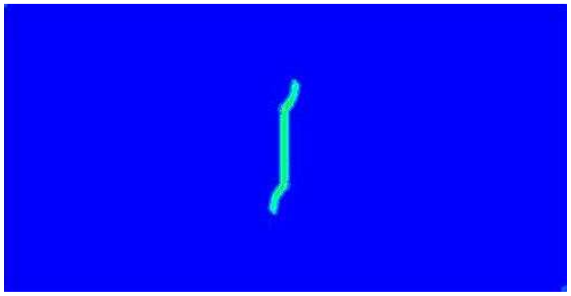

Figure 4.18. Damage map for 45° fiber orientation under loading Case B.

The damage pattern is changed significantly compared with the loading Case A, for this fiber-grid orientation angle. This is seen from comparing Figure 4.18 with Figure 4.15. Under Case B loading conditions, the diffuse matrix cracking is absent and is replaced by a distinct crack growth in the matrix that starts off as splitting fracture but it progresses by bending and thus *migrating over* the "fiber bonds" until it finally arrests in

an almost vertical direction. A close examination of the elastic strain energy density evolution as the crack propagates, shows that the reflected stress waves from the boundaries influence the running crack and induce the bending, migration, and the ultimate arrest of the crack.

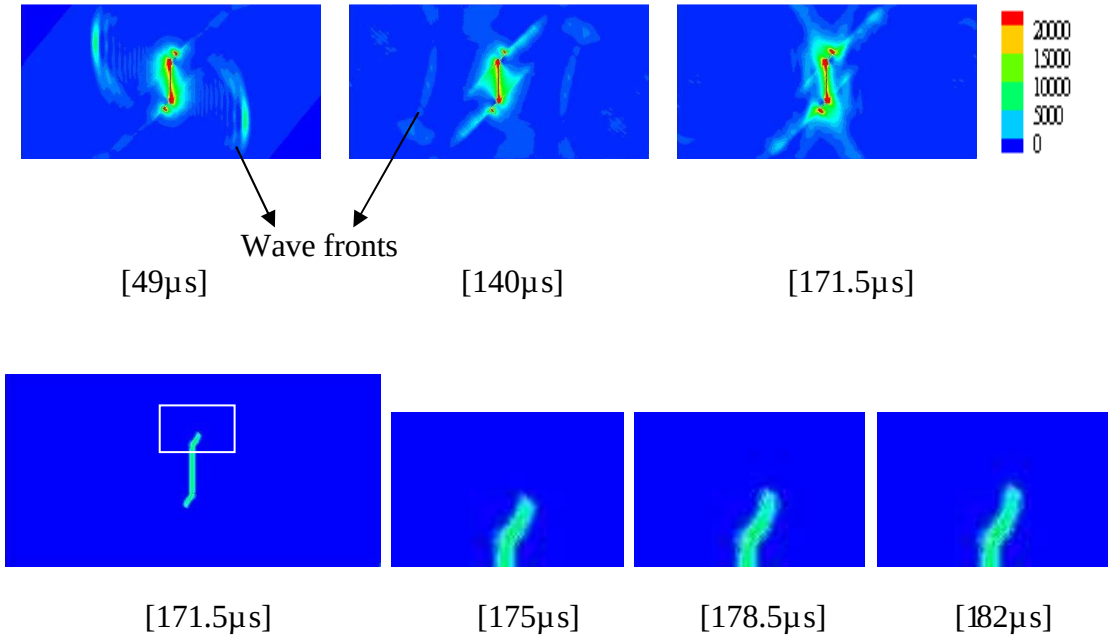

Figure 4.19. Elastic strain energy profiles (top row of figures) and damage maps around the crack tip area (bottom row of plots) for the 45° fiber orientation under loading Case B (loading of the crack faces).

On the top row of Figure 4.19, the elastic strain energy is plotted at three different times to illustrate the elastic wave moving away from the pre-crack faces, the reflected wave from the boundaries, and the interaction of the reflected wave with the crack tip. On the bottom row of Figure 4.19, damage maps show the crack propagation in time. The crack starts to propagate along the 45° fiber orientation, in splitting mode, but

immediately bends and “migrates” over “fiber bonds” without breaking any of them. The stress wave generated by the suddenly applied pressure on the crack faces moves toward to the boundaries and reflects from them at about 91μs. The particular angles at which the reflected wave meets the crack tip results in curving of the crack path. It is interesting to observe that, due to the anisotropy and the asymmetry of the fiber orientation relative to the sample geometry, the reflected waves from the right and left boundaries reach the top crack tip at different times (171.5μs and 178.5μs, respectively) and at different angles. Due to this, the interaction with the stress waves changes the crack growth direction. The role of the dynamic interaction between a crack and a stress wave has been experimentally studied in isotropic materials [75].

Then, we only apply the sudden pressure along the crack surface with two different magnitudes σ = 20 MPa and σ = 33 MPa for φ = 45. The reason is that the character of the damage does not change by further increasing the loading for the other loading case.

In Figure 4.20, we observe that the splitting mode is dominant and the crack advances substantially *before* the reflected elastic waves reach the growing crack. As seen from Figure 4.20a, the splitting fracture transitions in the matrix fracture at the point when the crack is beginning to bend. When the loading is sufficiently strong, the splitting crack runs through and the stress waves do not reach the moving crack in time to cause a fracture mode change (see Figure 4.20b).

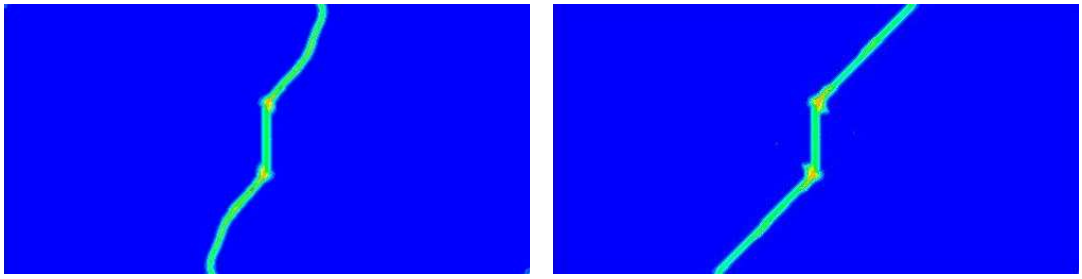

(a) (b)

Figure 4.20. Damage patterns for 45° fiber orientation when the loading magnitudes (Case B, crack face loading) are increased to σ = 20MPa (left) and σ = 33MPa (right).

4.5.7 Convergence studies for an arbitrary grid orientation relative to the fibers using the proposed algorithm

For an arbitrary grid orientation relative to the fiber orientation in the composite lamina, the proposed Algorithm is employed to compute the scaling factors for "fiber bonds" and "matrix bonds". We use two different grids for the same horizon size (*m*-convergence study) and also perform a δ-convergence study. Of interest are the damage patterns and evolution, as well as the development and propagation of splitting cracks. Because of this, we select the loading Case A, since this case, as we have seen above, results in a very interesting combination of diffuse-type damage ("matrix shattering") followed by isolated splitting cracks. Thus, along the left and right boundaries, a sudden tensile loading σ = 6.75 MPa is applied. We use a higher magnitude loading than that in section 4.5.6.1 in order to better observe the damage behavior in the "shattered" region. Given the dynamic nature of the loading, in which wave reflections and deflections from the

boundaries and newly formed crack surface dramatically influence the solution, these are extremely tough tests to pass by any numerical method.

We choose the case in which the angle between the grid and the fiber orientation is $\varphi = 25^{o}$. For the *m*-convergence tests we select only two values for the *m* parameter: $m = 5$ and $m = 7$, and a fixed horizon size $\delta = 4$ mm. Recall that the angle α that provides the cone within which we assign fiber bonds (see Table 4.2) should be, in principle, connected to the *m* value. For simplicity here we use $\alpha = 3°$ for both *m* values. As shown in Figure 4.22, we observe diffuse damage in the matrix and splitting fracture mode in both cases. Furthermore, the angles for the major splitting crack are the same in both cases, and very close to the fiber orientation angle of 25^{o}. Since the nodes picked up by Algorithm (see Table 4.2) that are designated to have "fiber bonds" with the central node are obviously different between $m=5$ and $m=7$ (see Figure 4.7), we conclude that *m*-convergence is achieved. In addition, since these nodes are not aligned in any special way (compare with the 0°, 45°, or 90° orientations) the results also demonstrate that the algorithm will perform the same even when a random, non-uniform discretization is used.

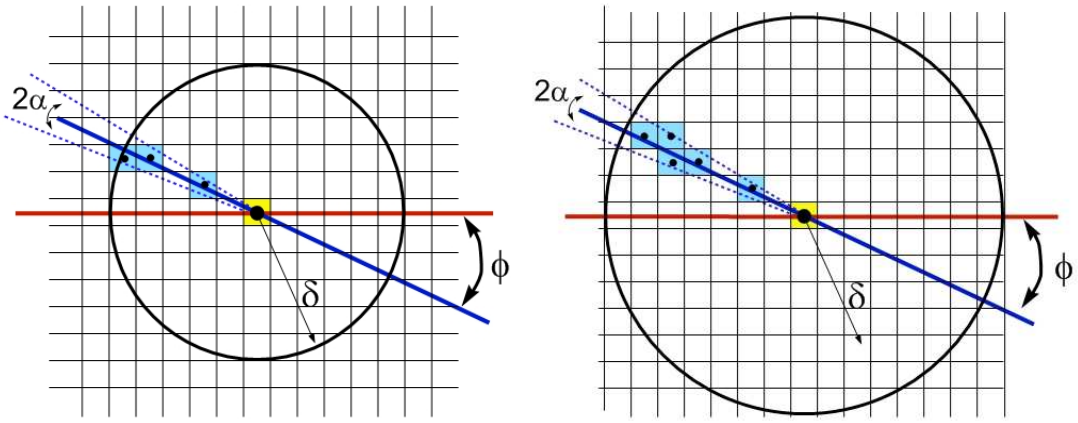

Figure 4.21. The number of nodes (blue) picked up by the algorithm to have "fiber bonds" with central node (yellow) for $m = 5$ and $m = 7$.

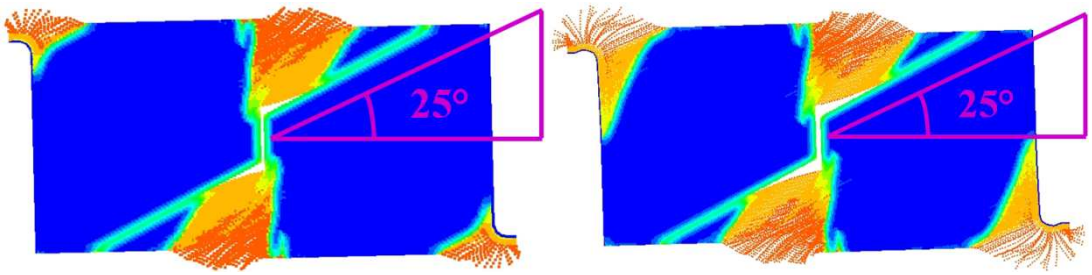

(a) (b)

Figure 4.22. Damage maps for φ = 25° with different m. (a) $m = 5$ at 75.2 μs; (b) $m = 7$ at 78.2 μs.

The large magnitude sudden loading sends shock waves that bounce off the boundaries which creates extra damage zones near the corners of the samples. The no-fail conditions enforced on the peridynamic bonds near the left and right boundaries are now visible. While the shattered matrix region and the splitting crack are almost identical between the two different grids (which use the same horizon size) and obtained at about the same time, the corner-damage is more extensive in the finer grid than in the coarser

grid. This can be explained by how slightly different wave dispersions between the grids interact with the peridynamic bonds. The “matrix bonds” are shattered in the central diffuse-damage region as well as in the corner regions and the “fiber bonds” in these areas become separated. Observe that when $m = 7$ (denser grid) there are more loose “fiber bonds” than in the coarser model with $m = 5$. Interestingly, under the given loading, no “fiber bonds” suffer damage.

In what follows we select $m = 5$ to perform a δ-convergence test for the fiber orientation $\varphi = 25^{o}$. The results will indicate which horizon size is sufficiently small to capture the main features of the damage evolution and for which using a smaller horizon size would not result in qualitatively different results. From a practical point of view, one wants to use a larger horizon size to reduce the computational burden. .We use the following horizon sizes and the resulting discretizations from a value $m = 5$: $\delta = 4$ mm with $\Delta x = 0.8$ mm (31752 nodes), $\delta = 3$ mm with $\Delta x = 0.6$ mm (56112 nodes), and $\delta = 2$ mm with $\Delta x = 0.4$ mm (126002 nodes). The same loading conditions are used as in the *m*-convergence study above.

The results in terms of the damage maps are shown in Figure 4.23. As shown in Figure 4.23 (a)-(c), for different horizon sizes, the similar damage patterns are observed, such as diffuse damage in the “matrix bonds” (shattered matrix) followed (see below for the time-evolution of damage) by the splitting fracture mode. Notice the change in size of the damaged area produced by the meeting of the stress waves in the center, and the subsequent interactions between stress waves reflected from the boundaries. The reason

for the larger damage areas when the horizon is larger is discussed in detail in [15]. As shown in Figure 4.23(d), we do not observe any damage of the “fiber bonds”, other than that generated by the initial center cut. The measured angle of the splitting crack is very close to the fiber orientation $\varphi = 25^{o}$, and is about 26^{o}. Moreover, in the shattered-matrix region, we see ends of “fibers” becoming “loose”. This happens because all the “matrix bonds” for nodes in those regions have been broken. We also observe that the damage around the corner areas is decreasing as the horizon decreases. This damage is produced initially by the abrupt loading, especially with the larger horizon size, and its growth is induced at later times by the stress waves moving through the material. Notice that the times at which the damage maps look similar between the different horizon sizes are significantly different. This is due to the different time-evolution of damage and propagation of splitting cracks obtained when different nonlocal regions (horizon sizes) are used. This behavior is induced by two factors, both related to the horizon size:

1. The wave dispersion of stress waves depends on the horizon size (see [28]), and
2. The “thickness” of the damage zone is related to the horizon size (see [15]).

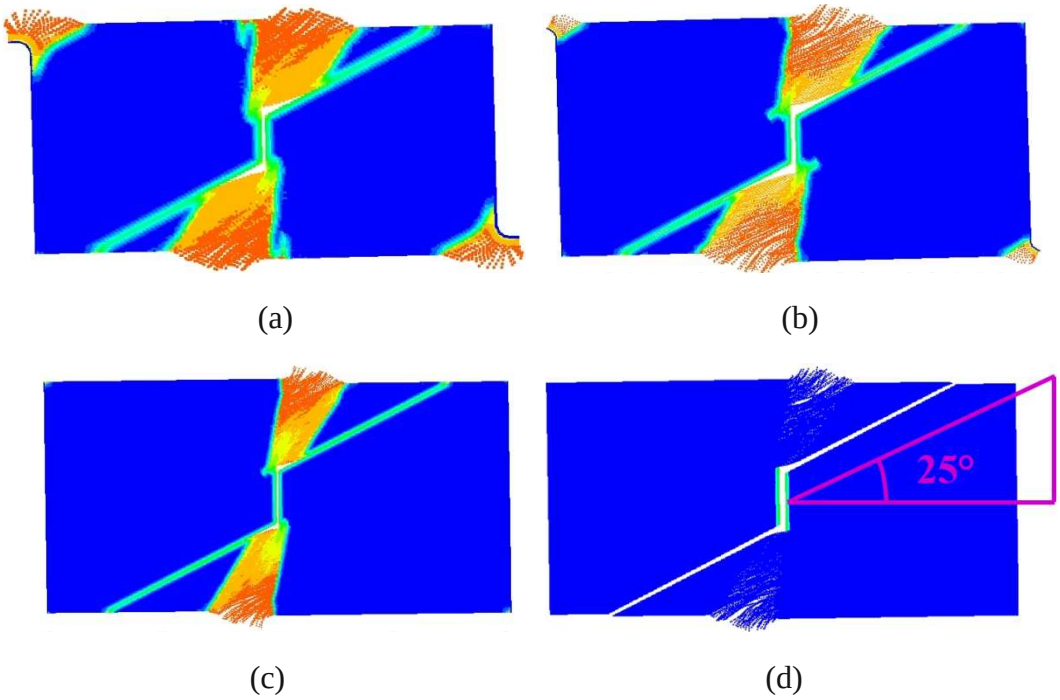

Figure 4.23. Damage maps for φ = 25° at different horizon size. (a) δ = 4 mm at 75.2 μs; (b) δ = 3 mm at 90 μs; (c) δ = 2 mm at 135 μs; (d) The damage map for "fiber bonds" only.

In what follows we discuss in detail the time-evolution of damage and how the two factors mentioned above play a role in influencing when the splitting cracks start propagating and how fast they grow. The damage maps and elastic strain energy plots for both δ = 4 mm and δ = 2 mm at different times are shown in Figure 4.24-Figure 4.26. The damage of "matrix bonds" in the central region happens immediately after the shock waves arriving from the left and right boundaries reach the pre-crack at about 10.5 μs. The damage pattern and strain energy profiles for two different horizon sizes are approximately the same at this time. However, the oscillations behind the shock front, which are caused by the wave dispersion induced by nonlocality, become smaller with a

decreasing horizon size. At about 24 µs, the damage patterns are about the same but the stress waves start showing some more pronounced differences, especially near the damage region, as seen from the strain energy density maps in Figure 4.25. The horizon size influences the effective "thickness" of the damage zone (see [15]) and we start to observe a thicker shattered matrix region. That, in turn, significantly influences the reflection and deflection of the stress waves that continue to damage the composite as they travel through the sample.

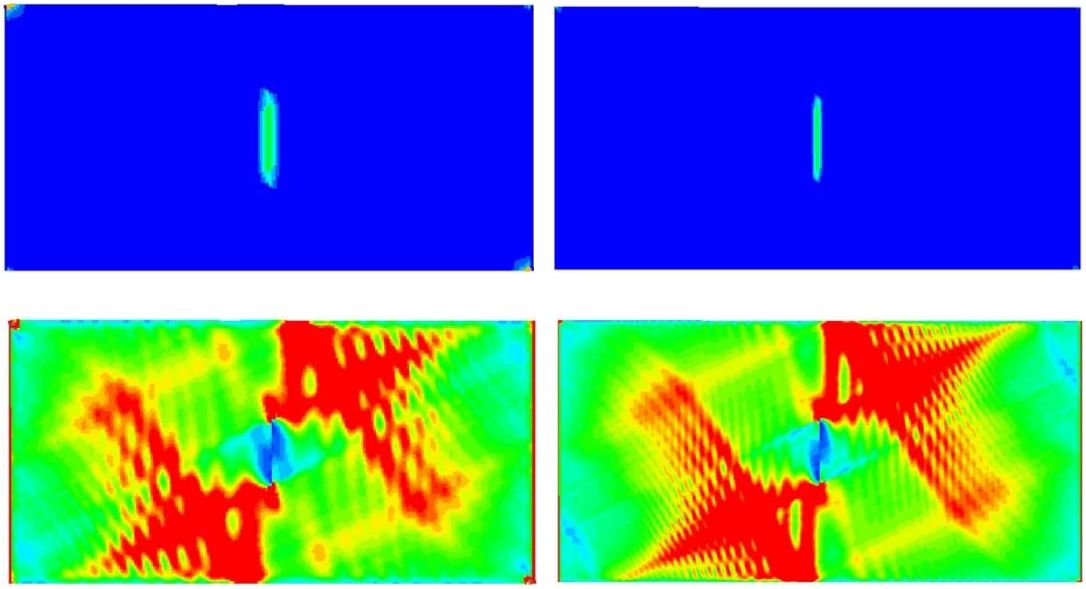

Figure 4.24. Damage maps (top) and strain energy density plots (bottom) for δ = 4 mm (left) and δ = 2 mm (right) at about 10.5 µs.

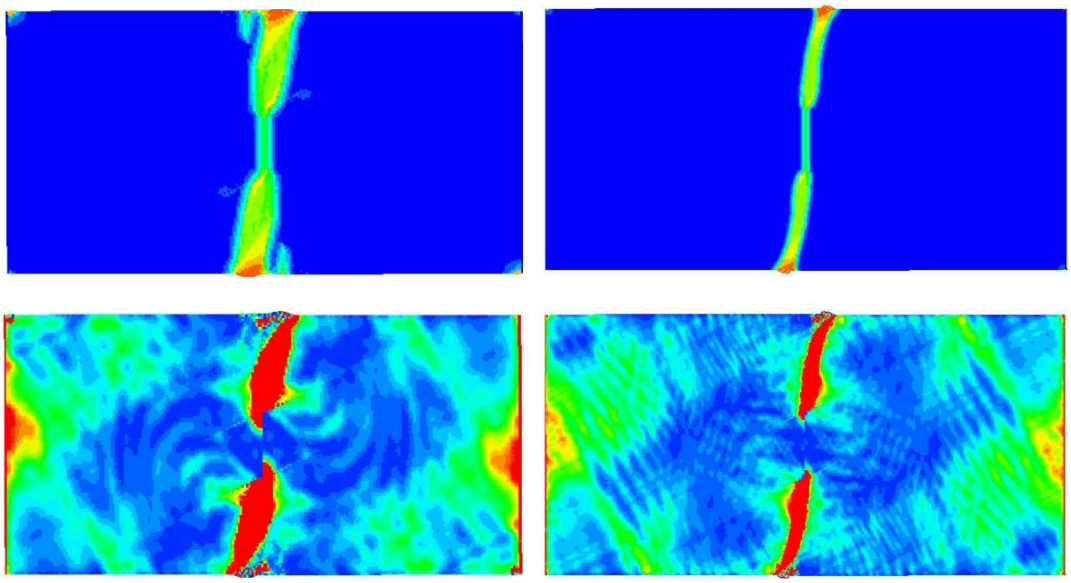

Figure 4.25. Damage maps (top) and strain energy density plots (bottom) for δ = 4 mm (left) and δ = 2 mm (right) at about 24 µs.

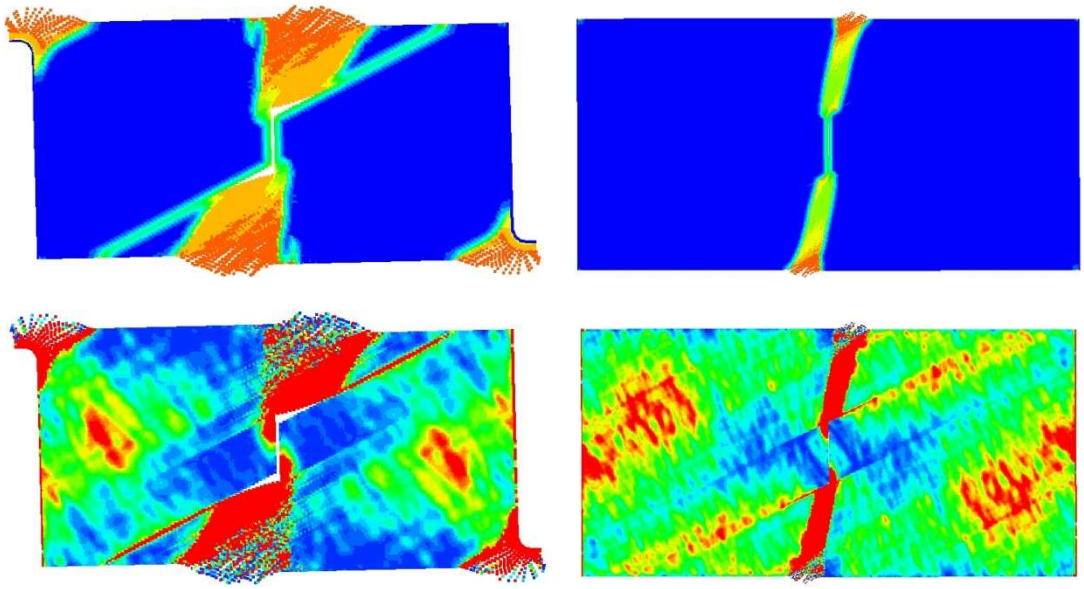

Figure 4.26. Damage maps (top) and strain energy density plots (bottom) for δ = 4 mm (left) and δ = 2 mm (right) at about 75.2 µs.

We roughly estimate the average crack propagation speed for the splitting crack and obtain that is about 5600 m/s for $\delta = 4$ mm and about 3400 m/s for $\delta = 2$ mm. While the longitudinal waves speed is the same independent of the horizon size (the micromodulus functions are obtained so that the microelastic material has the same elastic modulus as a classical material) the crack propagation speeds are lower for the smaller horizon size (see, e.g. [15], [31]). We explain this as follows: the trailing waves behind the shock front (induced by both the nonlocal region size and the numerical discretization and modified by reflections from boundaries) can strongly influence the crack propagation speed, by speeding it up or slow it down. We observed the same behavior in the case with 0° fiber orientation. It is important to notice that when the loading is so that, at least for a while, the crack propagation is not influenced by stress waves, the crack propagation speed *does not* depend on the horizon size. This is demonstrated in [47] by applying sudden loadings on the faces of a pre-crack.

4.6 Summary

In this section, we proposed a new homogenized peridynamic model for simulating fracture in a unidirectional (UD) fiber-reinforced composite lamina. Then, we introduced a computational model of the homogenized peridynamic formulation for unidirectional (UD) fiber-reinforced composites (FRCs). The model can be used with any type of uniform or non-uniform discretization, and for any fiber orientation relative to the grid orientation. For the special case when the angle between the fibers and a uniform grid is

0^o, 90^o, or 45^o we derived, semi-analytically, the scaling factors in the model. For the general case, we introduced an algorithm that correctly scales the discrete model so that the computed strain energy density in the composite is independent of the grid spacing or the grid orientation relative to the fiber direction.

Then, we use this model to compute dynamic fracture and damage behavior for 45 and 90 degree fiber orientations. We performed convergence studies for the grid aligned with fiber orientation and arbitrary grid orientation in terms of grid refinement for a fixed horizon size and in terms of decreasing the horizon size. We also compared the maximum crack propagation speed from the peridynamic simulations with an analytical solution for a steady-state dynamic debonding crack. The peridynamic solutions show a maximum crack propagation speed for the splitting mode that approaches the theoretical dynamic debonding solution when the horizon goes to zero. The propagation of the splitting crack type was shown to match the angle of the fiber orientation. We capture interactions between stress waves and crack propagation behavior for UD FRC. Because of the dynamic loading, the damage pattern, crack propagation path, and crack propagation speed is strongly affected by the stress waves in the body. Our results agree well with recent experimental results.

We capture the strain-rate dependence of fracture modes without introducing the strain-rate parameters into our model. The brittle fracture in composite material is strain-rate dependent because of dynamic loading effects (inertia and stress wave propagation).

No special criteria for splitting fracture, for crack curving or crack branching, or for transitions between fracture modes were used. The nonlocal region (the peridynamic horizon) was selected so that it would be sufficiently small relative to the geometric and dynamic conditions in order to efficiently obtain results deemed close to converged ones.

Chapter 5
Impact fracture and damage in glass laminates

5.1 Introduction

Glass laminates are widely used in skylight glazing and automobile and train windshields due to the low cost manufacturing, light weight, and high performance. In the military, glass laminate armor on military vehicles has become an important issue in recent years [76]. Thus, it is important to understand the damage and fracture behaviors of glass laminates under impact in order to design and improve glass laminates protect system.

Many experiments have been conducted to analyze the behavior of single glass plate or glass laminate subject to low or high impact velocity. Knight et al. [77] found that the Hertzian cone angle decreases with impact velocity for a glass block under small steel

spheres impact. In [78] the impact of small steel ball on glass surfaces was studied. The use blocks of glass samples were used in the impact tests and different cracking mechanism such as lateral crack and radial crack were observed. Ball and Mckenzie [79] performed a series of impact tests on circular float glass plates with thicknesses between 3 mm and 12 mm with various impact speed (10 - 50m/s). They identified a number of failure mechanisms in the plates and were able to establish a fracture map incorporating the effect of plate thickness and impact velocity. Behr et al. [80] discussed that when the glass ply is thin, the bending and membrane effects will be more dominant in the fracture process and the damage and fracture will be dramatically different from that of a glass block under impact. Moreover, Kim et al. [81] evaluated the effects of back plate material on cone crack formation in glass plates impacted by small spheres under various impact speeds. The specimen thickness and the material of back plates have influence on the damage pattern under certain impact velocity [81]. The glass laminates subject to high velocity impact is very complex damage pattern by dynamic brittle fracture through layers. Bless et al. ([82], [83]) studied of high velocity impact phenomenology onto layered glass for impact speed at 1120 m/s. For instance, a characteristic “spider web” cracking pattern that comprises with multiple radial and circumferential cracks, prevents the glass layer from complete piercing of impact. The experiments of two glass material (first layer is glass plate and the second plate is polycarbonate, no glue between layers) under different impact velocities (from 61 m/s to 300 m/s) are performed by [84]. From experiment results, the number of radial cracks and circumferential cracks increases when the impact velocity increases. The fragmentation appears on the glass plate when impact

velocity larger than 100m/s. Near the impact site, the polycarbonate layer experience permanent deformation only when impact velocity larger than 200 m/s.

Experimental investigations of the glass behavior about the impact at various velocities are well studied and documented. However, it is a challenge to develop a model that can correctly capture all the observed features of dynamic fracture and fragmentation from impact. Numerical studies based on finite element method or molecular dynamics have been performed to compute the response of glass plate under impact loading. Explicit damage models are needed in the simulations. In [85] radial cracks for a glass laminate under low impact velocity are captured by using shell elements with brittle failure. However, special mesh topology is required in order to obtain the radial cracks, circumferential cracks and only certain shape of fragments (for example, sector). In [86] used stress-based continuum damage model to describe the constitutive behavior of glass and the contribution of different cracking systems is explicitly taken into account. They studied the initiation and propagation of the ring/cone crack in a glass plate under impact based on this model. A “nonlocal failure criterion” was introduced by [87] based on the experimental observations. The area of damage region is correctly captured but not the damage pattern with this model. These difficulties are due to undefined derivatives at the discontinuities. In [88] the fracture of glass through hypervelocity impact are studied by using large-scale molecular-dynamics simulations but with a sample in nanometer scale.

Peridynamic formulation does not involve in derivatives. Hence, peridynamics can capture the damage initiation and crack propagation with arbitrary directions without any

ad-hoc criteria. Impact damage on a brittle glass cylinder under sphere impactor has been studied by using different influence functions in [89]. In here, we use three-dimensional bond-based peridynamic model and show that the peridynamic model can reproduce most of the dynamic brittle fracture characteristics of a glass plate observed in the experiments [3] and [84].

5.2 Discussion of experiments results for glass plate under impact

Two layer glass laminate target is tested (Yu from ARL [84]): One layer of square soda-lime glass plate of 10.16cm × 10.16cm × 0.33 cm, and a backing layer of square polycarbonate of 10.16cm × 10.16cm × 0.3 cm (See Figure 5.1). A spherical rigid projectile (440C stainless steel) with 0.556 cm diameter and 0.692 g is shot vertically into the center of top glass layer at different initial velocity of 61m/s and 200 m/s. The frame is 10.16cm × 10.16cm with a 5.08cm × 5.08cm opening. The inside surface of the frame is lined with a 1mm thick rubber gasket.

The impact damage on glass laminates are shown in Figure 5.2. Under low impact speeds (61 m/s and 100 m/s), radial cracks and a few circumferential cracks form on the glass plate and no visible damage take place on the polycarbonate aside from surface scratches. Moreover, the projectile is rejected from the target at about 2.6m/s and 7.8 m/s, respectively. Under higher impact speeds (200 m/s and 300 m/s), more radial cracks and circumferential cracks are observed in the experiment. No cracks are observed on the

polycarbonate layer. However, the permanent deformation and small indentation on the polycarbonate near the impact site are observed. The projectile is still rejected from the target at about 33 m/s and 46 m/s, respectively.

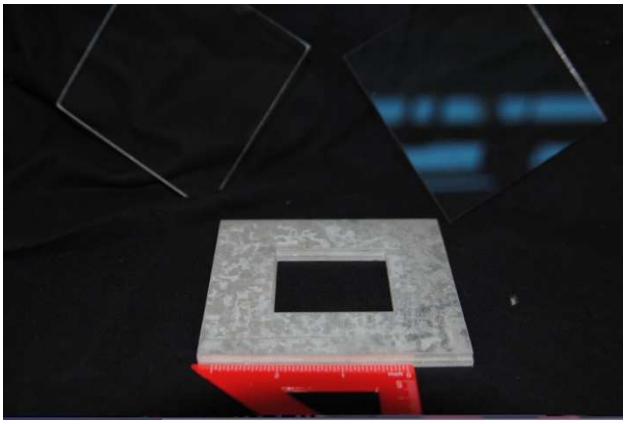

Figure 5.1. Experiment setup from Yu [84].

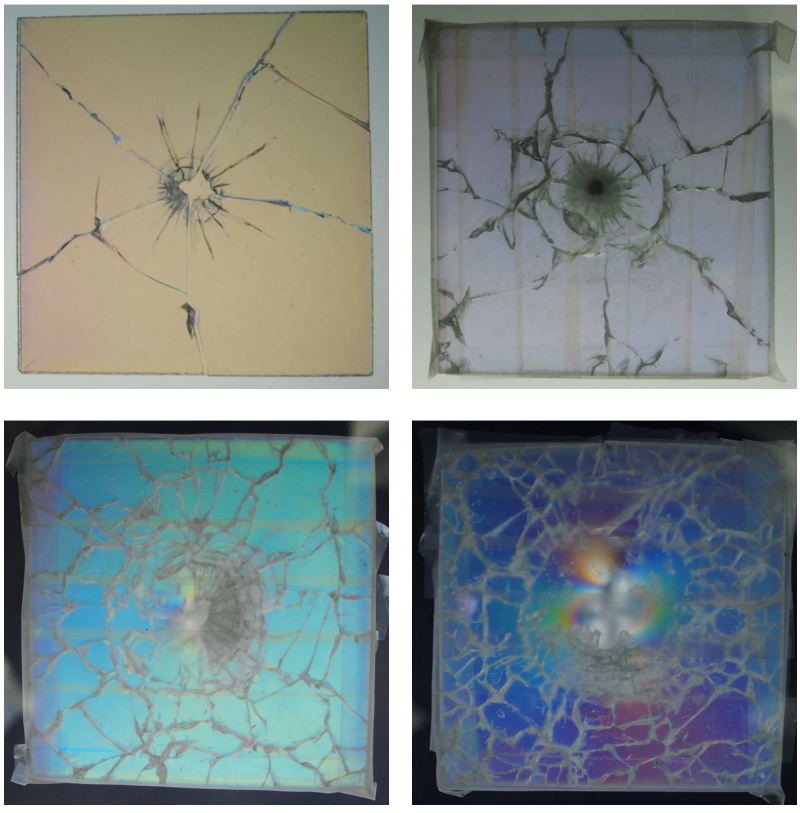

Figure 5.2. Experimental results for glass layer under various impact speed from 61 m/s to 300 m/s (from [84]).

For these impact speeds, the projectile perforates the glass plate but not polycarbonate plate. The ballistic impact of polycarbonate in penetration and perforation by spherical projectile was studied by [90]. Five mechanism of deformation and subsequent fracture of the plate are identified, such as elastic dishing (flexural and stretching deformation of an annular region of the plate surrounding the projectile impact point), petalling, deep penetration (embedding of the projectile into the plate without a failure of the distal face), cone cracking and plugging. In [90] two failure mechanisms are also mentioned that appear to be significant as energy processes (energy dissipation). For the case of thin plates the 80%-90% of the energy dissipated is absorbed by elastic dishing and the plastic bending of the petals, and very little energy is dissipated by cracking. Moreover, the minimum speed for perforation is also given for certain thickness of polycarbonate layer.

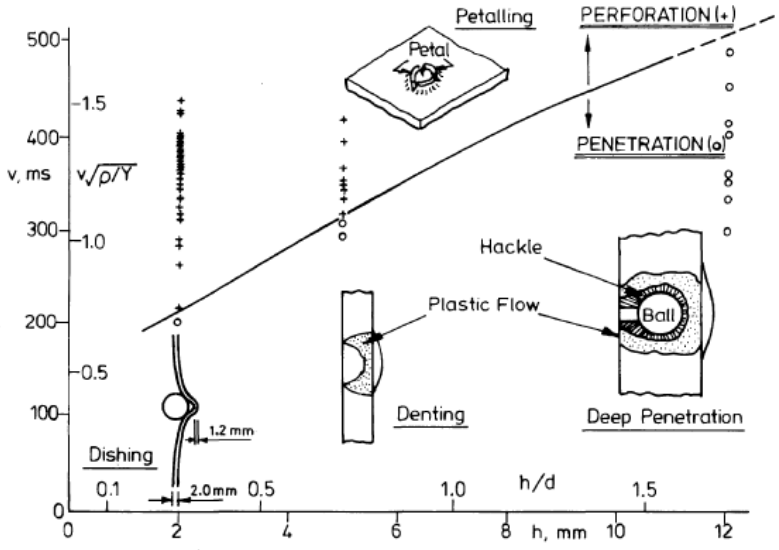

Figure 5.3. Failure mechanism for spherical bullet impact of polycarbonate [90].

Another set of impact experiment on glass plate are performed by [3]. The planar dimension is the same as in Yu's [90] but with the thickness of 5 mm for glass plate. They use rubber as backing material, which has different mechanical properties than polycarbonate. The Figure 5.4 shows the damage patterns under different impact loading rates. The main damage events are for both experiments are similar, such as radial cracks and circumferential crack. However, more structured damage features are seen in [3] than in Yu's experiment [84]. One possible reason is that the thickness of glass plates is different in these two experiments. When the glass layer is thin, the bending and membrane effects of glass plate will be more dominant in the fracture process and cause more damage as suggested in [80]. Moreover, the backing material is polycarbonate in Yu's experiment and Bouzid et al. use rubber as backing material. Thus, under dynamic loading, the amount of energy dissipation and the behavior of stress wave have significant differences between those two different backing materials since polycarbonate is much stiffer than rubber, which will influence the damage patterns. In [81] crack development in soda-lime glass is studied by ball drop with back plate materials of Polyurethane, PMMA, and Aluminum. The diameter of the ball and the thickness of the glass plate and properties of the backing materials influence the velocity range for producing ring crack, perfect cone crack, and lateral and radial crack. In other words, the damage patterns in glass plate may varies under same impact speeds but with different backing materials.

We also observe that there are more fragments seen in [84] under high impact speed. The residual stress field in glass plates may be the reason for the different damage patterns. In fact, residual stresses are often present in brittle materials either by design or

as a consequence of processing. Especially, under high velocity impact, the high amplitude of the longitudinal stress waves may cause extensive damages in the regions where the residual stresses exist. Moreover, the damage progression of thinner plate tends to more sensitive to the residual stress than the thicker plate.

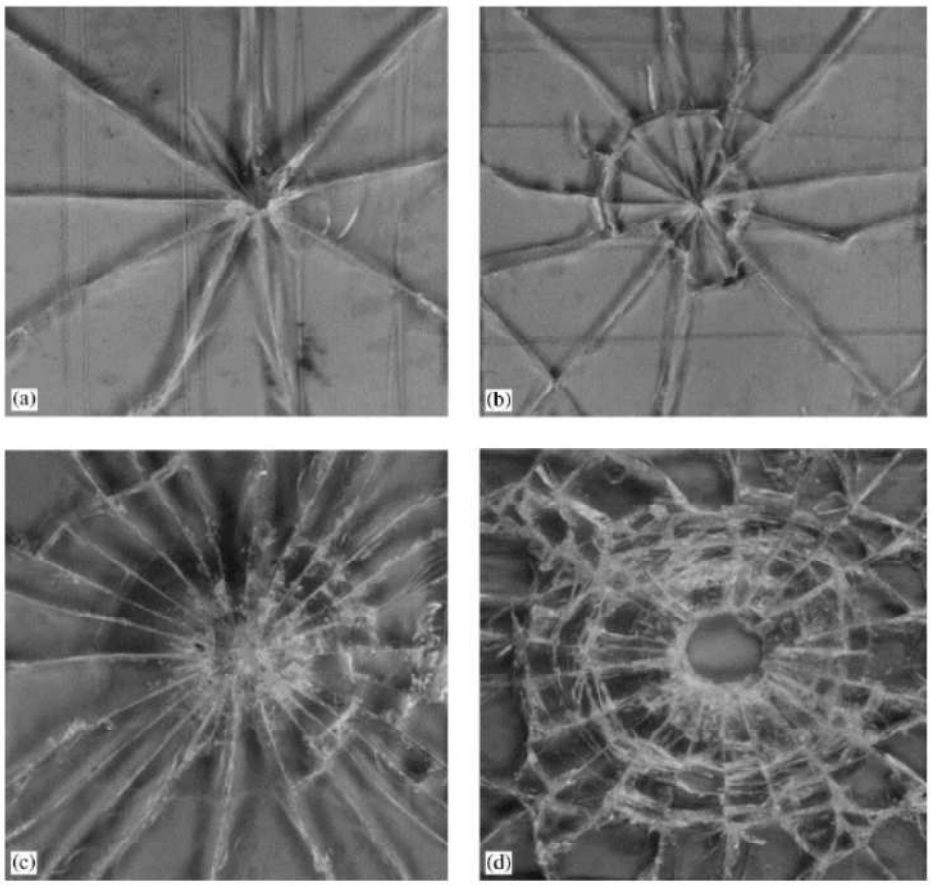

Figure 5.4. Experimental results for glass layer under various loading rates from [3].

5.3 Computational model

5.3.1 Problem setup

We use same geometry size as in the experiment (see Figure 5.5): 1) two plates have the same planer dimension with 10.16cm × 10.16cm; 2) the first layer has the thickness of 0.33 cm while second layer has the thickness of 0.3 cm. All simulations in this paper are 3D simulation based on EMU from Sandia [91]. The two materials used here soda-lime glass and polycarbonate. The material properties are summarized in Table 5.1. We use a rigid spherical impactor with diameter 0.556 cm and 0.692g, which is shot vertically into the center of the top layer.

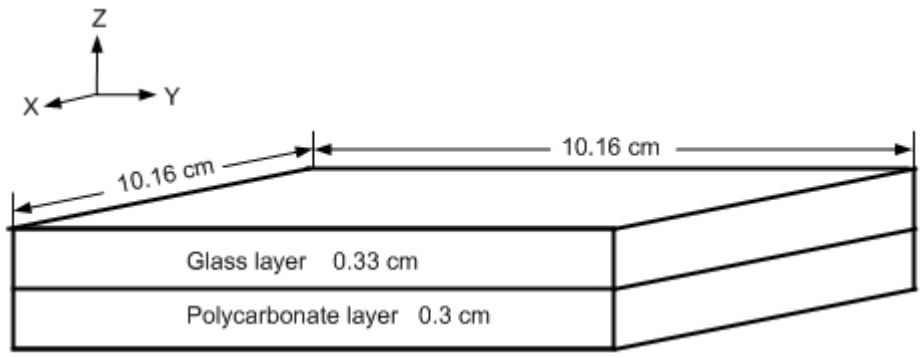

Figure 5.5. Geometry dimension for numerical simulation.

Table 5.1. Material properties.

Material	Young's Modulus	Poisson's Ratio	Density
Soda-lime glass	72 GPa	0.22	2440 kg/m^3
Polycarbonate	2 GPa	0.37	1200 kg/m^3

For the plate under impact, the constant critical relative elongation may result in overprediction of fragmentation. Thus, we choose to "strengthen" the material in

damaged regions by increasing s_0 depending on the amount of damage at that node. One could attempt an exact evaluation of the damage-dependent (variable) s_0. However, here we resort to a simpler way, namely an approximation proposed by [92] which is described by the following formula

$$s = \begin{cases} s_0 \times \min\left[\gamma, 1+\beta\times\dfrac{D-\alpha}{1-D}\right], & \text{if } D > \alpha \\ s_0, & \text{otherwise} \end{cases} \tag{5.1}$$

where the damage index D is defined as the ratio of the number of broken bonds to the number of initially bonds. s_0 and s are an initially given and computed critical relative elongation parameters. Also, α, β, and γ are damage stretch coefficients: if $\alpha = \beta = 0$ and $\gamma = 1$ we recover the constant s_0 model. The Coulomb friction between projectile and target is included in this model. The coefficient of friction is 0.5.

5.3.2 Difference between experiment and simplified computational model

As mentioned in section 5.3.1, we introduced a computational model to simulate the damage pattern and ballistic performance of the two layer laminates under impact. However, our model is a simplified model compare with actual experimental set up. Thus, this model may not capture some experiment phenomena correctly. In this section, we discuss some factors may influence the damage patterns of multilayered glass systems but not included (well present) in our model in detail:

- Boundary conditions – In Yu's experiment [84], the clamp are used in order to hold the metal frame, rubber gasket, glass plate and polycarbonate together (see Figure 5.1). The location of the clamps and amount of clamp pressure applied on the sample influence the damage pattern. Because the pre-stress regions will be created near the clamps, the stress wave may initiate the cracks in those regions therefore the stress wave behavior may be changed. In the model, we simply fix the displacement on x, y, and z direction except opening instead of the using clamp. Thus, some damage features may not be correctly captured, for instance, the number of fragments and radial cracks.
- Interface conditions – In [84] and [3], no glue are used in order to bond with glass layer and polycarbonate but friction resists motion of two plate surfaces in contact. Some energy can be dissipated by the friction. Moreover, wave phenomena depend substantially on the friction [93]. Friction may influence the damage pattern on the back face of the glass layer. In our model, simple contact model are used between the glass layer and polycarbonate layer. Thus, we may observe more damage in the simulation compare with experiment.
- Backing material – Polycarbonate has been used as backing material for two layers system in experiment [84]. The material has an unusually high yield strain and ductility. Thus, polycarbonate displays impressive impact and perforation resistance. In our current model, we use peridynamic elastic model for polycarbonate with unbreakable condition. Therefore, polycarbonate layer can stretch to infinite without stopping the projectile in our simulations. Thus, we are

not able to capture the phenomena of projectile rejected from the target in the simulations.

In fact, many other factors, such as deformation of the projectile (erosion), need to be considered in order to capture all the dynamic brittle fracture in glass plate and projectile behavior under high velocity impact. We do not include all these factors in our model. However, we may capture main damage events by using the current model. In future, we will introduce those factors into our peridynamic model.

5.4 Numerical results and discussion

5.4.1 Convergence tests

In this section, we will perform convergence studies (δ-convergence and *m*-convergence) in order to provide a reasonable grid size to capture the damage and fracture pattern. In order to balance between the computational efficiency and accuracy, we only consider a layer of square soda-lime glass plate of 3 cm × 3 cm × 0.3 cm without back plate as shown in Figure 5.6 to perform the convergence studies. The material properties for soda-lime glass are shown in Table 5.1. The facture energy used in here is 135 J/m^2. A spherical rigid projectile (440C stainless steel) with 0.278 cm diameter and 8.7 g is shot vertically into the center of top glass layer at initial velocity 200m/s. We fix the vertical displacement (z-direction) on both the top and bottom surface except the opening 2.5cm × 2.5cm. For all the following simulations, we use 100 processors with 2.2GHz/64 bit Opteron on cluster.

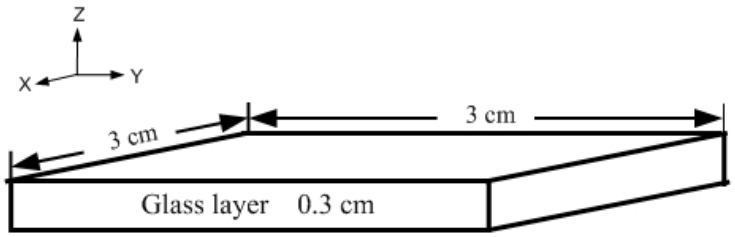

Figure 5.6. Geometry configuration for glass model.

We first perform the m-convergence study for the fixed horizon size δ = 1 mm with m = 3 (82810 nodes), m = 4 (190333 nodes), m = 5 (364816 nodes), and horizon size δ = 0.5 mm with m = 3 (622459 nodes), m = 4 (1452025 nodes), and m = 5 (2827324 nodes). We use the damage range for the color-bar of the damage index in all damage map plots.

As shown in Figure 5.7 and Figure 5.8, the similar characteristic of the impact damage, such as radial crack, circumferential crack and some small fragments, are observed at about the same time. Since the wave dispersions between the grids interact with the peridynamic bonds are slightly different, the damage patterns may not match to each other exactly with different discretization. Interestingly, the number of radial crack increases while m increases. This is because when m increases, there are more peridynamic bonds can be broken, which allows a sufficiently large number of directions along which the true crack path can develop. Thus, if we have enough computational resources, we may use large m (e.g. 10 or 12) in order to obtain more accurate results.

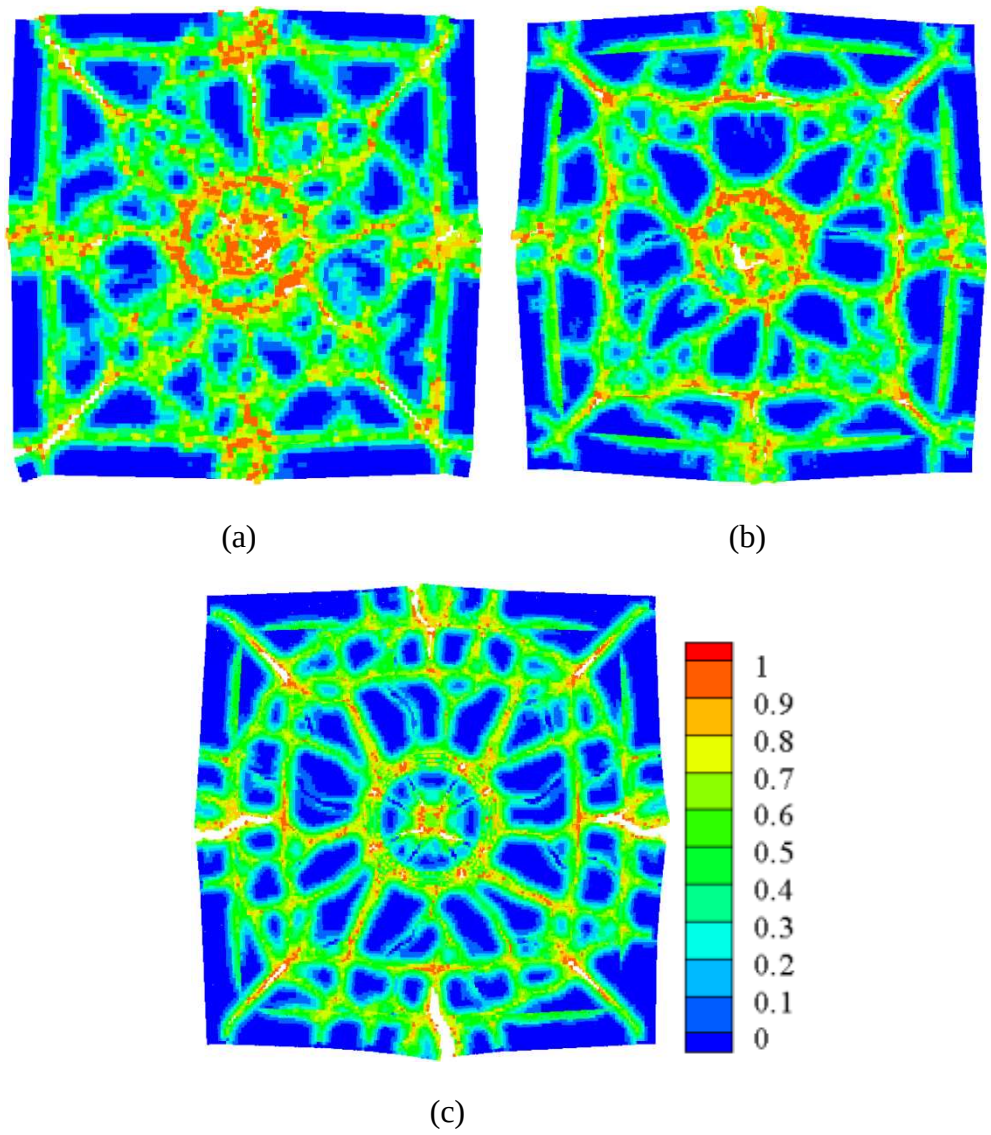

Figure 5.7. Top face damage map for horizon size δ = 1 mm with different *m* at about 27μs: a). *m* = 3 with perforation speed about 180.3 m/s; b) *m* = 4 with perforation speed about 179.9 m/s; c) *m* = 5 with perforation speed about 179 m/s.

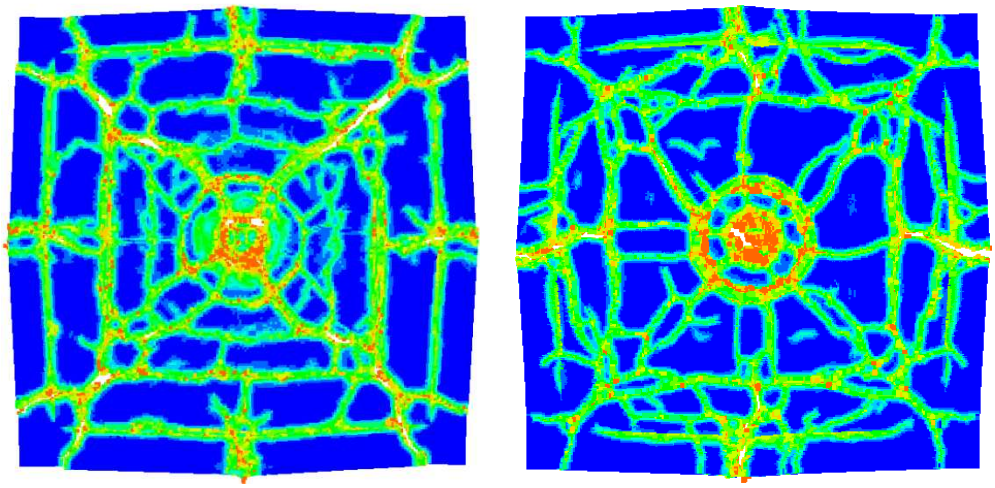

(a) (b)

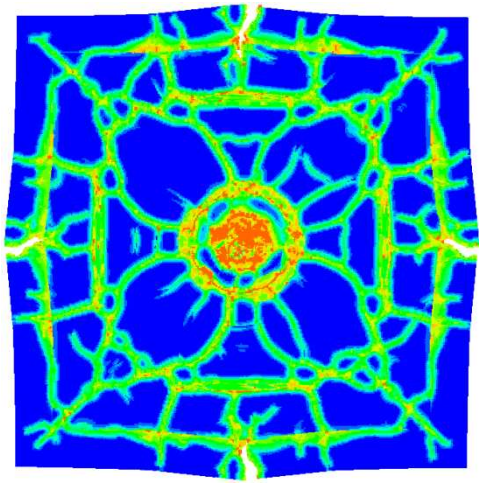

(c)

Figure 5.8. Top face damage map for horizon size δ = 0.5 mm with different *m* at about 27μs: a). *m* = 3 with perforation speed about 183.2 m/s; b) *m* = 4 with perforation speed about 183 m/s; c) *m* = 5 with perforation speed about 182.3 m/s.

In what follows we select *m* = 4 to perform a δ-convergence. We note that for *m* = 4 the main damage events can be captured but requires much less computational effort compare with *m* = 5. We use the following horizon sizes: δ = 2 mm with Δx = 0.5mm (26047), δ = 1 mm with Δx = 0.25mm (190333 nodes), δ = 0.5 mm with Δx = 0.125mm

(1452025 nodes). The same projectile size and impact speed are used in the *m*-convergence studies.

The results showing the damage map for each horizon sizes are given in Figure 5.9. For largest horizon size $\delta = 2$ mm, the glass plate are shattered because of strong nonlocal effect, which induce a much higher crack propagation speed than realistically expected. For other horizon sizes, the similar damage patterns are observed, such as radial crack and the shape of circumferential crack. Moreover, the projectile speed curve and perforation speed start to converge as shown in Figure 5.10. We could use horizon size of $\delta = 0.5$ mm or even smaller to perform the simulations. However, the smaller horizon size requires much more computational resources and we cannot afford to perform the simulation with current computational resources that we have. Thus, in practice, we may use larger horizon size $\delta = 1$ mm, which is sufficiently small to capture the main features of impact damage qualitatively and reduce the computational burden.

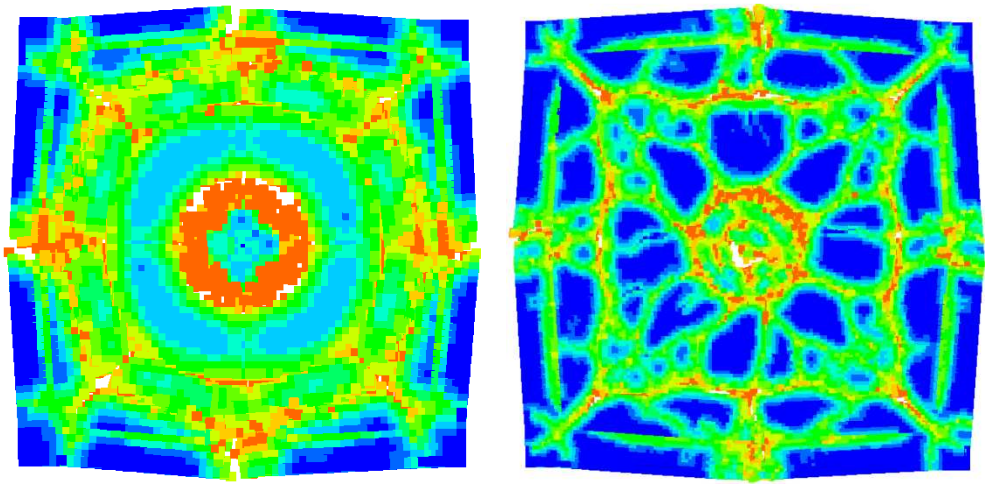

(a) (b)

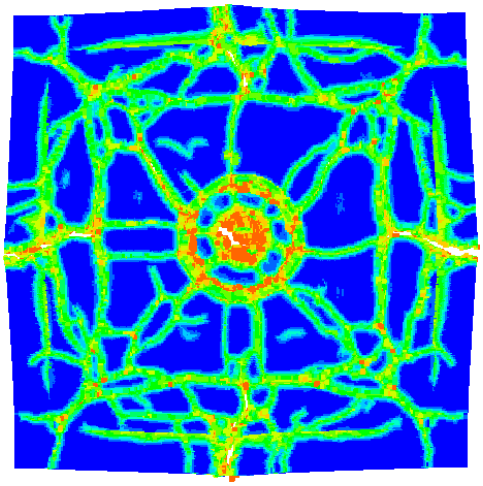

(c)

Figure 5.9. Top face damage maps for m = 4 with different δ at about 27μs: a). δ = 2 mm with perforation speed about 168.6 m/s ; b) δ = 1 mm with perforation speed about 179.9 m/s; c) δ = 0.5 mm with perforation speed about 183 m/s.

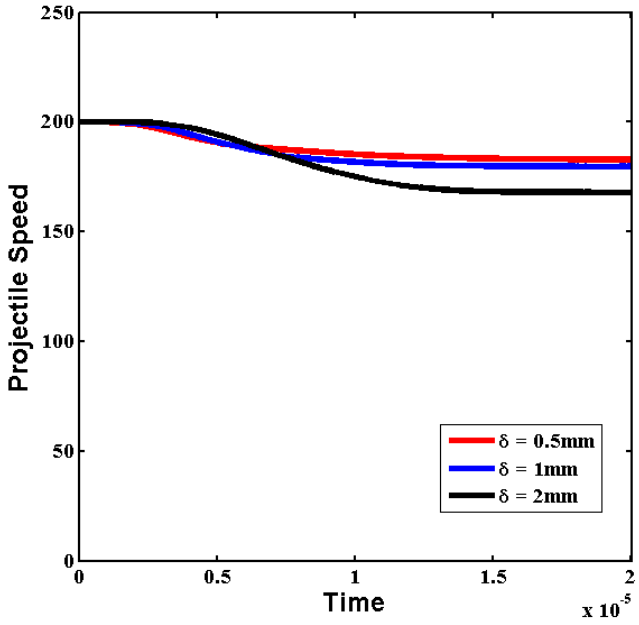

Figure 5.10. Projectile speed profiles for different horizon sizes.

5.4.2 Impact damage on a glass layer with polycarbonate plate under various impact speeds

In this section, we perform the simulation for a multilayered system a glass plate and a polycarbonate plate under two different impact velocities. The geometry setup is shown in Figure 5.5. In order to mimic the boundary conditions in the experiment [84], we fix the vertical displacement (z-direction) on both the top and bottom surface except the opening 2.5cm × 2.5cm. We also fix the horizontal displacement (x and y direction) about one horizon away from the boundaries through the thickness. We “disconnect” all the bonds between two different material regions since no adhesive layer is placed between glass plate and polycarbonate plate in the experiment. Simple contact conditions

are used between two plates. The fracture energy for soda-lime glass is 8 J/m^2 (measured under the quasi-static loading condition). Note that the polycarbonate plate is flexible and unbreakable in the simulations.

From the discussion of the convergence studies, we choose the horizon size $\delta = 1$ mm and $m = 4$ in following simulations. The 3D model has total 6129120 nodes with the uniform discretization (about 20 million degrees of freedom). The total time steps are 2800 with time step size about 2.75 ns. We have used 100 processors on 2.2GHz/64 bit Opteron Linux cluster and 70G on memory. We perform the simulations under various the impact speeds at 61 m/s, 100 m/s, and 200 m/s, which is the same impact speed used in the experiments [84]. Note that the damage patterns under impact speeds at 200 m/s and 300 m/s have no significantly difference.

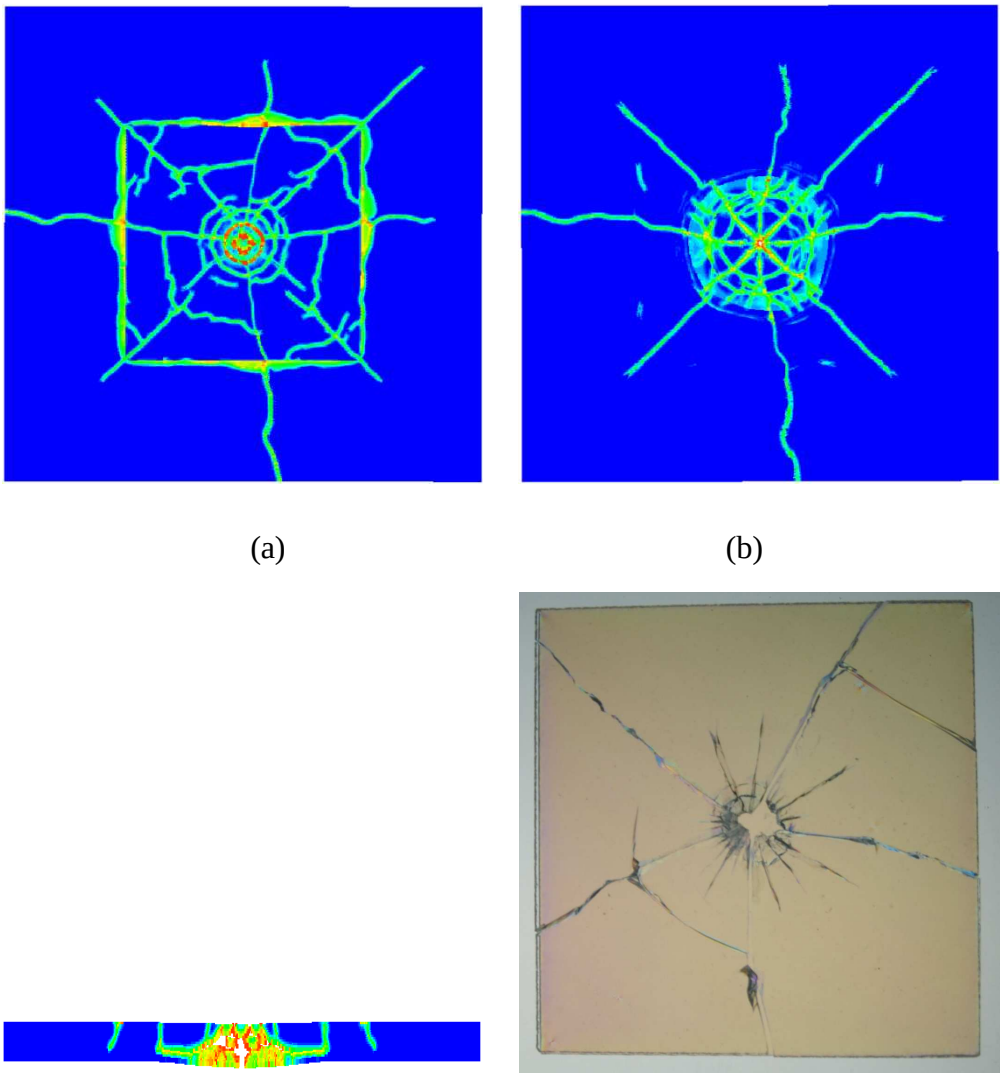

(a) (b)

(c) (d)

Figure 5.11. The damage maps at about 77 µs for glass layer under 61 m/s: a) top view (strike face); b) bottom view; c) cross section view; d) experimental result.

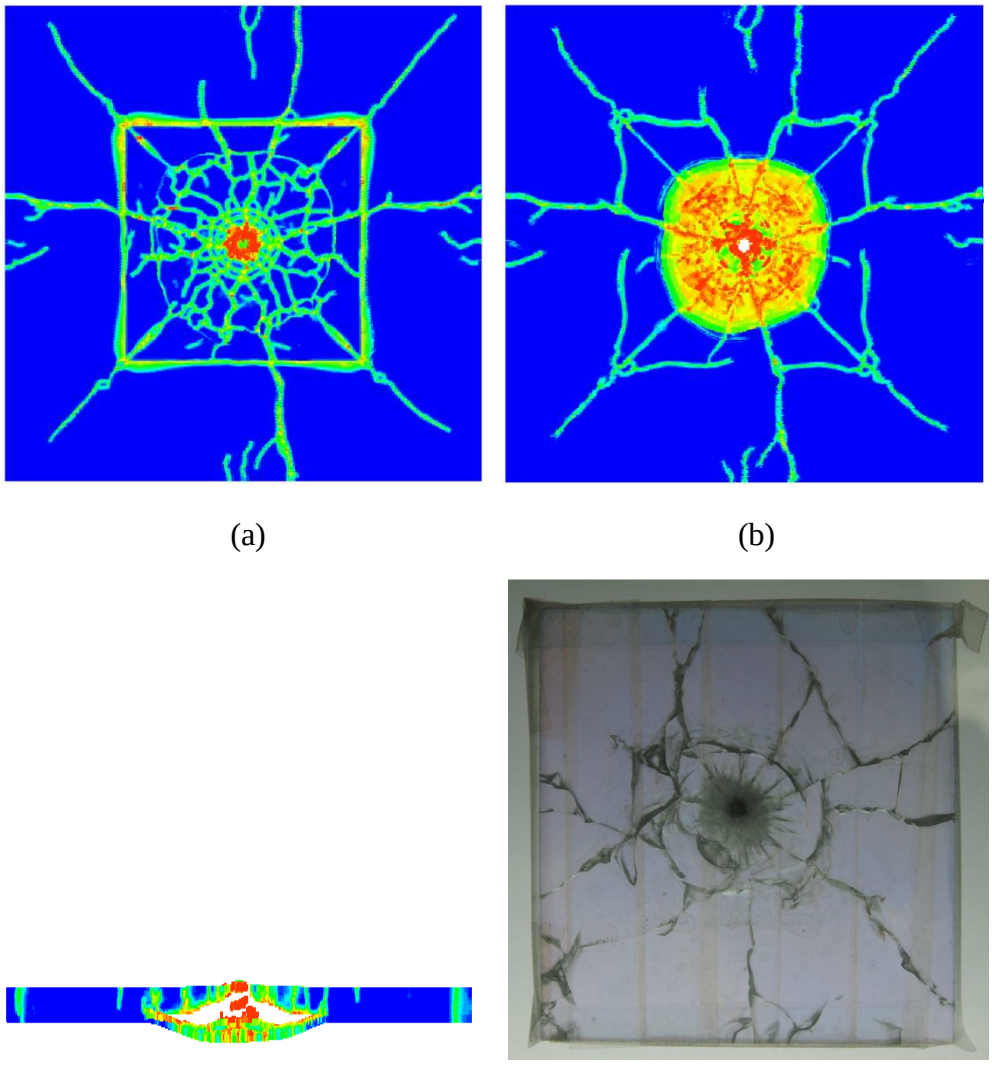

(a) (b)

(c) (d)

Figure 5.12. The damage maps at about 77 µs for glass layer under 100 m/s: a) top view (strike face); b) bottom view; c) cross section view; d) experimental result.

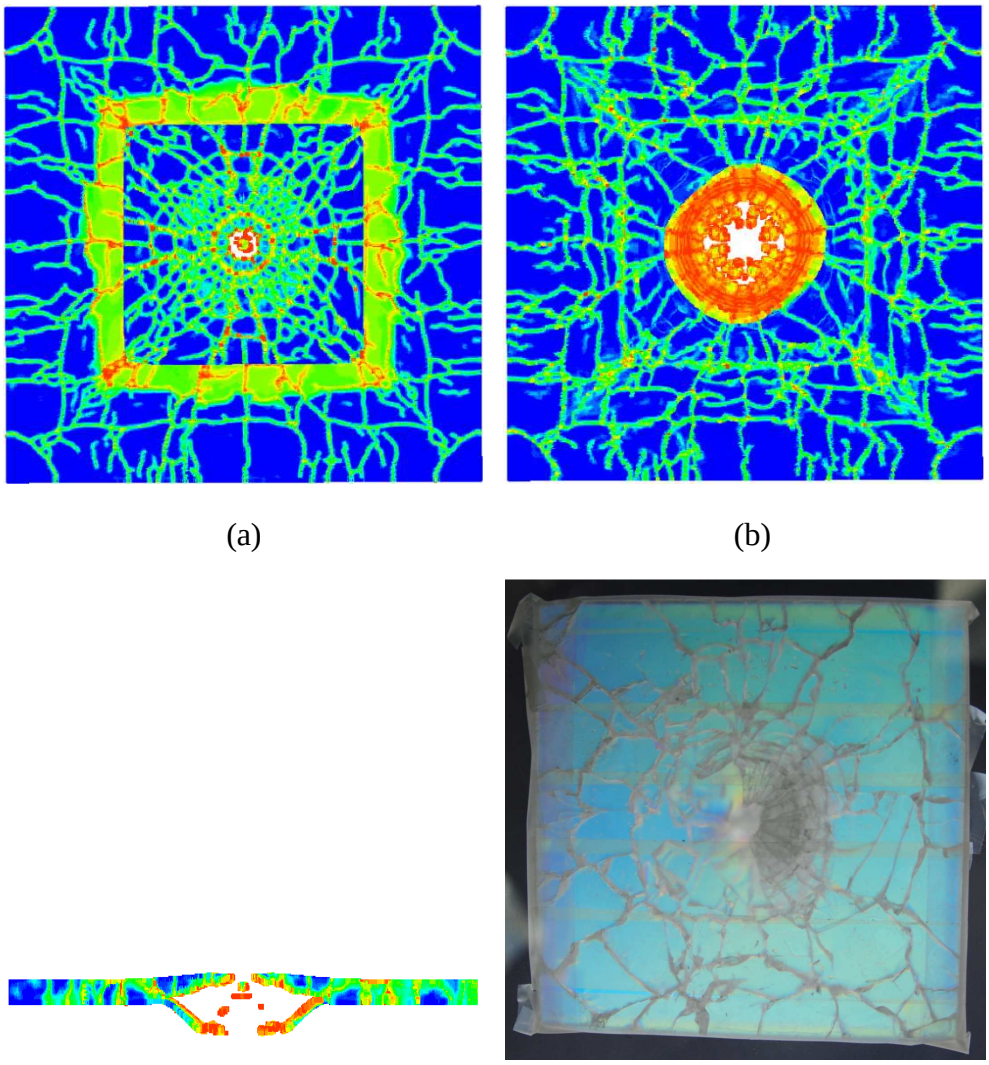

(a) (b)

(c) (d)

Figure 5.13. The damage maps at about 77 µs for glass layer under 200 m/s: a) top view (strike face); b) bottom view; c) cross section view; d) experimental result.

The damage maps for glass layer under various impact speeds at about 77 µs are shown in Figure 5.11, Figure 5.12, and Figure 5.13. Under impact speed at 61 m/s, the damage pattern is relatively simple and only radial cracks and circumferential cracks are observed. For impact speed at 100 m/s, the most damage can be seen around the impact region. When impact speed increase to 200 m/s, there is a complex “spider web” damage

pattern that comprises with multiple radial and circumferential cracks and small fragments are observed. The propagation of anti-plane kinked cracks is captured under those different impact speeds in our simulations, which are also observed in the experiment under same impact speeds [84]. Note that we only use the peridynamic elasticity model for polycarbonate without taking plasticity into account. Thus, in the simulations, the energy cannot dissipate through the polycarbonate layer (mainly due to the plastic deformation), which results in more damage on the glass layer, especially under impact speed at 200 m/s. Compare our simulation results with experimental results [84] (see Figure 5.2), we capture the main features of impact damage in the glass layer in terms of various impact speeds.

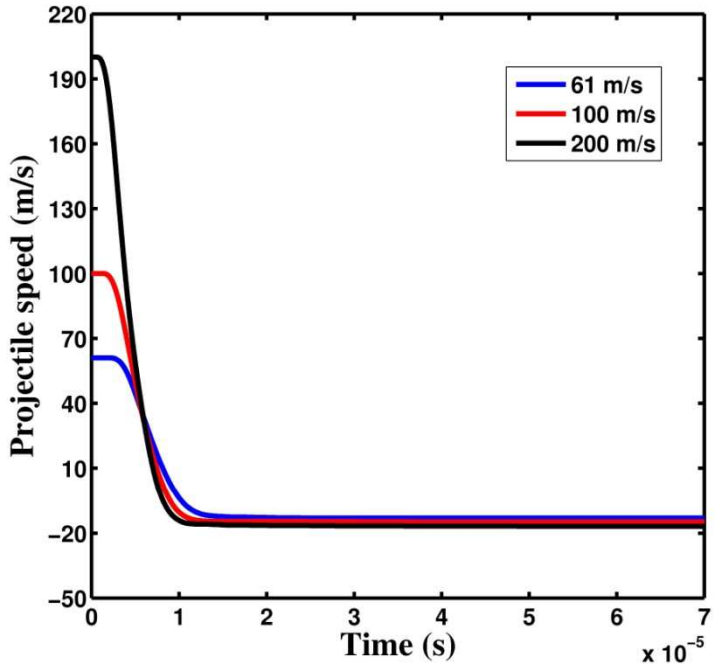

Figure 5.14. Projectile speed profiles for different impact speeds.

In the experiment [84], the projectile was ejected from the target for all the impact speeds. The reject speeds are 2.6 m/s for impact speed at 61 m/s, 7.8 m/s for impact speed at 100 m/s, and 33 m/s for impact speed at 200m/s. In our simulations, we also observed similar behavior that the projectile was ejected from the target. The projectile speed profile is shown in Figure 5.14. In our simulation, the reject speeds are 13m/s for impact speed at 61 m/s, 14.9 m/s for impact speed at 100 m/s, and 16.8 m/s for impact speed at 200m/s. The possible reason for the difference of the eject speed between experiments and simulations is that the fracture energy of soda-lime glass can be different under different impact speeds (or loading rates [94]). In our simulations, we use the same fracture energy for all the cases. Other factors may also influence the eject speed. For instance, the steel bullet can experience plastic deformation during the impact and may even lose some mass. Moreover, the location where measure the eject speed, are not very clear in the experiment.

5.4.3 Impact damage on glass backing by polycarbonate with thicker glass layer

We consider a thick glass layer as 5 mm with the same planar dimensions and polycarbonate is still 3 mm thick. The impact speed is about 61 m/s and the fracture energy is 8 J/m^2. The total simulation time is about 77 μs.

The damage maps for the glass layer are shown in Figure 5.17, Figure 5.16, and Figure 5.17. We can observe some similarities between different thicknesses. For example, radial cracks are observed on the top face (strike face) and spall fracture is also

observed. However, the quadrant crack initiation and propagation is different due to the thin plate tends to have more flexural motion. On the other hand, the quadrant cracks are not so significant in a thick glass plate since the thick glass plate has less bend motion. Furthermore, more circumferential cracks are observed near the impact cater for the thin glass plate. The Hertz cone cracks are observed through the thickness for the thick glass layer while spall fracture appears for the thin glass plate (see Figure 5.17).

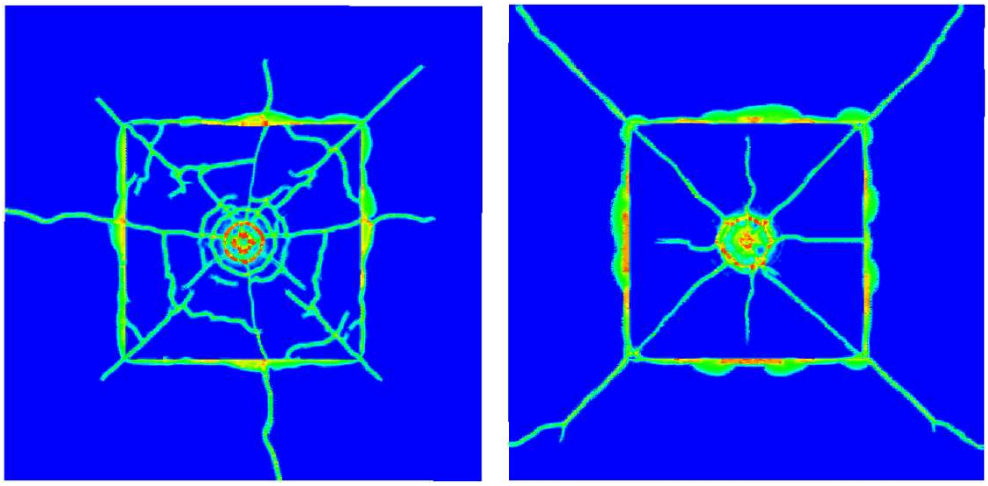

Figure 5.15. Damage maps of top face (strike face) for thin glass plate (left) and thick glass plate (right).

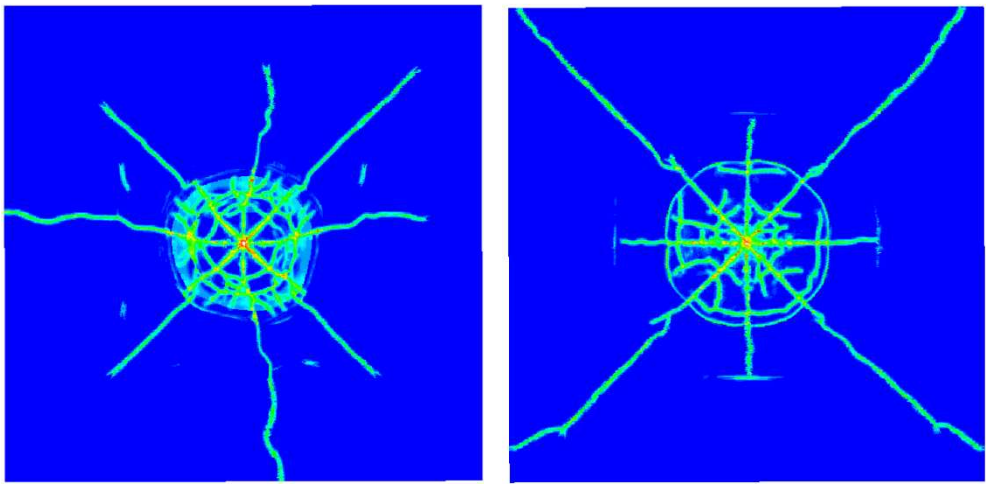

Figure 5.16. Damage maps of bottom face for thin glass plate (left) and thick glass plate (right).

Figure 5.17. Damage maps of cross section view for thin glass plate (left) and thick glass plate (right).

As expected, the thickness of the glass plate has significant influence on the ballistic performance (see Figure 5.18). For instance, the projectile reject speed for the thick glass is about 29.2 m/s and for the thin glass is about 13 m/s. This also indicates that increasing the thickness of the plate improves the ballistic performance.

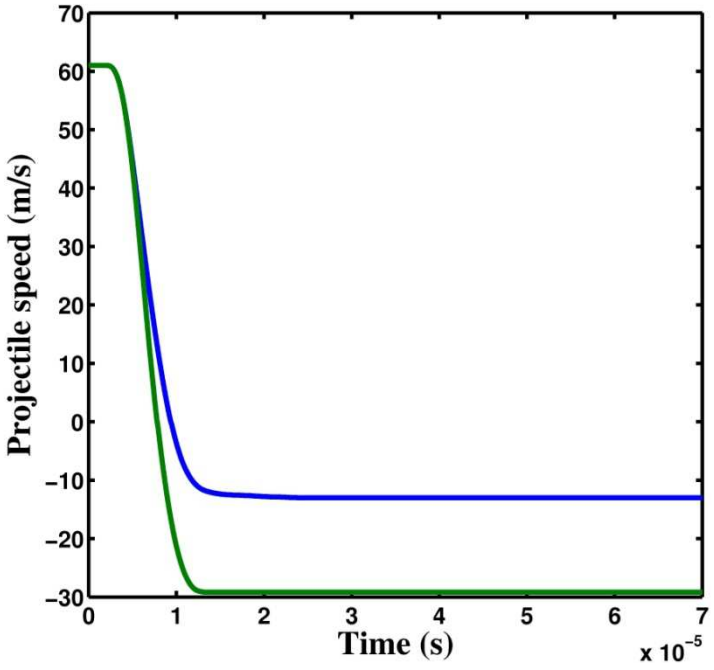

Figure 5.18. Projectile speed profiles for different glass plate thickness.

5.5 Summary

The damage and fracture patterns on glass laminates under high velocity impact are studied by using the peridynamic code EMU. Experimental results are reviewed from the literature in terms of various impact speeds. Some important mechanisms, which may influence the experimental results, are identified. Appropriate horizon size and *m* (grid density) are determined in order to find a balance between the computational efficiency and accuracy of the simulation results by performing convergence studies in terms of damage patterns and projectile impact speed profile. The damage patterns of glass laminates under various impacts are investigated. The main damage features are captured with respect to various impact speeds, such as radial cracks, circumferential cracks, kinked cracks, and fragmentation. The ejection of projectile from the target is also

captured in our simulations. Then, we perform simulation of two different thickness of glass plate under same impact speed. The thickness of the glass plate influences the initiation and development of quadrant cracks as well as the eject speeds. The simulation results show that peridynamic model is capable of capturing qualitatively damage pattern and fracture behavior of glass laminates and have a good agreement with the experimental results. As for the quantitatively comparison, further investigations are needed to develop a peridynamic plasticity model (see e.g. [29]) as well as a damage model for the polycarbonate layer.

Chapter 6
Conclusions and future work

6.1 Conclusions

The objective of this dissertation is to develop peridynamic models for modeling dynamic brittle fracture in anisotropic and multilayered materials. We studied, in particular, dynamic fracture in unidirectional fiber-reinforced composites and impact damage and fracture on glass layers. Most of the work presented here has appeared or will soon appear in journal publications (see [45], [46], [44]).

We derived the 2D peridynamic *J*-integral formulation based on the infinitesimal virtual extension of the mode-I crack. An algorithm to compute the peridynamic *J*-integral has been presented. The formulation of peridynamic *J*-integral coincides with the

classical *J*-integral formula when the horizon size goes to zero. We performed the convergence studies and compare our results with finite element solution using ABAQUS. The influence of skin effects and imposed boundary conditions on peridynamic *J*-integral calculations has been discussed in detail. Appropriate horizon size and integral contour locations choices in terms of sample geometry have been suggested in order to compute the peridynamic *J*-integral accurately.

Then, we developed a new homogenized peridynamic model for a unidirectional fiber-reinforced composite lamina. Analytical expressions for the micromodulus function and the critical relative elongation are obtained by calibrating them, for a given horizon size, to measurable material properties of the UD composite lamina, such as the elastic strain energy density in a homogeneous deformation and mode I fracture energies. We proposed a computational method for a homogenized peridynamics description of fiber-reinforced composites and we use it to simulate dynamic brittle fracture and damage in these materials, which had a good agreement with some experimental results.

The detailed investigations with respect to the location of the suddenly applied loadings (on the outer boundaries or on the center pre-crack faces) and with respect to the magnitude of the suddenly applied loads led to the following conclusions:

- The failure and damage patterns induced by dynamically loading a UD FRC composite are strain rate dependent and dramatically more complex than what is observed from quasi-static loadings. No explicit rate-dependence was used in the peridynamic model. The inertia and wave propagation led directly to the observed behavior.

- The stress waves control the dynamic crack propagation process, influencing curving of crack paths and crack arrest, as well as the crack propagation speed.
- The dynamic effects lead to coexistence of damage modes and to transitions between these modes. Depending on the type of loading (from the boundaries, or from the interior pre-crack faces) the peridynamic model captures splitting fracture, diffuse damage (shattering) in the matrix and separation between "fiber bonds", crack curving and crack migration in the matrix, and matrix crack branching.
- The dynamic fracture and damage profiles obtained from the peridynamic model are consistent with recent experimental observations on dynamic fracture in UD FRCs. For example, branching of a splitting crack into two matrix cracks is observed in UD composites dynamically loaded along the transverse direction. Branching does not happen unless the load level is sufficiently high. In both the experiments and the peridynamics computations, this type of loading does not cause breakage of the fibers (or fiber bonds).

We also showed the results of damage and fracture on glass layers under high impact speed. The convergence studies are performed in order to choose appropriate horizon size and *m* to perform the simulations. Then, two layers material system (one layer glass and one layer polycarbonate) was used to perform impact simulations under various impact speeds. We compared the damage patterns from peridynamic simulations with some recent experimental results from other groups. The main damage features and events were successfully captured by our simulations.

In conclusion, peridynamics, a nonlocal continuum model, can correctly reproduce important characteristic features of dynamic brittle fracture: crack branching, crack-path instability, symmetry-breaking of crack paths, successive branching, and fragmentation. Moreover, no special element and/or special grid are required in order to obtain certain types of crack path and damage pattern in peridynamics.

6.2 Future work

The future work includes a few aspects as following:

- Numerical dispersion has been observed in the dynamic simulations which may influence the crack propagation speed and/or crack propagation direction. Thus, the Multi-dimensional Flux-Corrected Transport scheme should be developed and implemented in order to eliminate the oscillations behind the shock wave.
- The bond-based peridynamic UD FRCs model cannot capture the all the material parameters, such as Poisson's ratio. In future, we could develop the state-based composite model in order to correctly obtain all the material parameters.
- In peridynamics, most simulations are performed based on the linear elastic material model. Peridynamic models that include the plasticity (polycarbonate) [29] or nonlinear elasticity (rubber) are important to be included in the simulations. Moreover, the damage model is reasonable for modeling the dynamic brittle fracture but may not suitable for other types of material response. In the future, those types of material models can be employed for better modeling high velocity impact problems.

- Residual stresses occur for a variety of reasons, including inelastic deformations and heat treatment. The material with high levels of residual stress will encourage crack initiation and growth, especially under dynamic loading condition. Thus, the damage and fracture of brittle material and ductile material with residual stress under dynamic loading is an important topic. One possible approach is to assign random critical relative elongation s_0 for each peridynamic bonds or use probability distribution, such as Weibull distribution. When the shock wave passes through the "weak" region, the cracks will initiate and propagate. In fact, we have observed similar phenomenon in homalite-100 with loaded on the pre-crack surface, the crack tends to initiate at the boundary due to the "skin effect" due to the stress wave (see[95]).

Bibliography

[1] BN Cox, H Gao, D Gross, and D Rittel, Review: mordern topics and challenges in dynamic fracture. *Journal of the Mechanics and Physics of Solids*, vol. 53, pp. 565-596, 2005.

[2] M Ramulu and AS Kobayashi, Mechanics of crack curving and branching-A dynamic fracture analysis *International Journal of Fracture*, vol. 27, pp. 187-201, 1985.

[3] S Bouzid, A Nyoungue, Z Azari, N Bouaouadja, and G Pluvinage, Fracture criterion for glass under impact loading. *International Journal of Impact Engineering*, vol. 25, pp. 831-845, 2001.

[4] B Hopkinson, A method of measuring the pressure produced in detonation of high explosives or by the impact of bullets. *Proceedings of the Royal Society A.*, vol. 89, pp. 411-413, 1914.

[5] WJ Murri, DR Curran, and L Seaman, Fracture model for high energy propellant. in *In Proceeding of the American Physical Society Conference on Shock Waves in Condensed Matter*, NY, 1982, pp. 460-464.

[6] S Kazemahvazi, D Zenkert, and M Burman, Notch and strain rate sensitivity of non-crimp fabric composites. *Composites Science and Technology*, vol. 69, pp. 793-800, 2009.

[7] A Haque and M Ali, High strain rate responses and failure analysis in polymer matrix composites-an experimental and finite element study. *Journal of Composite*

Materials, vol. 39, pp. 423-450, 2005.

[8] TL Anderson, *Fracture Mechanics: Fundamentals and Applications.*, 3rd ed.: CRC Press, 2005.

[9] K Ravi-Chandar and WG Knauss, An experimental investigation into dynamic fracture: I. Crack initiation and arrest. *International Journal of Fracture*, vol. 25, pp. 247-262, 1984.

[10] RL Woodward, BJ Baxter, SD Pattie, and P McCarthy, Impact fragmentation of brittle materials. *Journal of Physics C*, vol. 3, pp. 259-264, 1991.

[11] DS Dugdale, Yielding of steel sheets containing slits. *Journal of the Mechanics and Physics of Solids*, vol. 8, pp. 100-108, 1960.

[12] GL Barenblatt, The mathematical theory of equilibrium cracks in brittle fracture. *Advances in Applied Mechanics*, vol. 7, pp. 55-129, 1962.

[13] GT Camacho and M Ortiz, Adaptive lagrangian modeling of ballistic penetration of metallic targets. *Computational Methods in Applied Mathematics*, vol. 142, pp. 269-301, 1997.

[14] XP Xu and A Needleman, Numerical simulations of dynamic crack growth along an interface *International Journal of Fracture*, vol. 74, pp. 289-324, 1996.

[15] YD Ha and F Bobaru, Studies of dynamic crack propagation and crack branching with peridynamics. *International Journal of Fracture*, vol. 162, pp. 229-244, 2010.

[16] PA Klein, JW Foulk, EP Chen, SA Wimmer, and H Gao, Physics-based modeling of brittle fracture: cohesive formulations and the application of meshfree methods. *Theoretical and Applied Fracture Mechanics*, vol. 37, pp. 99-166, 2001.

[17] T Belytschko and T Black, Elastic crack growth in finite elements with minimal remeshing. *International Journal for Numerical Methods in Engineering*, vol. 45, pp. 601-620, 1999.

[18] T Belytschko, H Chen, J Xu, and G Zi, Dynamic crack propagation based on loss of hyperbolicity and a new discontinuous enrichment. *International Journal for Numerical Methods in Engineering*, vol. 58, pp. 1873–1905, 2003.

[19] Song, Areias, PMA , and T Belytschko, A method for dynamic crack and shear band

propagation with phantom nodes. *International Journal for Numerical Methods in Engineering*, vol. 67, pp. 868–893, 2006.

[20] CL Richardson, J Hegemann, E Sifakis, and J Hellrung, An XFEM method for modelling geometrically elaborate crack propagation in brittle materials. *International Journal for Numerical Methods in Engineering*, vol. 88, pp. 1042-1065, 2009.

[21] DBP Huynh and T Belytschko, The extended finite element method for fracture in composite materials. *International Journal for Numerical Methods in Engineering*, vol. 77, pp. 214-239, 2009.

[22] WT Ashurst and WG Hoover, Microscopic fracture studies in 2-dimensional triangular lattice. *Physical Review B*, vol. 14, pp. 1465-1473, 1976.

[23] FF Abraham, Instability dynamics of fracture: A computer simulation investigation. *Physical Review Letters*, vol. 73, pp. 272-275, 1994.

[24] FF Abraham, D Brodbeck, WE Rudge, and XP Xu, A molecular dynamics investigation of rapid fracture mechanics. *Journal of the Mechanics and Physics in Solids*, vol. 45, pp. 1595-1619, 1997.

[25] P Vashishta, PK Kalia, and A Nakano, Multimillion atom molecular dynamics simulations of nanostructures on parallel computers. *Journal of Nanopaticle Research*, vol. 5, pp. 119-135, 2003.

[26] A Sharma, RK Kalia, and P Vashishta, Large multidimensional data vizualization for material science. *Computing in Science and Engineering*, vol. 5, pp. 26-33, 2003.

[27] K Kadau, TC Germann, and PS Lomdahl, Larger-scale molecular dynamics simulation of 19 billion particles *International Journal of Modern Physics C*, vol. 15, pp. 193-201, 2004.

[28] SA Silling, Reformulation of elasticity theory for discontinuities and long-range forces. *Journal of the Mechanics and Physics of Solids*, vol. 48, pp. 175-209, 2000.

[29] JT Foster, SA Silling, and WW Chen, Viscoplasticity using peridynamics *International Journal for Numerical Methods in Engineering*, vol. 81, pp. 1242-1258, 2010.

[30] J Foster, SA Silling, and WW Chen, An energy based failure criterion for use with

peridynamic states *International Journal for Multiscale Computational Engineering*, vol. 9, pp. 675-688, 2011.

[31] YD Ha and F Bobaru, Characteristics of dynamic brittle fracture captured with peridynamics. *Engineering Fracture Mechanics*, vol. 78, pp. 1156-1168, 2011.

[32] J Xu, E Askari, O Weckner, and SA Silling, Peridynamic analysis of impact damage in composite laminates. *Journal of Aerospace Engineering*, vol. 21, pp. 187-194, 2008.

[33] B Kilic, A Agwai, and E Madenci, Peridynamics theory for progressive damage prediction in center-cracked composite laminates. *Composite Structures*, vol. 90, pp. 141-151, 2009.

[34] SA Silling and F Bobaru, Peridynamic modeling of membranes and fibers. *International Journal of Non-Linear Mechanics*, vol. 40, pp. 395-409, 2005.

[35] F Bobaru, Influence of van der waals forces on increasing the strength and toughness in dynamic fracture of nanofiber networks: a peridynamic approach. *Modelling and Simulation in Materials Science and Engineering*, vol. 15, pp. 397-417, 2007.

[36] JR Rice, A path independent integral and the approximate analysis of strain concentration by notches and cracks. *Journal of Applied Mechanics*, vol. 9, pp. 379-386, 1968.

[37] SA Silling and RB Lehoucq, Peridynamic theory of solid mechanics. *Advances in Applied Mechanics*, vol. 44, pp. 73-168, 2010.

[38] SR Hallett, BG Green, WG Jiang, and MR Wisnom, An experimental and numerical investigation into the damage mechanisms in notched composites. *Composites Part A: Applied Science and Manufacturing*, vol. 40, pp. 613-624, 2009.

[39] IM Daniel, JJ Luo, PM Schubel, and BT Werner, Interfiber/interlaminar failure of composites under multi-axial states of stress. *Composites Science and Technology*, vol. 69, pp. 764-771, 2009.

[40] EJ Pineda, AM Wass, BA Bednarcyk, CS Collier, and PW Yarrington, Progressive damage and failure modeling in notched laminated fiber reinforced composites. *International Journal of Fracture*, vol. 158, pp. 125-143, 2009.

[41] A Gilat, RK Goldberg, and GD Roberts, Experimental study of strain-rate-dependent

behavior of carbon/epoxy composite. *Composites Science and Technology*, vol. 62, pp. 1469-1476, 2002.

[42] T Gomez-del Rio, E Barbero, R Zaera, and C Navarro, Dynamic tensile behaviour at low temperature of CFRP using a split hopkinson pressure bar. *Composites Science and Technology*, vol. 65, pp. 61-71, 2005.

[43] J Xu, E Askari, O Weckner, H Razi, and SA Silling, Damage and failure analysis of composite laminates under biaxial loads. in *In: 47th AIAA Structures, Structural Dynamics, and Materials Conference*, Honolulu, HI, 2007.

[44] W Hu, YD Ha, SA Silling, and F Bobaru, The formulation and computation of the nonlocal J-integral in bond-based Peridynamics. [submitted] *International Journal of Fracture*.

[45] W Hu, YD Ha, and F Bobaru, Modeling dynamic fracture and damage in fiber-reinforced composites with peridynamics. *International Journal for Multiscale Computational Engineering*, vol. 9, pp. 707-726, 2011.

[46] W Hu, YD Ha, and F Bobaru, Peridynamic simulations of dynamic fracture in unidirectional fiber-reinforced composites. *Computer Methods in Applied Mechanics and Engineering*, vol. 217-220, pp. 247-261, 2012.

[47] F Bobaru and W Hu, The meaning, selection, and use of the peridynamic horizon. (under review) *International Journal of Fracture*, 2012.

[48] F Bobaru, M Yang, LF, Silling, SA Alves, E Askari, and J Xu, Convergence, adaptive refinement, and scaling in 1D peridynamics. *International Journal for Numerical Methods in Engineering*, vol. 77, pp. 852-877, 2009.

[49] SA Silling and E Askari, A meshfree method based on peridynamic model of solid mechanics. *Computers and Structures*, vol. 83, pp. 1526-1535, 2005.

[50] F Bobaru and YD Ha, Adaptive refinement and multiscale modeling in 2D peridynamics. *International Journal for Multiscale Computational Engineering*, vol. 9, pp. 635-660, 2011.

[51] E Hairer, C Lubich, and G Wanner, Geometric numerical integration illustrated by the stromer/verlet method. *Acta Numerica*, vol. 12, pp. 399-450, 2003.

[52] JW Hutchinson, Singular behavior at the end of a tensile crack tip in a hardening

material. *Journal of the Mechanics and Physics of Solids*, vol. 16, pp. 13-31, 1968.

[53] JR Rice and GF Rosengren, Plane strain deformation near a crack tip in a power-law hardening Material. *Journal of the Mechanics and Physics of Solids*, vol. 16, pp. 1-12, 1968.

[54] RB Lehoucq and SA Silling, Force flux and the peridynamic stress tensor. *Journal of the Mechanics and Physics of Solids*, vol. 56, pp. 1566-1577, 2008.

[55] F Bobaru and M Duangpanya, The peridynamic formulation for transient heat conduction *International Journal of Heat and Mass Transfer*, vol. 53, pp. 4047-4059, 2010.

[56] F Bobaru and M Duangpanya, A peridynamic formulation for transient heat conduction in bodies with evolving discontinuities [in press] *Journal of Computational Physics*, vol. http://dx.doi.org/10.1016/j.jcp.2011.12.017, 2012.

[57] H Jeff, The Boeing 787 Dreamliner: More Than an Airplane. in *Presentation to AIAA/AAAF Aircraft Noise and Emissions Reduction Symposium*, Monterey, California, 2007.

[58] EM Wu, "Fracture mechanics of anisotropic plates.," in *Composite material workshop*. Lancaster, PA: Technomic publishing, 1968, pp. 20-43.

[59] SC Tan, Mixed-mode fracture of notched unidirectional and off-axis laminates under tensile loading. *Journal of Composite Materials*, vol. 23, pp. 1082-1105, 1989.

[60] GF Sun, Fracture of fiberglass reinforced composites. *Journal of Composite Materials*, vol. 15, pp. 521-530, 1981.

[61] K Tohgo, SD Wang, and TW Chou, A criterion for splitting crack initiation in unidirectional fiber-reinforced composites. *Journal of Composite Materials*, vol. 27, pp. 1054-1076, 1993.

[62] E Eskandari and JA Nemes, Dynamic testing of composite laminates with a tensile split hopkinson bar. *Journal of Composite Materials*, vol. 34, pp. 260-273, 2000.

[63] FP Bowden, JH Brunton, JE Field, and AD Heyes, Controlled fracture of brittle solids and interruption of electrical current. *Nature*, vol. 216, pp. 38-42, 1967.

[64] TE Tay, G Liu, VBC Tan, XC Sun, and DC Pham, Progressive failure analysis of

composite. *Journal of Composite Materials*, vol. 42, pp. 1921-1966, 2008.

[65] JM Guimard, O Allix, N Pechnik, and T Pascal, Characterization and modeling of rate effects in the dynamic propagation of mode-II delamination in composite laminates. *International Journal of Fracture*, vol. 160, pp. 55-77, 2009.

[66] ND Cristescu, EM Craciun, and E Soos, *Mechanics of Elastic Composite.* New York: Chapman & Hall/CRC, 2004.

[67] JC Halpin and JL Kardos, The Halpin-Tsai equations: A review. *Polymer Engineering and Science*, vol. 16, pp. 344-352, 1976.

[68] SA Silling, M Epton, O Weckner, J Xu, and E Askari, Peridynamic states and constitutive modeling. *Journal of Elasticity*, vol. 88, pp. 151-184, 2007.

[69] S Jose, RR Kumar, MK Jana, and GV Rao, Intralaminar fracture toughness of a cross-ply laminate and its constituent sub-laminates. *Composites Science and Technology*, vol. 61, pp. 1115-1122, 2001.

[70] SW Yurgartis, Measurement of small angle fiber misalignments in continuous fiber composites *Composites Science and Technology*, vol. 30, pp. 279-293, 1987.

[71] PB Bogert, A Satyanarayana, and PB Chunchu, Comparison of damage path predictions for composite laminates by explicit and standard finite element analysis tool. in *In: 47th AIAA Structures, Structural Dynamics, and Materials Conference*, Newport, Rhode Island., 2006.

[72] W Yang, Z Suo, and CF Shih, Mechanics of dynamic debonding. *Proceedings of the Royal Society A*, vol. 433, pp. 679-697, 1991.

[73] JL Tsai, C Guo, and CT Sun, Dynamic delamination fracture toughness in unidirectional polymetric composites. *Composites Science and Technology*, vol. 61, pp. 87-94, 2001.

[74] W Xie, "Peridynamic flux-corrected transport algorithm for shock wave studies.," Enginering Mechanics, University of Nebraska-Lincoln, Lincoln, NE, Master thesis 2005.

[75] K Ravi-Chandar and WG Knauss, An experimental investigation into dynamic fracture: IV. On the interaction of stress waves with propagating cracks. *International Journal of Fracture*, vol. 26, pp. 189-200, 1984.

[76] PJ Patel, GA Gilde, PG Dehmer, and JW McCauley, Transparent ceramics for armor and EM window applications. *Proceedings of SPIE-The international Socity for Optical Engineering*, vol. 4102, pp. 1-14, 2000.

[77] CG Knight, MV Swain, and MM Chaudhri, Impacts of small steel spheres on glass surfaces *Journal of Materials Science*, vol. 12, pp. 1573-1586, 1977.

[78] MM Chaudhri and CR Kurkjian, Impact of small steel spheres on the surfaces of 'Normal' and 'Anomalous' glasses. *Journal of the American Ceramic Society*, vol. 69, pp. 404-410, 1986.

[79] A Ball and HW Mckenzie, On the low velocity impact behaviour of glass plates. *Journal De Physique IV*, vol. 4, pp. 783-788, 1994.

[80] RA Behr, JE Minor, and HS Norville, Structural behavior of architectural laminated glass *Journal of Structural Engineering*, vol. 119, pp. 202-222, 1993.

[81] MS Kim, HS Shin, and HC Lee, The effects of back plate materials on perfect cone formation in impact-loaded soda-lime glass. *International Journal of Impact Engineering*, vol. 28, pp. 281-290, 2003.

[82] SJ Bless, T Chen, and R Russell, Impact on glass laminates. in *In: 23rd International Symposium on Ballistics*, Tarragona, Spain, 2007, pp. 1503-1510.

[83] SJ Bless and T Chen, Impact damage in layered glass. *International Journal of Fracture*, vol. 162, pp. 151-158, 2010.

[84] Yu J, "Damage and Fracture of glass laminate under impact.," Army research laboratory, Aberdeen, Md, 2012.

[85] M Timmel, S Kolling, P Osterrieder, and PA DuBois, A finite element model for impact simulation with laminated glass. *International Journal of Impact Engineering*, vol. 34, pp. 1465-1478, 2007.

[86] J Ismail, F Zairi, M Nait-Abdelaziz, and Z Azari, How cracks affect the contact characteristics during impact of solid particles on glass surface: A computational study using anisotropic continuum damage mechanics. *International Journal of Impact Engineering*, vol. 40-41, pp. 10-15, 2012.

[87] T Pyttel, H Liebertz, and J Cai, Failure criterion for laminated glass under impact loading and its application in finite element simulation. *International Journal of*

Impact Engineering, vol. 38, pp. 252-263, 2011.

[88] E Holmstrom, J Samela, and K Nordlund, Atomistic simulations of fracture in sillica glass through hypervelocity impact. *A Letters Journal Exploring the Frontiers of Physics*, vol. 96, pp. 16005-p1-16005-p5, 2011.

[89] P Seleson and M Parks, On the role of the influence function in the peridynamic theory *International Journal for Multiscale Computational Engineering* , vol. 9, pp. 689-706, 2011.

[90] SC Wright, NA Fleck, and WJ Stronge, Ballistic impact of polycarbonate-An experimental inverstigation. *International Journal of Impact Engineering*, vol. 13, pp. 1-20, 1993.

[91] Silling SA. EMU. [Online]. http://www.sandia.gov/emu/emu.htm

[92] SA Silling, "Fragmentation modeling with EMU.," Sandia National Laboratories, Albuquerque, NM, Technical report 2005.

[93] C Hoeschl, M Okrouhlik, J Cerv, and J Benes, Analytical, computational and experimental investigations on stress wave propagation. *Applied Mechanics Reviews*, vol. 47, pp. 77-99, 1994.

[94] JC Wright, "Dyanmic fracture toughness of soda-lime glass.," Purdue University, Thesis 2010.

[95] W Hu and F Bobaru, "Crack branching on homalite-100.," University of Nebraska-Lincoln, Lincoln, NE, Technique report 2011.